ROTORDYNAMIC ANALYSIS OF CIRCUMFERENTIALLY GROOVED ANNULAR PUMP SEALS WITH TURBULENT FLOW AND INLET SWIRL

by

Kevin Wood Wilkes

Thesis submitted to the Faculty of the

Virginia Polytechnic Institute and State University

in partial fulfillment of the requirements for the degree of

Master of Science

in

Mechanical Engineering

APPROVED:

Dr. R. Gordon Kirk, Chairman

Dr. Hal L. Moses

Dr. Walter F. O'Brien

August, 1991

Blacksburg, Virginia

c.2

ROTORDYNAMIC ANALYSIS OF CIRCUMFERENTIALLY GROOVED ANNULAR PUMP SEALS WITH TURBULENT FLOW AND INLET SWIRL

by

Kevin Wood Wilkes

Dr. R. Gordon Kirk, Chairman

Mechanical Engineering

(ABSTRACT)

In this thesis an analysis is developed to predict the leakage and dynamic characteristics for circumferentially grooved turbulent annular seals used in turbopumps. The flow in the groove is modelled using turbulent shear layer theory and an entrance loss model is applied at the inlet and land regions of the seal. The governing equations are derived using Hirs' turbulent lubrication theory. The equations are expanded to yield zeroth and first order perturbation equations for small rotor displacements about a centered position. The leakage and velocity distribution is obtained from a numerical solution of the zeroth order equations. The first order equations define the dynamic pressure distribution which is integrated to yield the fluid force reactions. The model predictions are compared to test results for smooth walled and grooved seals. The model shows good qualitative agreement with experimental test results for seal leakage and rotordynamic coefficients. Actual quantitative agreement is unresolved given the high level of experimental uncertainty in the test results.

Acknowledgements

This project was initiated by Dr. David A. Elrod who provided a preliminary computer program to analyze smooth tapered annular seals with a constant entrance loss coefficient. The idea to model the entrance loss as a function of flow distance stems from his Ph.D. dissertation at Texas A & M University. Although most of the original code has been rewritten, the first order solution technique including the numerical integration subroutines were taken directly from Dr. Elrod's original program. Dr. Clayton Nelson of Texas A & M University is also credited with developing these subroutines.

The author wishes to thank Dr. R. Gordon Kirk for his encouragement and support throughout this project. His experience and suggestions relating to the grooved seal program have been indispensable. Dr. Hal L. Moses and Dr. Walter F. O'Brien have also provided insight and inspiration in turbomachinery fluid dynamics. Funding for this project was provided by the Mechanical Engineering Department at Virginia Polytechnic Institute and State University, the Virginia Tech Rotordynamics Laboratory, and its corporate sponsors.

Table of Contents

List of Illustrations

List of Tables

Nomenclature

Variable Name	Description
C	direct damping for isotropic model
c	cross-coupled damping for isotropic model
C_{xx}	direct damping in x direction
C_{yy}	direct damping in y direction
C_{xy}	cross-coupled damping
C_{yx}	cross-coupled damping
D	shaft diameter
D_g	groove depth
e	radius of orbit for circular rotor whirl
f_w	wall friction factor defined by Hirs equation
f_d	developing flow friction factor
f_g	groove friction factor for turbulent shear layer
F_x	force on rotor in $+x$ direction
F_y	force on rotor in $+y$ direction
F_r	force on rotor in $+r$ direction
F_θ	force on rotor in $+\theta$ direction

H	seal radial clearance
K	direct stiffness for isotropic model
k	cross-coupled stiffness for isotropic model
K_{xx}	direct stiffness in x direction
K_{yy}	direct stiffness in y direction
K_{xy}	cross-coupled stiffness
K_{yx}	cross-coupled stiffness
L	seal length
L_g	groove length
M	direct inertia for isotropic model
m	cross-coupled inertia for isotropic model
M_{xx}	direct inertia in x direction
M_{yy}	direct inertia in y direction
M_{xy}	cross-coupled inertia
M_{yx}	cross-coupled inertia
mr	Hirs exponent for rotor friction factor
ms	Hirs exponent for stator friction factor
nr	Hirs coefficient for rotor friction factor
ns	Hirs coefficient for stator friction factor
P	static pressure
P_a	upstream static pressure
P_b	downstream static pressure
$\dot{Q}$	seal leakage
R	shaft radius
r	$+r$ cylindrical coordinate
R_s	stator radius
R_r	rotor radius

Re	Reynolds number: $\frac{HV}{\nu}$
t	time
V	fluid velocity: $\sqrt{V_z^2 + V_\theta^2}$
V_z	axial fluid velocity
V_θ	circumferential fluid velocity
x	$+x$ cartesian coordinate
$\dot{x}$	velocity in $+x$ direction
$\ddot{x}$	acceleration in $+x$ direction
y	$+y$ cartesian coordinate
$\dot{y}$	velocity in $+y$ direction
$\ddot{y}$	acceleration in $+y$ direction
z	$+z$ cylindrical coordinate
α	flow divergence angle for turbulent shear layer
ζ	entrance loss coefficient
θ	$+\theta$ cylindrical coordinate
λ	pressure loss due to inlet sudden contraction
μ	fluid dynamic viscosity
ν	fluid kinematic viscosity: $\frac{\mu}{\rho}$
ρ	fluid density
τ_s	shear stress at stator surface
τ_r	shear stress at rotor surface
τ_w	wall shear stress defined by Hirs equation
ϕ	seal coordinate measured from the line of centers: $\theta - \Omega t$
Ω	rotor whirl angular velocity
ω	shaft angular velocity
0	subscript denoting zeroth order variables
1	subscript denoting first order variables

1. Introduction

The goal of this research was to predict the rotordynamic coefficients of annular pressure seals with circumferential grooves. Annular seals are widely used in pumps, compressors, and other turbomachines primarily to reduce leakage between regions of different pressure. The addition of circumferential grooves is a common means of enhancing leakage reduction. Two typical seal configurations are shown in Figure 1 on page 4. In each case the seal is composed of a rotating part (rotor) in close proximity with a stationary part (stator). The neck-ring seal is located at the suction region of a shrouded centrifugal impeller and is used to reduce leakage between impeller shroud and case into the impeller inlet. The interstage seal is located between the shaft and the stationary vanes to restrict leakage between stages where high pressure differences may exist. In addition to controlling leakage, the fluid forces developed inside an annular seal will affect the dynamic response of the system. The ability to predict these forces and understand the physics behind them is crucial to the design or analysis engineer in minimizing rotor vibration. The linearized equation of motion (1.1) used to model the fluid forces acting on the rotor is well documented by Vance (1) and Adams (2,3) among others. This model is universally accepted in the literature and treats the presence of a seal as a system of springs, dampers, and added mass which influence the lateral motion of the rotor. The stiffness, damping, and added mass coefficients are defined by the

matrices K_{ij}, C_{ij}, and M_{ij} respectively. These terms are collectively referred to as the rotordynamic coefficients of the seal.

$$-\begin{Bmatrix} F_x \\ F_y \end{Bmatrix} = \begin{bmatrix} K_{xx} & K_{xy} \\ K_{yx} & K_{yy} \end{bmatrix} \begin{Bmatrix} x \\ y \end{Bmatrix} + \begin{bmatrix} C_{xx} & C_{xy} \\ C_{yx} & C_{yy} \end{bmatrix} \begin{Bmatrix} \dot{x} \\ \dot{y} \end{Bmatrix} + \begin{bmatrix} M_{xx} & M_{xy} \\ M_{yx} & M_{yy} \end{bmatrix} \begin{Bmatrix} \ddot{x} \\ \ddot{y} \end{Bmatrix} \tag{1.1}$$

It is often assumed, as in the present analysis, that the whirling motion of the rotor due to a rotating unbalance follows a circular path which is concentric with the geometric center of the seal. The force equations then become isotropic and may be written as follows.

$$-\begin{Bmatrix} F_x \\ F_y \end{Bmatrix} = \begin{bmatrix} K & k \\ -k & K \end{bmatrix} \begin{Bmatrix} x \\ y \end{Bmatrix} + \begin{bmatrix} C & c \\ -c & C \end{bmatrix} \begin{Bmatrix} \dot{x} \\ \dot{y} \end{Bmatrix} + \begin{bmatrix} M & m \\ -m & M \end{bmatrix} \begin{Bmatrix} \ddot{x} \\ \ddot{y} \end{Bmatrix} \tag{1.2}$$

The rotordynamic coefficients are referred to as direct stiffness (K), cross-coupled stiffness (k), direct damping (C), cross-coupled damping (c), direct inertia (M), and cross-coupled inertia (m). The cross-coupled terms arise due to the swirling motion (circumferential velocity) of the fluid inside the seal. These terms account for the fact that motion in one direction causes a force in an orthogonal direction. The opposite signs on the cross-coupled terms are a consequence of using a cartesian coordinate system to describe a polar phenomenon. That is, for a positive cross-coupled coefficient, a displacement in the $+r$ direction produces a force in the $+\theta$ direction. Hence, a $+x$ displacement produces a force in the $+y$ direction, but a $+y$ displacement produces a force in the $-x$ direction.

This effect can be visualized by a coordinate transformation where the forces are composed of radial and tangential components as shown in Figure 2 on page 5. This figure shows the forces on a rotor in a circular whirl orbit of amplitude e and whirl angular velocity Ω. The radial force acts along the line of centers and the tangential force acts in the direction of positive rotor whirl. It is shown in Appendix A that these forces may be expressed in terms of the whirl velocity and the rotordynamic coefficients as follows.

$$\frac{F_r}{e} = -K - c\Omega + M\Omega^2 \tag{1.3}$$

$$\frac{F_\theta}{e} = k - C\Omega - m\Omega^2 \tag{1.4}$$

Equation (1.3) shows that positive direct stiffness and positive cross-coupled damping act as a restoring force which tends to stabilize the rotor system. Positive added mass, however, tends to destabilize the system by producing a force in the same direction as the displacement, e. Equation (1.4) shows that positive cross-coupled stiffness also has a destabilizing effect producing a force in the direction of positive rotor whirl. Positive direct damping acts to balance this effect. For synchronous rotor whirl ($\Omega =$ shaft speed) the stiffness to damping ratio ($k/\Omega C$) is often quoted as a measure of shaft stability. It is argued by Adams (4) that the cross-coupled inertia, m, produces a force proportional to Ω^2 which would overwhelm the stiffness and damping terms and always result in unstable negative rotor whirl. The absence of this behavior in experimental results suggests that $m \equiv 0$, as Adams indicates. Many authors still include the cross-coupled inertia terms in their analysis, but find that the calculated values are negligible in the final results.

These equations also show that the forces developed in a seal are quadratic functions of the whirl velocity. This observation is used both analytically and experimentally to determine the rotordynamic coefficients of a seal. By analyzing the forces developed at different whirl velocities, the rotordynamic coefficients may be determined by fitting a parabola through a plot of force versus whirl velocity. This is the procedure used in the present analysis. The rotordynamic coefficients will in general vary with shaft rotational speed, since this will strongly influence the circumferential velocity in the seal. The goal of this work is to predict the rotordynamic coefficients for a given seal geometry, fluid conditions, and shaft speed.

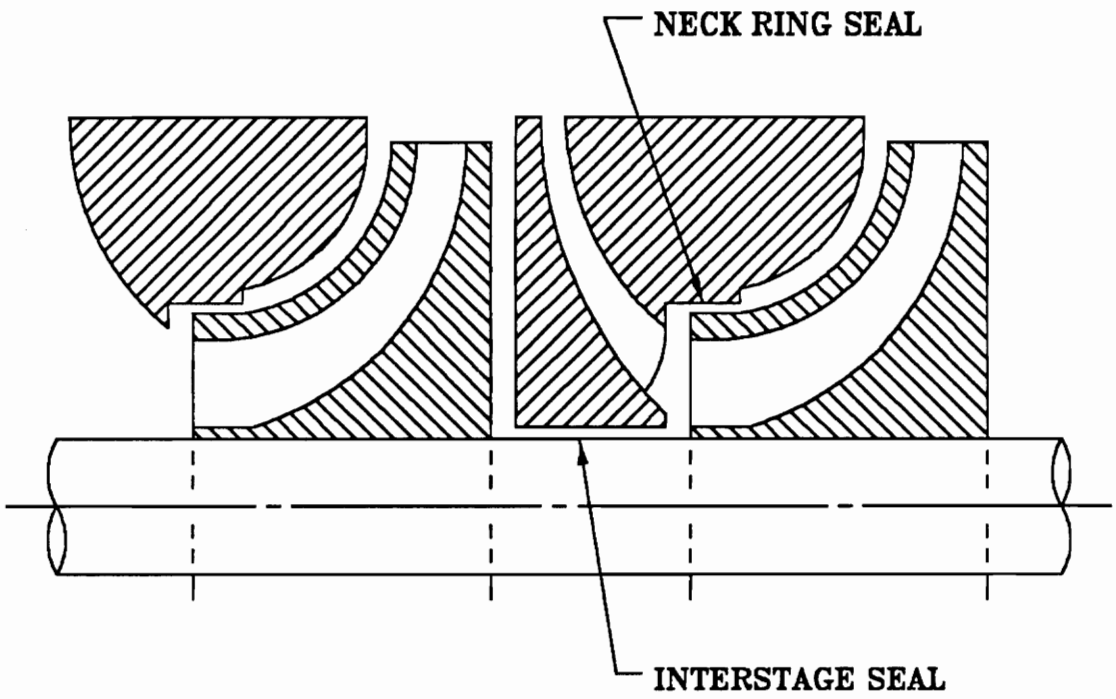

Figure 1. Neck-Ring and Interstage Seals: Cross-section of a centrifugal pump showing typical locations of annular seals.

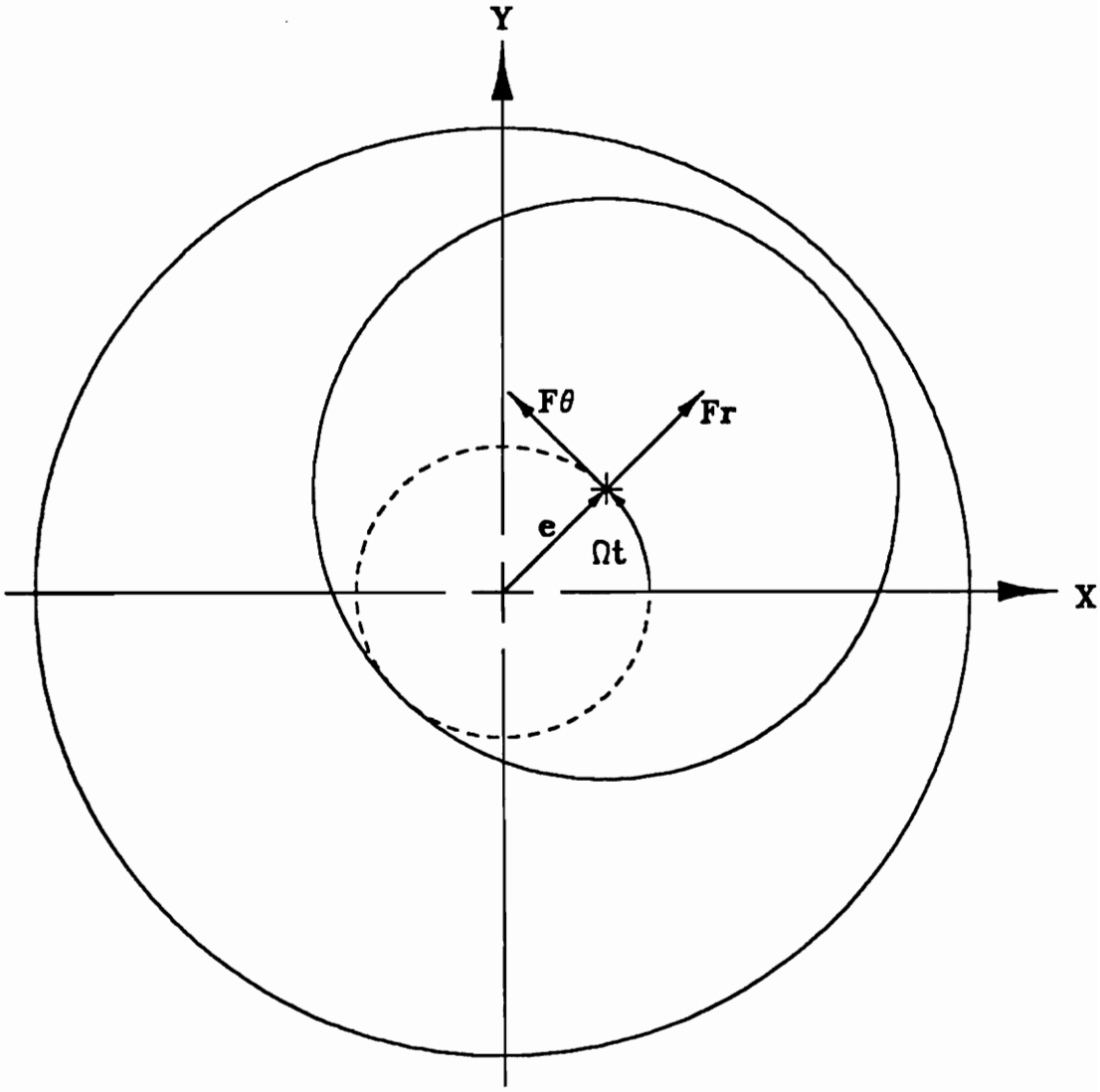

Figure 2. Forces on a Precessing Rotor: Radial and tangential force components on a rotor in a circular orbit about a centered position.

2. Literature Review

Investigations of the fluid forces developed inside annular pressure seals have increased significantly in the past two decades. Much of the recent research activity has been motivated by early vibration problems with the Space Shuttle main engine turbopumps in the mid 1970's (5,6). Advances in computer technology have also prompted detailed seal models which were previously unfeasible. A literature review by Barrett (7) lists 55 papers dealing with turbulent flow annular pump seals, 32 of which have been published since 1970. Flack and Allaire (8) review 58 papers concerning lateral forces on pump impellers. Ehric and Childs (9) also list an extensive bibliography with 38 references. The present review is intended to outline the most prominent papers and researchers in the field, and briefly discuss the merits and limits of each analysis.

It has been realized for quite some time that the presence of a seal in a turbomachine may affect the stability of the system by imposing an effective seal stiffness on the rotor. The first person to explain this phenomenon analytically was Lomakin (10) who in 1958 presented a static analysis neglecting shaft rotation and lateral velocity. Lomakin postulated that a small displacement of the rotor from its centered position would cause changes in the axial velocity distribution due to changes in radial clearance. The axial fluid velocity decreases in the smaller clearance region and increases in the larger clearance region due to changes in flow resistance. The axial pressure drop across the seal is caused by an entrance loss and a friction loss along the length of the seal. As

shown in Figure 3 on page 11 the entrance loss is greater in the high clearance region. The Bernoulli effect produces higher pressures in the low velocity region and lower pressures in the high velocity region. This pressure difference produces a restoring force which opposes the direction of displacement. Hence, an effective stiffness is produced which tends to center the rotor, a stabilizing effect. This radial stiffness is commonly referred to as the Lomakin effect.

Beginning in 1962 Yamada (11-13) published experimental results of leakage flow between co-axial cylinders with the inner cylinder rotating. For fully developed turbulent flow he presented a Blasius-type friction factor correlation based on the mean axial velocity Reynolds number (equation 2.1). For smooth walled surfaces the empirical constants in this equation were determined by Yamada to be $no = .065$ and $mo = -.24$. Hirs (14) later developed a bulk-flow theory for turbulent lubrication films using the same friction factor correlation with $no = .066$ and $mo = -.25$. This bulk-flow model has since been used almost universally in the literature for seals with turbulent incompressible flow.

$$f_w = no\, Re^{mo} \tag{2.1}$$

Undoubtedly the true pioneer in this field is Dr. Henry F. Black of Heriot-Watt University in Edinburgh, Scotland. His publications alone, and in conjunction with Jenssen and Cochrane, defined the forces developed by neck-ring and interstage seals in pumps. He also defined the vital dependency of pump rotordynamic behavior on seal characteristics. Black's 1969 paper (15) remains the definitive analysis of the phenomenon of rotor-stator motion across a clearance. In this paper he presented a bulk-flow theory where the circumferential bulk-flow velocity was assumed to be fully developed shear flow moving at one half the rotor surface speed. Assuming small perturbations about a centered position, Black solved the continuity and axial momentum equations subject to pressure boundary conditions which included a constant entrance loss coefficient of 0.5. He integrated the pressure distribution over the shaft surface to obtain the resultant force exerted by the flow on the shaft. Neglecting the shaft rotational speed, he then derived expressions for the direct stiffness, damping, and inertia coefficients, the direct stiffness being identical to that predicted

by Lomakin (10) for small rotor displacements. Limitations to this analysis included small length to diameter ratios (implied by the undisturbed circumferential flow), constant entrance losses, constant friction factors throughout the seal, and constant inlet swirl velocity.

Black and Jenssen (16) extended Black's original analysis to include "finite length" seals having appreciable length to diameter ratios. They also included the effect of shaft rotation by using a reference frame rotating at half the rotor speed. This allowed prediction of the cross-coupled coefficients when the solution was transformed back to an inertial frame of reference. Variable friction factors were also introduced based on Yamada's empirical results (11). Black et al. (17) combined prior seal analyses with equations developed for journal bearings (18,19) to examine the development of circumferential flow as a function of axial position in the seal. They concluded that the circumferential velocity approaches one half the rotor surface speed regardless of the inlet swirl. Predictions of the cross-coupled stiffness coefficient is generally reduced when development of circumferential flow is accounted for. Black and Cochrane (20) developed a semi-empirical approach to calculate the rotordynamic coefficients for serrated (circumferentially grooved) seals. Their approach introduces an equivalent length for the grooved sections of the seal such that the circumferential pressure gradients are reduced to the same extent as they are by the grooved sections replaced. The dynamic coefficients are then calculated using finite length correlations previously developed. Black spent the summer of 1979 working on the high pressure oxygen and hydrogen turbopumps in the Space Shuttle main engines with Drs. Barrett and Allaire (5) at the University of Virginia. Allaire (21) extended Black's plain seal model for eccentric seals with high axial Reynolds number in response to the Space Shuttle instability problem. Allaire later incorporated Black's grooved seal analysis (20) into his computer program (22).

Dr. Dara Childs at Texas A & M University became actively involved in the Space Shuttle rotordynamic problem by publishing a series of experimental and analytical papers on the analysis of turbulent flow annular seals. Dr. Childs and his colleagues at Texas A & M have hosted a number of workshops on rotordynamic instability problems in high performance turbomachinery and are responsible for much of the published literature in the past decade. Experimental test rigs

at Texas A & M (23) are capable of running extremely high Reynolds number flows to simulate conditions in the Space Shuttle hydrogen turbopump. This and a test facility at the University of Louisville (24) have provided much of the experimental data on turbulent seals in the United States. Childs' analytical work began with an analysis of short annular seals (25) based on Hirs' bulk-flow equations and a small perturbation analysis similar to that of Black. His results are the same as those of Black when a circumferential velocity of one half the rotor surface speed is used. Childs presented a finite length solution (26) and found that the solution did not reduce to the short seal solution when small length to diameter ratios were imposed. Childs attributes this to limitations of Hirs' governing equations to model unsteady flows for short seal lengths since Hirs' equations are based on steady state data. Childs later extended his analysis to include tapered seal geometries (27). Kilgore and Childs (28) presented experimental results for circumferentially grooved seals compared to an analytical model by Nordmann et al. (29). Other publications by Childs et al. include analyses for directionally homogeneous surface roughness (30), round hole pattern damper seals (31,32), and helically grooved stators (33,34).

Other researchers at Texas A & M include Dr. Clayton Nelson who made a comparison of Hirs' equation to Moody's equation for determining the rotordynamic coefficients of smooth and rough surface seals (35). He found that the two methods gave the same results for smooth seals but direct stiffness predictions were significantly higher when using Moody's equation for rough seals. This points out the limitation of using Hirs' equation, which is a function of Reynolds number only, to model friction factors which are a function of Reynolds number and relative roughness. Hirs' equation has been shown to underpredict direct stiffness for seals with rough rotor and stator surfaces. Nelson also developed an analysis to model eccentric seals using Fast Fourier Transforms to solve the governing equations (36,37). He found that the rotordynamic coefficients are fairly constant up to a static eccentricity ratio of 0.5. This agrees with the earlier results of Allaire et al. (21), however, Nelson's analysis shows better agreement with experimental data. His solution technique is also unique in that it uses Moody's equation and a Fast Fourier Transform. Scharrer

and Nelson (38) developed a model for partially tapered seals, i.e., seals consisting of tapered and parallel stator surfaces. No test data on this type of seal is available for comparison.

Extensive gas seal analyses have also been undertaken at Texas A & M, much of which offer insight into incompressible seals. Nelson (39) presented an analysis for compressible flow in tapered annular seals. His analysis was expanded by Elrod who included an entrance region friction factor model to more accurately describe the developing flow region at the seal inlet. Elrod et al. (40,41) were the first to publish a seal model which did not use a constant entrance loss coefficient to model these losses. Even finite difference analyses by Nordmann and Dietzen (42,43) use a constant entrance loss coefficient to establish the inlet boundary conditions. Their analysis assumes fully developed turbulent flow throughout the seal length. Elrod's analysis predicted the destabilizing cross-coupled stiffness of a seal better than Nelson's analysis. Since the developing flow region is often a substantial portion of the seal length, Elrod's model offers a more realistic approach to solving the flowfield and is equally applicable to incompressible seals. The presence of an entrance loss model in the current analysis is a direct result of Dr. Elrod's influence while on the faculty of Virginia Polytechnic Institute & State University.

Turbulent seal dynamics is also an area of active research in Japan. Takuzo Iwatsubo et al. (44-46) have published experimental and analytical results for smooth and grooved seal geometries. Their test rig can accurately control inlet preswirl as well as shaft motion, pressure drop, and clearance. Iwatsubo's smooth seal model is based on that of Childs with very similar results. His grooved seal analysis breaks the seal into a series of groove and land sections. The groove flow is separated by a turbulent shear layer into cavity flow and clearance flow. Iwatsubo assumes that the axial velocity of the cavity flow is half the axial velocity of the clearance flow. The present analysis uses Iwatsubo's segregated approach but does not make the same assumptions on axial cavity flow. An entrance loss model is also applied at each land inlet section. A more detailed review of the grooved seal analyses (20,28,29,42,44,46) is presented in Chapter 4.

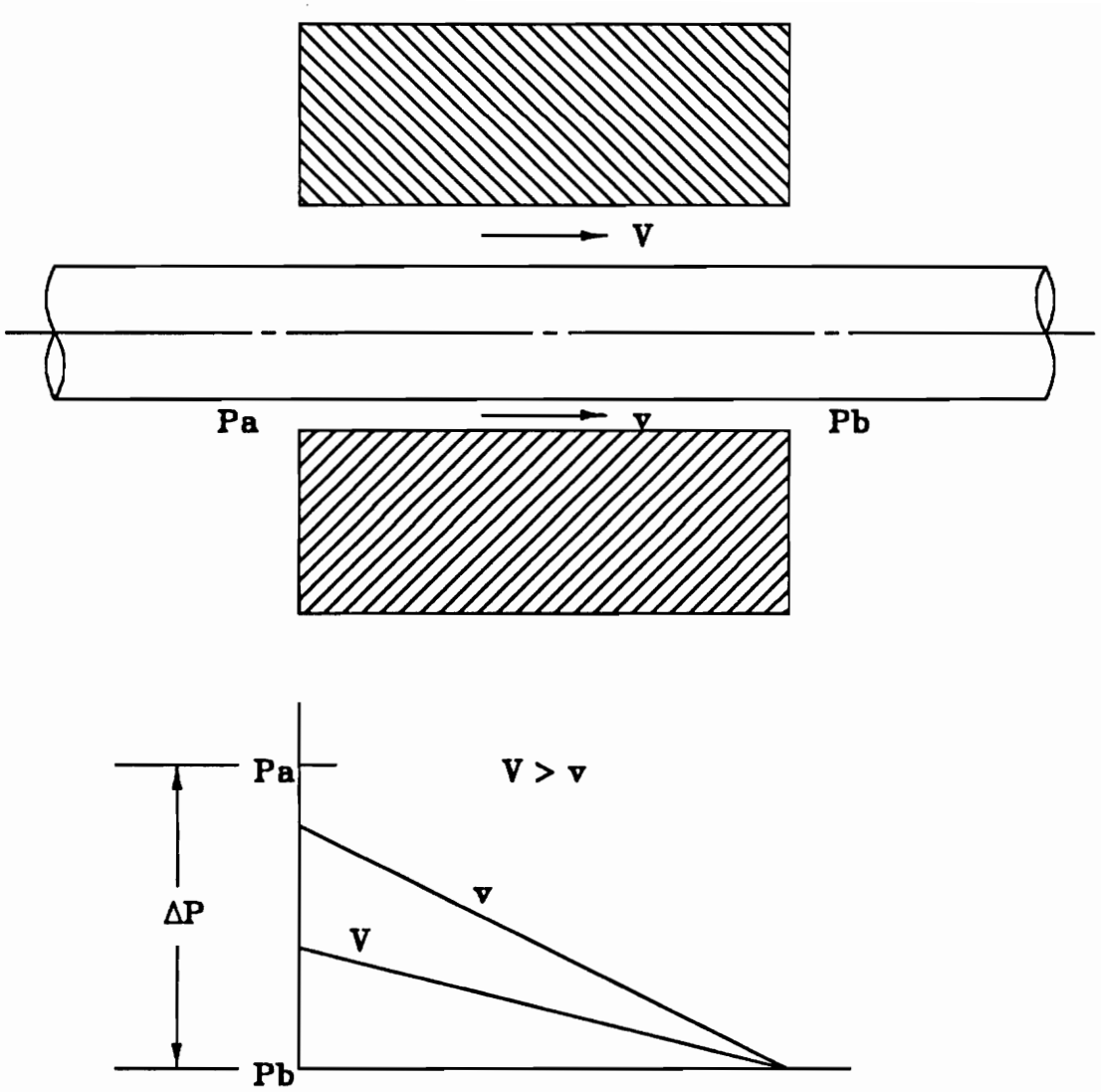

Figure 3. The Lomakin Effect for Annular Seals: Velocity decreases in the small clearance and increases in the large clearance. This causes a pressure difference due to the Bernoulli principle which acts as a restoring force, or effective seal stiffness.

3. An Analysis for Smooth Tapered Annular Seals

This chapter presents the equations and solution technique used to calculate the rotordynamic coefficients for smooth walled annular seals as shown in Figure 4 on page 19. Turbulent flow is assumed throughout the analysis.

GOVERNING EQUATIONS

The governing equations are developed for a differential fluid element as shown in Figure 5 on page 20. The equations are based on Hirs' theory for turbulent lubrication films (14). This theory does not attempt to model local fluctuations of flow velocity due to turbulence, nor does it explicitly describe the shape of the velocity profile in the radial direction. Only the bulk-flow relative to a surface or wall and the corresponding shear stress at that surface or wall under conditions of turbulent flow are considered and correlated. In addition, the viscous shear stress due to velocity gradients on the θ and z faces are assumed to be negligible. With these assumptions, the equations of continuity, axial and circumferential momentum may written as follows.

$$\frac{\partial H}{\partial t} + \frac{\partial}{\partial z}(V_z H) + \frac{1}{R}\frac{\partial}{\partial \theta}(V_\theta H) = 0 \qquad \text{Continuity}$$

$$H\left(\frac{\partial V_z}{\partial t} + \frac{V_\theta}{R}\frac{\partial V_z}{\partial \theta} + V_z\frac{\partial V_z}{\partial z}\right) = -\frac{1}{\rho}\left(H\frac{\partial P}{\partial z} + \tau_{sz} + \tau_{rz}\right) \qquad z \text{ - Momentum}$$

$$H\left(\frac{\partial V_\theta}{\partial t} + \frac{V_\theta}{R}\frac{\partial V_\theta}{\partial \theta} + V_z\frac{\partial V_\theta}{\partial z}\right) = -\frac{1}{\rho}\left(\frac{H}{R}\frac{\partial P}{\partial \theta} + \tau_{s\theta} + \tau_{r\theta}\right) \qquad \theta \text{ - Momentum}$$

These equations are expanded by introducing the perturbation variables composed of zeroth order and first order components as described in Appendix C. The perturbation variables take the following form.

$$H = H_0 + H_1 \qquad V_z = V_{z0} + V_{z1}$$
$$P = P_0 + P_1 \qquad V_\theta = V_{\theta 0} + V_{\theta 1}$$

The zeroth order variables describe a static, zero eccentricity flow condition where the rotor is perfectly centered in the seal and is not experiencing any rotor whirl. Under these conditions the derivatives with respect to t and θ will vanish and only derivatives in the axial direction remain. The zeroth order equations are derived by substituting the perturbation variables above into the governing equations and retaining those terms with only 0 subscripts and z-derivatives. The zeroth order equations then reduce to the following.

$$\frac{\partial}{\partial z}(V_{z0} H_0) = 0 \qquad \text{Zeroth Order Continuity}$$

$$H_0\left(V_{z0}\frac{\partial V_{z0}}{\partial z}\right) = -\frac{1}{\rho}\left(H_0\frac{\partial P_0}{\partial z} + \tau_{sz0} + \tau_{rz0}\right) \qquad \text{Zeroth Order } z \text{ - Momentum}$$

$$H_0 V_{z0}\frac{\partial V_{\theta 0}}{\partial z} = -\frac{1}{\rho}(\tau_{s\theta 0} + \tau_{r\theta 0}) \qquad \text{Zeroth Order } \theta \text{ - Momentum}$$

The first order variables describe small perturbations from the zeroth order solution caused by small clearance perturbations about a centered position as shown in Figure 6 on page 21. The first order solution defines the dynamic behavior of the flow due to small amplitude rotor whirl. The first order equations are derived by substituting the perturbation variables into the governing equations and retaining all terms with first order subscripts. Since the small perturbation analysis assumes that first order terms are much smaller than zeroth order terms, products of first order variables are neglected in the final equations shown below.

First Order Continuity

$$\frac{\partial H_1}{\partial t} + \frac{\partial}{\partial z}(V_{z1}H_0 + V_{z0}H_1) + \frac{1}{R}\frac{\partial}{\partial \theta}(V_{\theta 1}H_0 + V_{\theta 0}H_1) = 0$$

First Order z - Momentum

$$H_0\left(\frac{\partial V_{z1}}{\partial t} + \frac{V_{\theta 0}}{R}\frac{\partial V_{z1}}{\partial \theta} + V_{z0}\frac{\partial V_{z1}}{\partial z} + V_{z1}\frac{\partial V_{z0}}{\partial z}\right) + H_1 V_{z0}\frac{\partial V_{z0}}{\partial z} = \frac{-1}{\rho}\left(H_0\frac{\partial P_1}{\partial z} + H_1\frac{\partial P_0}{\partial z} + \tau_{sz1} + \tau_{rz1}\right)$$

First Order θ - Momentum

$$H_0\left(\frac{\partial V_{\theta 1}}{\partial t} + \frac{V_{\theta 0}}{R}\frac{\partial V_{\theta 1}}{\partial \theta} + V_{z0}\frac{\partial V_{\theta 1}}{\partial z} + V_{z1}\frac{\partial V_{\theta 0}}{\partial z}\right) + H_1 V_{z0}\frac{\partial V_{\theta 0}}{\partial z} = -\frac{1}{\rho}\left(\frac{H_0}{R}\frac{\partial P_1}{\partial \theta} + \tau_{s\theta 1} + \tau\right.$$

LOSSES DUE TO FRICTION AND ENTRANCE EFFECTS

The pressure drop across the seal is caused by wall friction and sudden contraction effects at the seal inlet. The solution of the governing equations depends largely on the modelling technique used to predict these losses. Hirs' bulk-flow theory uses a Blasius-type friction factor to model the wall shear stress for fully developed turbulent flow as follows.

$$\tau_w = f_w \frac{1}{2} \rho V^2$$

where $f_w = no\, Re^{mo}$

$$Re = \frac{VH}{\nu}$$

and $V =$ flow velocity relative to wall

The expanded form of the shear stress equations is shown in Appendix D. The Reynolds number is based on the radial clearance, H. This is consistent with the Reynolds number as defined by Hirs (14) for a thin fluid annulus where $H \ll R$. Some authors elect to use a Reynolds number based on the hydraulic diameter, $2H$. This is the source of some confusion in the literature since different Hirs' coefficients are required depending on the Reynolds number definition. There is no effect on the governing equations as long as the proper coefficients are used. Hirs' coefficients for smooth surfaces for Reynolds numbers below 10^5 are shown below.

$Re = \frac{HV}{\nu}$	$Re = \frac{2HV}{\nu}$
$no = .066$	$no = .079$
$mo = -.25$	$mo = -.25$

Hirs' coefficients are used to model the friction factors for fully developed turbulent flow. In the developing flow region however, friction factors are significantly higher due to sudden contraction effects near the inlet and boundary layer growth near the walls. Most of the published seal analyses use a constant entrance loss coefficient, ζ, to model the entrance loss, λ, as follows.

$$\lambda = \zeta \frac{1}{2} \rho V^2$$

All of the flow inside the seal is then treated as fully developed turbulent flow. Various experimental studies (47-50) of turbulent flow in the entrance region of pipes concluded that the flow becomes fully developed at 35-40 diameters from the inlet. Deissler (51) presented similar results for flow between flat parallel plates. Using radial clearance as the effective diameter for seal flow, 40 diameters is often a substantial portion of the seal length. Elrod et al. (40) showed that pred-

ictions of cross coupled stiffness were improved by modelling the entrance region friction factor as a function of axial distance rather than an abrupt entrance loss. In the present analysis, the axial coordinate, z, is introduced into the friction factor equation as follows.

$$f_d = no\left(\frac{VH}{\nu}\right)^{mo}\left(\frac{z}{40H}\right)^{-.25}$$

For smooth walled coefficients ($mo = -.25$) this reduces to the following.

$$f_d = no\left(\frac{Vz}{40\nu}\right)^{mo}$$

This agrees with the entrance region friction factor used by Elrod et al. (40). Note that when $z = 40H$, the entrance region friction factor matches the fully developed value. Beyond $z = 40H$ the entrance loss model is not applied and the fully developed value is used. Figure 7 on page 22 shows the ratio of developing friction factors to fully developed friction factors versus non-dimensional axial distance. This figure agrees well with Deissler's (51) results for flow between parallel plates. Note that the friction factor ratio is very close to unity at 20 clearances, even though 40 clearances is used as the fully developed transition point. This is also in agreement with experimental results. The mean velocity profile is generally used as the criteria for fully developed flow although velocity profiles continue to change after wall shear stresses are relatively stable.

ZEROTH AND FIRST ORDER SOLUTIONS

The zeroth and first order solutions are obtained by numerical integration using the Adams Predictor-Corrector method. The boundary conditions are determined by the inlet and exit pressures. Inlet static pressure measurements are generally taken where axial velocity is negligible, although inlet preswirl is present. The static pressure at the seal inlet then includes a pressure drop due to Bernoulli's equation.

$$P_{0(z=0)} = P_a - \frac{1}{2}\rho V_{z0}^2$$

Exit static pressure measurement generally includes the effects of axial and circumferential velocity and is used directly in the analysis. These inlet and exit pressure boundary conditions are sufficient to establish the zeroth order solution. The solution is obtained by an iterative procedure to determine the axial velocity distribution which will balance the shear forces with the pressure forces on the seal. The zeroth order solution determines the nominal (centered) velocity distribution and leakage flow for the seal. The zeroth order solution is then used to calculate the coefficients required for the first order solution (Appendix E).

The first order solution is found by solving a system of six first order linear differential equations (Appendix E). The six unknown variables in these equations define the first order perturbation variables, V_{z1}, $V_{\theta 1}$, and P_1. The boundary conditions imposed for this solution are as follows.

1. The exit perturbation pressure is zero, i.e., $P_1(L) = 0$.

2. The inlet circumferential velocity perturbation is zero, i.e., $V_{\theta 1}(0) = 0$.

3. The inlet pressure drop is defined by Bernoulli's Equation:

$$(P_0 + P_1)_{(z=0)} = P_a - \frac{1}{2}\rho(V_{z0} + V_{z1})^2$$

$$(P_0 + \frac{1}{2}\rho V_{z0}^2 - P_a) + P_1 = -\rho V_{z0} V_{z1} - \frac{1}{2}\rho V_{z1}^2$$

Neglecting products of first order terms: $P_1 = -\rho V_{z0} V_{z1}$.

These boundary conditions are sufficient for solving the first order system of equations using the Adams Predictor-Corrector numerical integration scheme. The six perturbation coefficients will in general vary with axial location but are constant at any axial plane. This is a direct result of the assumptions used in defining the form of the perturbation variables in Appendix C. The forces on

the rotor are found by numerically integrating the dynamic pressure distribution defined by the first order perturbation pressure coefficients. With reference to Figure 3 and Figure 6, the radial and tangential force components are defined by the following integrals.

$$-F_r = \int_0^L \int_0^{2\pi} (P_{1c}\cos\phi + P_{1s}\sin\phi)\cos\phi R d\phi dz$$

$$-F_\theta = \int_0^L \int_0^{2\pi} (P_{1c}\cos\phi + P_{1s}\sin\phi)\sin\phi R d\phi dz$$

Carrying out the integration with respect to ϕ the force equations may be written as follows.

$$-F_r = \pi R \int_0^L P_{1c} dz$$

$$-F_\theta = \pi R \int_0^L P_{1s} dz$$

The integration with respect to z is carried out numerically using a third order cubic spline integration scheme. Comparing the force equations above to equations 1.3 and 1.4, it is apparent that more than one whirl frequency must be analyzed to determine all six rotordynamic coefficients. By anaylyzing at least three different whirl frequencies at constant Reynolds number, the rotordynamic coefficients may be determined by fitting a parabola through a plot of force versus whirl angular velocity.

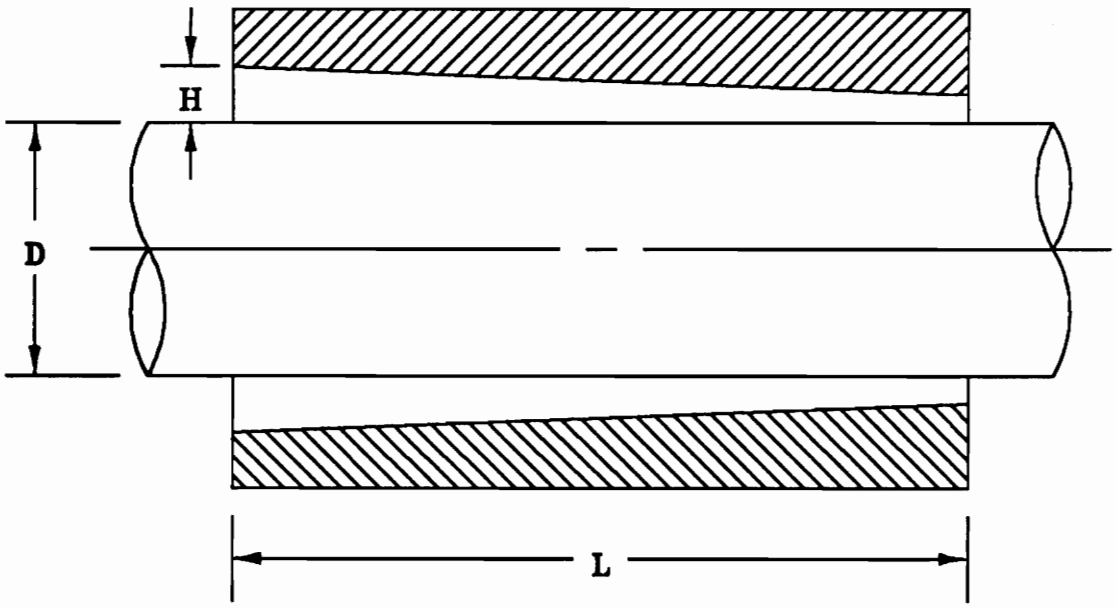

Figure 4. Smooth Tapered Annular Seal: Cross section of a smooth walled tapered seal.

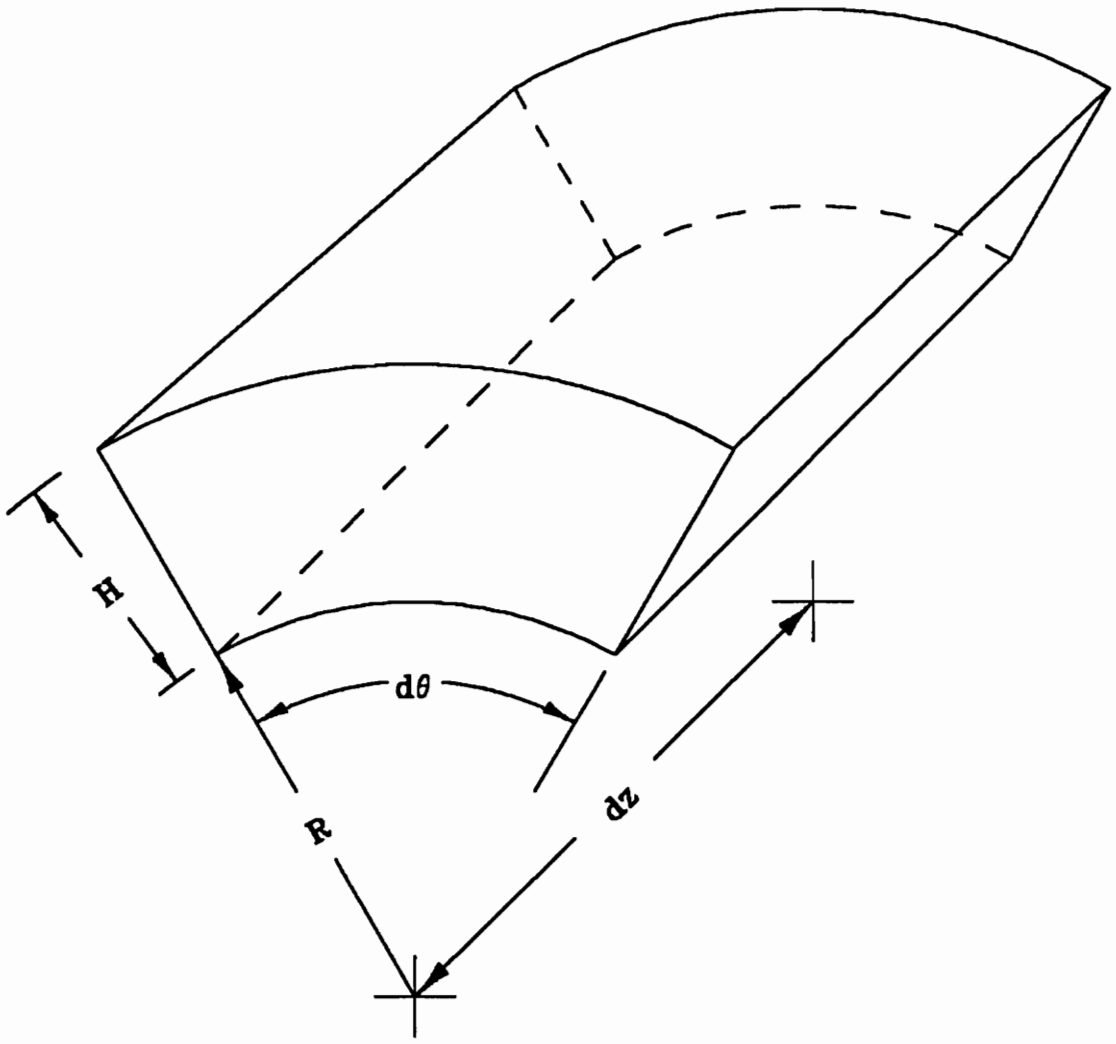

Figure 5. Differential Seal Element: Annular control volume for bulk-flow equations.

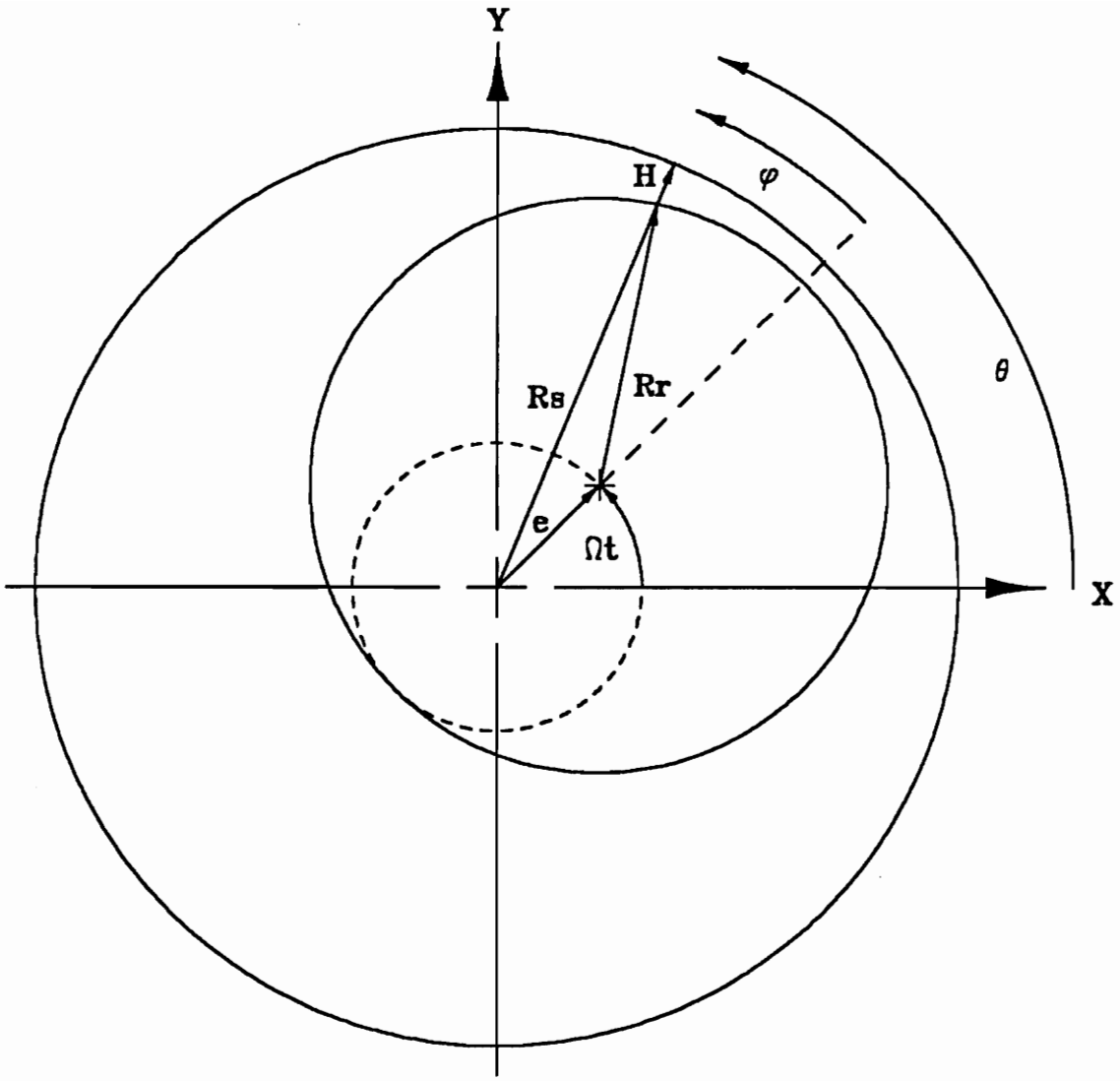

Figure 6. Seal Clearance for a Circular Whirl Orbit: $H = H_0 - e \cos \phi$.

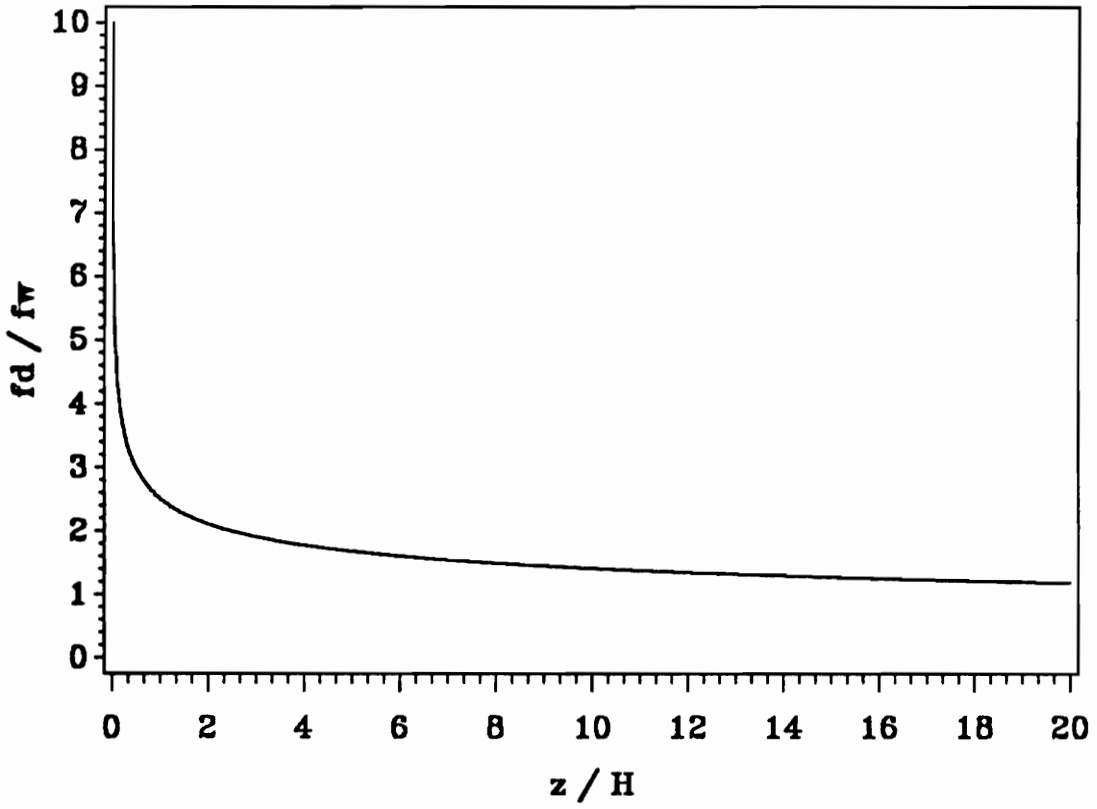

Figure 7. Entrance Loss Model: Losses due to sudden contraction at seal entrance.

4. An Analysis for Circumferentially Grooved Seals

This chapter presents the assumptions used to expand the smooth seal analysis to include grooved seal geometries. Two types of seals are considered, the smooth rotor / grooved stator configuration shown in Figure 8 on page 27, and the grooved rotor / smooth stator shown in Figure 9 on page 28. Grooved seals are widely used because of their excellent sealing properties and stabilizing effects. However, published anaylses for determining the rotordynamic characteristics of grooved seals are scarce. Black and Cochrane (20) developed an analysis for serrated (grooved) seals based on their earlier work for seals with high L/D ratios. They postulated that the main effect of a circumferential groove was to allow faster equilibration of the circumferential pressure gradients. By examining the circumferential momentum equation, they defined an equivalent L/D ratio which would reduce the circumferential pressure gradient to the same extent as the grooved section it replaced. Their results showed reasonable agreement with experimental data for L/D = 1.0, but did not agree well with shorter seals (L/D = .5 and .23). Their analysis was also limited to grooved stator / smooth rotor geometries. Allaire (22) later incorporated Black's analysis into his seal model which combined eccentric and grooved seal analyses. Kilgore and Childs (28) developed a grooved seal model based on that of Nordmann et al. (29). Their analysis is an extension of Childs' bulk-flow analysis (26) and uses Hirs' coefficients to define different friction factors in the axial and circumferential directions. An average groove depth is introduced to account for the flow in the

grooves. Their analysis also shows reasonable agreement with experimental data, but depends entirely on inputting the proper Hirs' coefficients for a grooved seal. These coefficients are determined empirically for each groove geometry and are generally not available in the literature. This poses a serious limitation to the design engineer. Their analysis is also limited to grooved stator / smooth rotor configurations. Dietzen and Nordmann (42) used their finite difference model to analyze grooved seals. They did not show comparisons to experimental data but presented parametric studies to show the effect of groove depth on leakage and rotordynamic coefficients. The predicted leakage showed the same trends found by Black (20). The cross coupled stiffness and damping were reduced, which also shows the proper trends.

Iwatsubo et al. (44,46) presented a bulk-flow analysis for grooved seals where the groove flow is separated into free stream (clearance) flow and cavity (groove) flow as shown in Figure 10 on page 29. Iwatsubo defines the shear stress between the two flows using theory for a turbulent shear layer. He assumes that the axial velocity in the cavity flow is one-half the axial velocity in the clearance flow. The circumferential velocity in the cavity flow is determined from a momentum balance between the wall shear and the shear layer. Iwatsubo's analysis does not require Hirs' coefficients for grooved geometries and can be applied to grooved rotor / smooth stator configurations as well. Large amounts of computer storage and run time associated with finite difference methods are also avoided. Iwatsubo's results show good qualitative agreement with data from his seal test rig, but quantitatively the model needs improvement. The present analysis uses the segregated approach of Iwatsubo but does not make the same assumptions on cavity flow. The one-half axial velocity assumption used by Iwatsubo seems unreasonable at large groove depths. Instead, a semi-empirical method is employed to determine the friction factors in the groove and an entrance loss model is applied at each land entrance region as well.

Figure 10 on page 29 shows a typical groove section. The divergence angle, α, is defined as the half-angle for a turbulent shear layer. There is some discrepancy in the literature as to what this angle should be. Iwatsubo (44) uses $\alpha = 4°$. Bejan (52) uses $3.5° \leq \alpha \leq 10°$ depending on exactly how the divergence angle is defined. The present analysis assumes $\alpha = 5°$. In a turbulent shear

layer the flow continues to diverge at a constant angle. In the groove section, the flow is assumed to follow a parabolic profile with a tangent at the land section equal to the shear layer divergence angle. This profile is used in the continuity equation to determine the axial and circumferential velocity distributions.

The friction factor for the fluid to fluid interface at the shear layer is a function of the turbulent eddy viscosity and is determined experimentally. Iwatsubo (46) uses $f_s = 0.093$. To use this friction factor the circumferential and axial velocity in the cavity flow must be known or assumed. It is clear that the friction factor in the groove will vary between the two extreme values where f_w is the value for fully developed wall friction (no groove) and f_s is the value for a pure turbulent shear layer (deep groove). Based on experimental studies by Yamada (12), the relationship between these two extremes is modelled as an exponential function of the non-dimensional groove depth. This relationship is plotted in Figure 11 on page 30. As can be seen, for $D_s/L_s = 0$ the groove friction factor reduces to that for a smooth walled seal. For deep grooves, a value of $D_s/L_s = 6$ was chosen as the point where the friction factor reaches 99% of the value for a turbulent shear layer. This was an empirical choice based on matching available test data for grooved seals. The friction factor model for the groove assumes that the groove flow relative to the groove surface is essentially zero for deep groove geometries. For a grooved stator this has the effect of "trapping" the swirl flow and reducing the cross-coupled coefficients. For a grooved rotor just the opposite occurs. The rotor "traps" the fluid and induces high circumferential velocities. This effect can be seen in Figure 12 on page 31 where the circumferential velocity is plotted along the length of the seal for different seal geometries. As shown, the circumferential velocity approaches a value lower than half the rotor speed with a grooved stator but approaches a higher value with a grooved rotor.

The exponential decay relationship shown in Figure 11 is also used to scale the entrance loss effects at the land entrance regions of each groove. That is, for zero groove depth the entrance loss model is only applied at the seal inlet, and for a deep groove ($D_s/L_s = 6$) the full entrance loss model shown in Figure 7 is applied. For groove depths between these two values, the entrance loss model is scaled in the same fashion as the friction factor model. This guarantees that the grooved seal model

will reduce to the smooth seal model for very small groove depths, and also predicts that extremely deep grooves ($D_g/L_g > 6$) will have little additional effect on seal leakage and rotordynamic coefficients. Results of the present analytical model for circumferentailly grooved seals are presented in the next chapter.

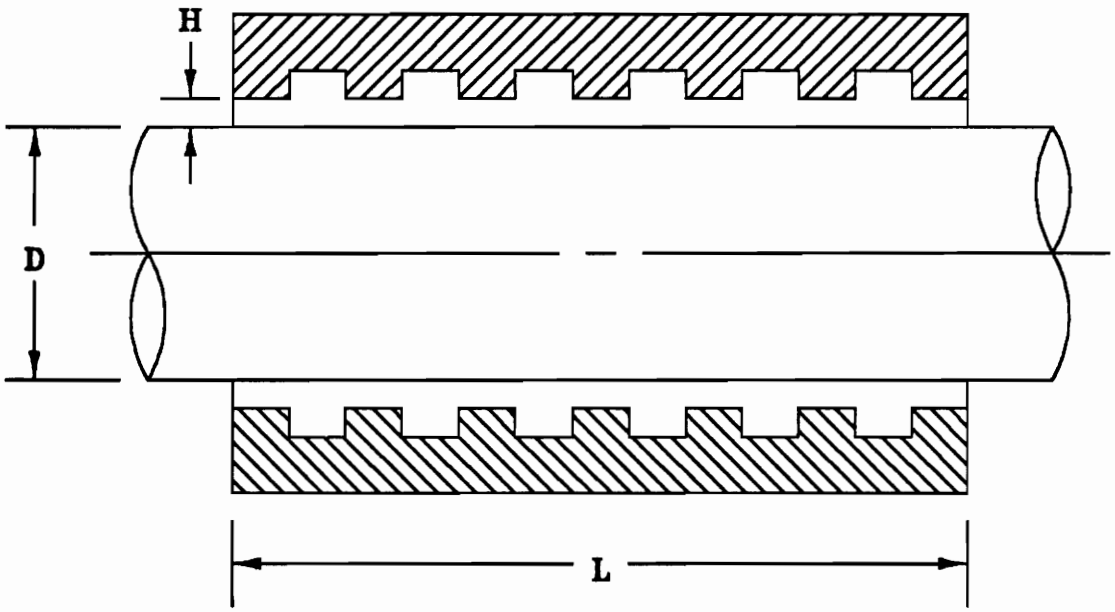

Figure 8. Smooth Rotor / Grooved Stator: Typical cross section of a seal with circumferentially grooved stator.

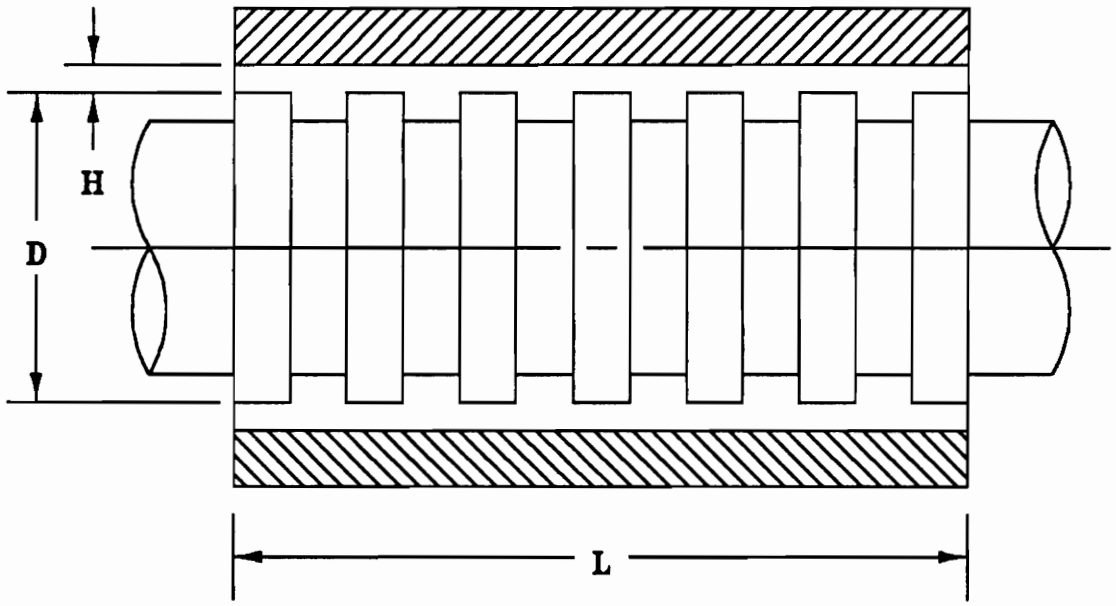

Figure 9. Grooved Rotor / Smooth Stator: Typical cross section of a seal with circumferentially grooved rotor.

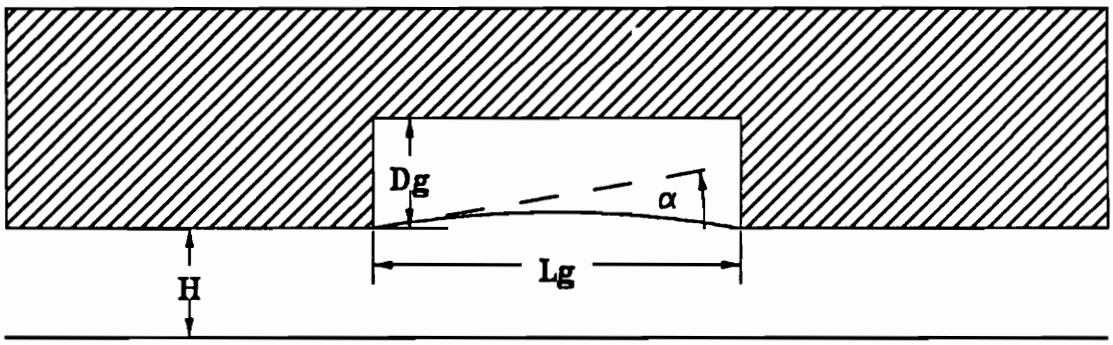

Figure 10. Typical Groove Geometry: Groove flow is separated into free stream (clearance) flow and flow in the groove (cavity flow). Friction in the groove section is modelled by the turbulent shear layer dividing the two flows. The divergence angle, α, for a turbulent shear layer is $\simeq 5°$.

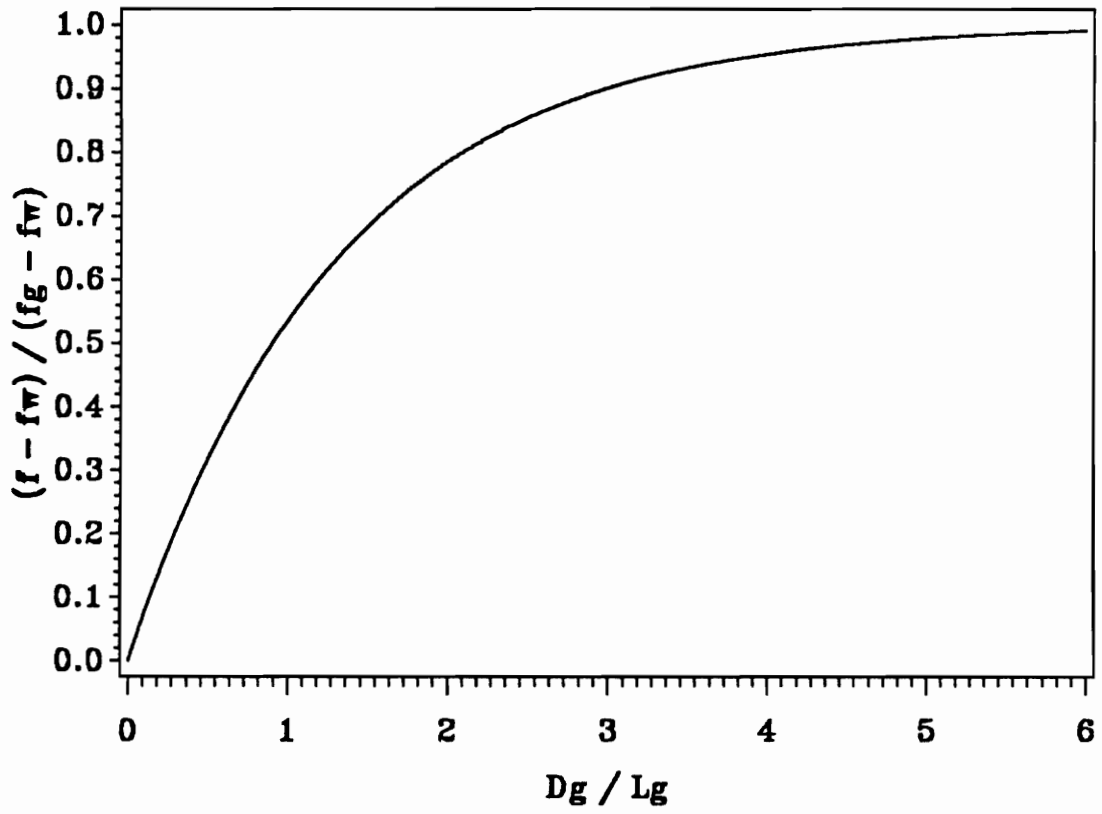

Figure 11. **Friction Factor Model for Grooved Sections:** The friction factor varies exponentially as a function of the non-dimensional groove depth. For zero groove depth the friction factor equals the wall value from Hirs' equation, f_w. The friction factor asymptotically approaches the value for a turbulent shear layer, f_g, as the groove depth increases.

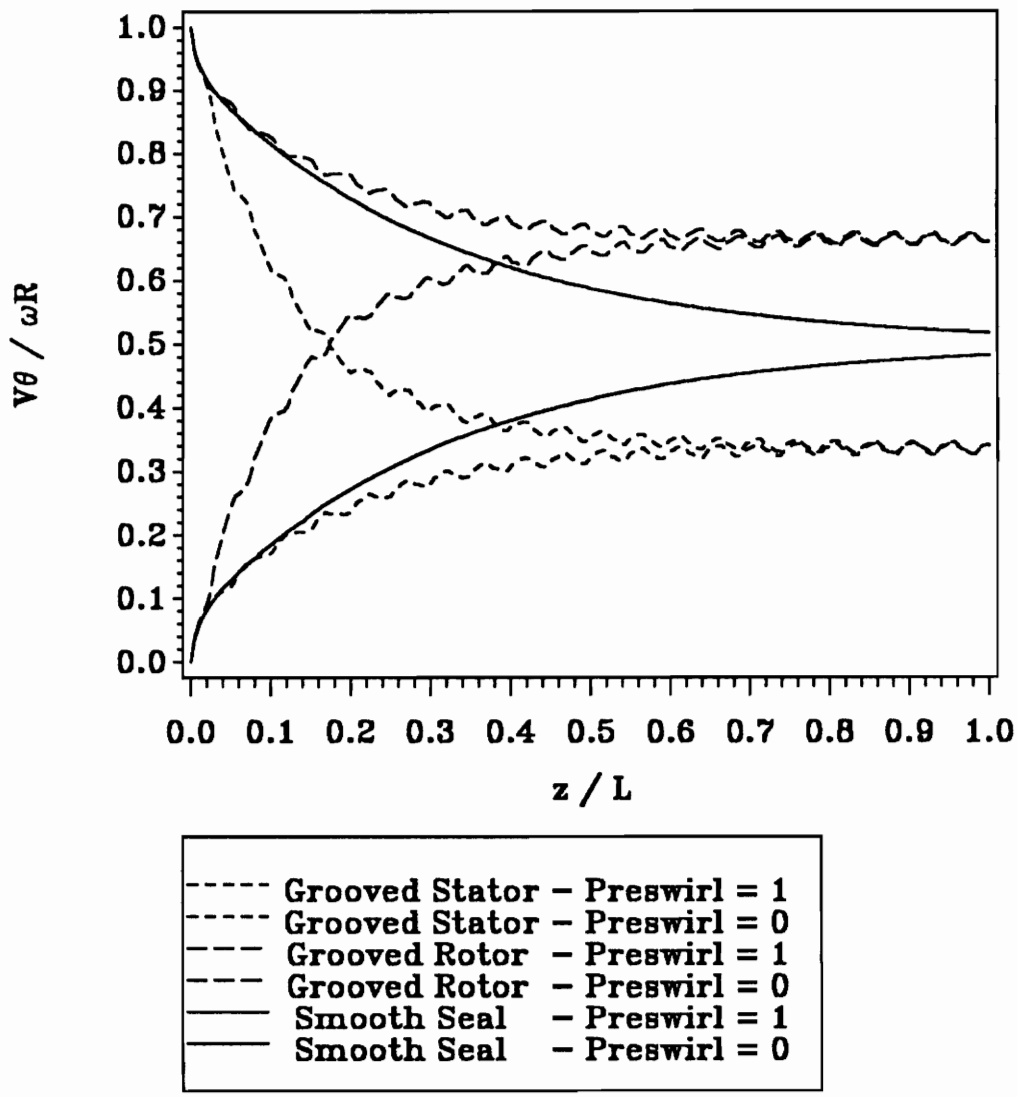

Figure 12. Effect of Grooves on Swirl Velocity: Circumferential velocity approaches $R\omega/2$ for smooth seals. High friction factors in the grooved sections slows the swirl flow down for grooved stators and increases the swirl flow for grooved rotors.

5. Comparisons to Experimental Results

In this chapter the results of the seal model are presented and compared to experimental data for smooth and grooved seal geometries. The experimental data has been taken from Childs (27) and Iwatsubo (45,46). Experimental measurement of the dynamic forces developed in annular seals is a difficult task and is prone to high experimental uncertainty. The test procedure generally consists of a controlled excitation of the rotor - stator interface either by moving the stator while holding the rotor fixed or vice versa. Displacement probes measure the position of the rotor and a timing signal records the phase angle. Pressure probes are placed axially and circumferentially around the seal housing to measure the radial and tangential forces on the rotor. Alternately, dynamic load cells are sometimes used in conjunction with the pressure probes for cross checking test results. The fluid properties and pressure drop must be carefully controlled to minimize changes in Reynolds number during the test. The accuracy of the test data depends on the ability to simultaneously record rotor displacement, phase angle, and pressure distribution around the seal. Integration of the pressure field yields the tangential and radial force components for a given shaft speed, whirl velocity, and pressure drop. As explained in Chapter 1, in order to extract the six rotordynamic coefficients from the data, the test rig must have the capability to independently vary the whirl velocity while holding shaft speed and pressure drop constant. A series of at least three data points is needed to fit a quadratic curve through a plot of force versus whirl angular velocity.

The coefficients of the curve fit will yield the rotordynamic coefficients as shown in equations 1.3 and 1.4.

Experimental data for rotordynamic coefficients is not abundant in the literature. Two test rigs at Texas A & M University (23) have provided a broad base of data for smooth tapered seals, however the published results for incompressible seals are limited to tests with synchronous rotor excitation. For this reason, the published data from Childs shows results for seal leakage, radial, and tangential forces only. The rotordynamic coefficients cannot be determined independently from the data. Iwatsubo's test rig (45) has the capability to independently vary whirl velocity and shaft speed and hence determine the rotordynamic coefficients. His published results for smooth and grooved seals have been used as the basis of comparison in this chapter, along with radial and tangential force comparisons from Childs.

Childs (27) published test results for three tapered seal geometries, referred to as Taper 1, Taper 2, and Taper 3. Geometric dimensions for these seals is shown in Tables 1 and 2. Test results for seal leakage, radial, and tangential forces are shown in Table 3 in SI units. Results of the current analytical model, referred to as PSEAL 1.2, are shown in Table 4 in SI units. Tables 5 and 6 show test data and model results respectively converted to USCS units. Test results from Taper 2 have been plotted in Figures 13-15 and are also representative of the results for Taper 1 and Taper 3. Figure 13 on page 43 shows the radial forces versus running speed for three different values of Reynolds number. The model shows the proper trends but does not match the test values. The discrepancy between model and test data increases at higher Reynolds number, suggesting that the values of Hirs' coefficients used in the friction factor model may be the source of the difference. Childs' model (27) shows the same tendency and it was his conclusion that surface roughness within the seal which exceeds that predicted by Hirs' coefficients may account for the discrepancy. By choosing suitable values for Hirs' coefficients, it is likely that the agreement between test and analytical values could be improved. Figure 14 on page 44 shows results for tangential forces. The same trends and general conclusions can be drawn from this figure. Seal leakage is plotted in Figure 15 on page 45. In general, these figures show favorable results of the model in predicting

seal behavior for smooth geometries. The model predicts the proper trends with running speed and shows only moderate discrepancies from actual test values.

Tables 7 and 8 show seal geometries for three seals tested by Iwatsubo et al. (45,46). Seal 1 is a smooth seal with constant clearance and L/D = 0.5. Seal 2 has approximately the same overall dimensions with the addition of 10 circumferential grooves. Seal 3 has the same groove dimensions as Seal 2 with 20 grooves. All seals were tested with water as the test fluid at various values of inlet preswirl, shaft velocity, and pressure drop. Selected data points along with predictions from the analytical model are presented in tables 9-12. Figure 16 on page 46 shows direct and cross-coupled stiffness results for Seal 1 with zero preswirl. Even though the model overpredicts direct stiffness, the relative levels and trends show good agreement with the test results. Note the increase in cross-coupled stiffness with shaft velocity. This is a well documented effect in seals due to the increased swirl velocity at higher running speeds. Figure 17 on page 47 shows results for direct and cross-coupled damping. Direct damping for this case is substantially overpredicted, however the relative levels and trends are still encouraging. Figure 18 on page 48 shows results for direct inertia. The model appears to underpredict direct inertia for this case, however, the data scatter makes it difficult to reach a firm conclusion. Overall the model shows the ability to predict proper trends and shows only moderate discrepancies from experimental data.

Test results for Seal 2 are presented in Figures 19-24. Unfortunately these results cannot be directly compared to those from Seal 1 since different parameters were changed during the test. Seal 1 was tested at a constant preswirl of 0% while varying the shaft speed. Seal 2 was tested at a constant shaft speed of 500 rpm while varying the inlet preswirl. Figure 19 on page 49 shows the radial forces for Seal 2 versus whirl velocity for three values of inlet preswirl. This figure emphasizes the difficulty of extracting rotordynamic coefficients by fitting a parabola through scattered data. The difference in levels between the data and the model results from the model's tendency to overpredict direct stiffness. Figure 20 on page 50 shows results for tangential forces. Note that the data is more linear because the cross-coupled inertia term is negligible. The increase in cross-coupled stiffness with increasing preswirl can be seen as a difference in levels among the three data sets. Seal leakage

for Seals 1 and 2 is plotted in Figure 21 on page 51 The model again predicts the proper effects of pressure drop and the addition of circumferential grooves with moderate discrepancies in the absolute levels. Curve fits of the experimental data provide the rotordynamic coefficients shown in Figures 22-24. Comparisons to the model again show the prediction of proper trends, especially in the cross-coupled terms, and moderate agreement in overall levels.

Table 1. Seal Geometry from Childs (27) in SI Units: Smooth tapered seal geometry for data plotted in Figures 13-15.

Seal	L cm	D cm	H inlet cm	H exit cm
Taper 1	4.996	10.16	.0889	.0508
Taper 2	4.996	10.16	.1079	.0508
Taper 3	4.996	10.16	.1125	.0508

Table 2. Seal Geometry from Childs (27) in USCS Units: Smooth tapered seal geometry for data plotted in Figures 13-15.

Seal	L in	D in	H inlet in	H exit in
Taper 1	1.967	4.000	.0350	.0200
Taper 2	1.967	4.000	.0425	.0200
Taper 3	1.967	4.000	.0443	.0200

Table 3. Test Data from Childs (27) in SI Units: Experimental results for three smooth tapered seals. Data from taper 2 is compared to PSEAL 1.2 in Figures 13-15.

Run	$Re_z \cdot 10^{-3}$ $\rho V_z H/\mu$	ΔP kN / m^2	ω rpm	ρ kg / m^3	$\mu \cdot 10^3$ N • s / m^2	F_r/e kN / m	F_θ/e kN / m	$\dot{Q}$ kg / s
Taper 1								
1	13.48	1010.	3450.	1003.	1.245	-3640.	-2500.	5.35
2	13.49	1010.	2442.	1003.	1.245	-3670.	-1780.	5.35
3	13.34	979.	1200.	1003.	1.245	-3580.	-929.	5.29
4	10.01	558.	3486.	1003.	1.245	-2240.	-1880.	3.97
5	10.26	579.	2448.	1003.	1.245	-2210.	-1180.	4.06
6	10.16	572.	1302.	1009.	1.288	-2070.	-725.	4.06
7	7.60	345.	3510.	1003.	1.245	-1420.	-1360.	3.01
8	8.94	427.	2292.	1003.	1.245	-1550.	-1130.	3.54
9	8.51	372.	1152.	1003.	1.245	-1430.	-621.	3.37
10	4.86	152.	3786.	1009.	1.288	-535.	-1080.	2.01
11	5.01	145.	3450.	1003.	1.245	-599.	-986.	1.99
12	5.03	138.	2370.	1003.	1.245	-538.	-695.	2.00
13	4.84	124.	1236.	1003.	1.245	-522.	-348.	1.99
Taper 2								
1	16.35	717.	3750.	998.4	1.024	-2270.	-2040.	4.83
2	16.35	717.	2479.	998.4	1.024	-2220.	-1360.	4.82
3	16.60	730.	1681.	998.4	1.024	-2330.	-988.	4.89
4	16.45	737.	943.	998.4	1.024	-2330.	-707.	4.85
5	11.10	338.	4152.	998.4	1.024	-1040.	-1480.	3.28
6	10.95	345.	3390.	998.4	1.024	-1100.	-1250.	3.22
7	11.15	331.	2449.	998.4	1.024	-1010.	-896.	3.28
8	10.20	338.	1255.	998.4	1.024	-1100.	-506.	3.30
9	5.55	89.6	3371.	998.4	1.024	-409.	-632.	1.65
10	5.10	82.7	2479.	998.4	1.024	-269.	-467.	1.65
11	5.40	96.5	1818.	998.4	1.024	-330.	-387.	1.60
12	5.55	82.7	925.	998.4	1.024	-300.	-185.	1.65
Taper 3								
1	14.90	496.	3792.	996.7	0.861	-1503.	-1793.	4.07
2	15.10	462.	2844.	996.7	0.861	-1568.	-1233.	4.11
3	14.85	483.	1932.	996.7	0.861	-1544.	-859.	4.04
4	14.90	483.	984.	996.7	0.861	-1585.	-497.	4.06
5	12.60	510.	3366.	998.4	1.024	-1476.	-1672.	4.06
6	12.50	493.	2832.	998.4	1.024	-1435.	-1004.	3.95
7	12.70	482.	1956.	998.4	1.024	-1652.	-967.	4.10
8	12.50	462.	960.	998.4	1.024	-1588.	-463.	4.06
9	9.85	221.	3780.	996.7	0.861	-559.	-1160.	2.68
10	9.75	207.	2886.	996.7	0.861	-627.	-774.	2.66
11	9.70	207.	936.	996.7	0.861	-706.	-264.	2.63
12	4.81	89.6	3630.	998.4	1.024	-483.	-686.	1.56
13	5.45	96.5	3153.	998.4	1.024	-326.	-666.	1.77
14	5.35	89.6	2028.	998.4	1.024	-257.	-408.	1.74
15	5.10	75.8	1026.	998.4	1.024	-270.	-177.	1.65

Table 4. Results from PSEAL 1.2 in SI Units: Analytical results for three smooth tapered seals. Data from taper 2 is compared to experimental results in Figures 13-15.

Run	$Re_z \cdot 10^{-3}$ $\rho V_z H/\mu$	ΔP kN / m^2	ω rpm	ρ kg / m^3	$\mu \cdot 10^3$ N • s / m^2	F_r/e kN / m	F_θ/e kN / m	$\dot{Q}$ kg / s
Taper 1								
1	14.33	1010.	3450.	1003.	1.245	-2500.	-2199.	5.75
2	14.42	1010.	2442.	1003.	1.245	-2618.	-1555.	5.78
3	14.25	979.	1200.	1003.	1.245	-2628.	-751.	5.71
4	14.39	558.	3486.	1003.	1.245	-1267.	-1646.	4.17
5	10.71	579.	2448.	1003.	1.245	-1439.	-1176.	4.29
6	10.38	572.	1302.	1009.	1.288	-1505.	-622.	4.31
7	7.97	345.	3510.	1003.	1.245	-698.	-1298.	3.19
8	9.10	427.	2292.	1003.	1.245	-1041.	-944.	3.65
9	8.55	372.	1152.	1003.	1.245	-697.	-442.	3.43
10	4.78	152.	3786.	1009.	1.288	-183.	-899.	1.98
11	4.86	145.	3450.	1003.	1.245	-197.	-804.	1.95
12	4.87	138.	2370.	1003.	1.245	-266.	-549.	1.95
13	4.73	124.	1236.	1003.	1.245	-297.	-272.	1.90
Taper 2								
1	15.28	717.	3750.	998.4	1.024	-1736.	-1821.	5.05
2	15.42	717.	2479.	998.4	1.024	-1887.	-1195.	5.09
3	15.63	730.	1681.	998.4	1.024	-1993.	-814.	5.16
4	15.75	737.	943.	998.4	1.024	-2055.	-457.	5.20
5	10.11	338.	4152.	998.4	1.024	-645.	-1392.	3.34
6	10.33	345.	3390.	998.4	1.024	-750.	-1144.	3.41
7	10.21	331.	2449.	998.4	1.024	-804.	-804.	3.37
8	10.45	338.	1255.	998.4	1.024	-906.	-412.	3.45
9	4.81	89.6	3371.	998.4	1.024	-886.	-559.	1.59
10	4.74	82.7	2479.	998.4	1.024	-132.	-404.	1.57
11	5.23	96.5	1818.	998.4	1.024	-206.	-322.	1.74
12	4.97	82.7	925.	998.4	1.024	-209.	-150.	1.64
Taper 3								
1	15.14	496.	3792.	996.7	0.861	-1123.	-1504.	4.21
2	14.70	462.	2844.	996.7	0.861	-1137.	-1081.	4.09
3	15.16	483.	1932.	996.7	0.861	-1281.	-745.	4.21
4	15.24	483.	984.	996.7	0.861	-1339.	-377.	4.24
5	12.89	510.	3366.	998.4	1.024	-1210.	-1348.	4.26
6	12.72	493.	2832.	998.4	1.024	-1221.	-1110.	4.20
7	12.65	482.	1956.	998.4	1.024	-1271.	-753.	4.18
8	12.45	462.	960.	998.4	1.024	-1276.	-359.	4.11
9	9.72	221.	3780.	996.7	0.861	-383.	-1004.	2.70
10	9.52	207.	2886.	996.7	0.861	-429.	-739.	2.65
11	9.78	207.	936.	996.7	0.861	-559.	-234.	2.72
12	4.83	89.6	3630.	998.4	1.024	-705.	-586.	1.60
13	5.13	96.5	3153.	998.4	1.024	-123.	-541.	1.70
14	5.09	89.6	2028.	998.4	1.024	-177.	-339.	1.68
15	4.78	75.8	1026.	998.4	1.024	-187.	-156.	1.58

Table 5. Test Data from Childs (27) in USCS Units: Experimental results for three smooth tapered seals. Data from taper 2 is compared to PSEAL 1.2 in Figures 13-15.

Run	$Re_z \cdot 10^{-3}$ $\rho V_z H/\mu$	ΔP lb / in^2	ω rpm	ρ lbm / in^3	$\mu \cdot 10^6$ lb • s / in^2	F_r/e lb / in	F_θ/e lb / in	$\dot{Q}$ lbm / s
Taper 1								
1	13.48	147.	3450.	0.0362	0.1806	-20800.	-14300.	11.8
2	13.49	147.	2442.	0.0362	0.1806	-21000.	-10200.	11.8
3	13.34	142.	1200.	0.0362	0.1806	-20400.	-5300.	11.7
4	10.01	80.9	3486.	0.0362	0.1806	-12800.	-10700.	8.75
5	10.26	84.0	2448.	0.0362	0.1806	-12600.	-6740.	8.95
6	10.16	83.0	1302.	0.0365	0.1868	-11800	-4140.	8.95
7	7.60	50.0	3510.	0.0362	0.1806	-8110.	-7770.	6.64
8	8.94	61.9	2292.	0.0362	0.1806	-8850.	-6450.	7.80
9	8.51	54.0	1152.	0.0362	0.1806	-8170.	-3550.	7.43
10	4.86	22.0	3786.	0.0362	0.1868	-3050.	-6170.	4.43
11	5.01	21.0	3450.	0.0362	0.1806	-3420.	-5630.	4.39
12	5.03	20.0	2370.	0.0362	0.1806	-3070.	-3970.	4.41
13	4.84	18.0	1236.	0.0362	0.1806	-2980.	-1990.	4.39
Taper 2								
1	16.35	104.	3750.	0.0361	0.1485	-13000.	-11600.	10.6
2	16.35	104.	2479.	0.0361	0.1485	-12700.	-7770.	10.6
3	16.60	106.	1681.	0.0361	0.1485	-13300.	-5640.	10.8
4	16.45	107.	943.	0.0361	0.1485	-13300.	-4040.	10.7
5	11.10	49.0	4152.	0.0361	0.1485	-5940.	-8450.	7.23
6	10.95	50.0	3390.	0.0361	0.1485	-6280.	-7140.	7.10
7	11.15	48.0	2449.	0.0361	0.1485	-5770.	-5120.	7.23
8	10.20	49.0	1255.	0.0361	0.1485	-6280.	-2890.	7.28
9	5.55	13.0	3371.	0.0361	0.1485	-2340.	-3610.	3.64
10	5.10	12.0	2479.	0.0361	0.1485	-1540.	-2670.	3.64
11	5.40	14.0	1818.	0.0361	0.1485	-1880.	-2210.	3.53
12	5.55	12.0	925.	0.0361	0.1485	-1710.	-1060.	3.64
Taper 3								
1	14.90	71.9	3792.	0.0360	0.1249	-8580.	-10200.	8.97
2	15.10	67.0	2844.	0.0360	0.1249	-8950.	-7040.	9.06
3	14.85	70.0	1932.	0.0360	0.1249	-8820.	-4910.	8.91
4	14.90	70.0	984.	0.0360	0.1249	-9050.	-2840.	8.95
5	12.60	74.0	3366.	0.0361	0.1485	-8430.	-9550.	8.95
6	12.50	71.5	2832.	0.0361	0.1485	-8190.	-5730.	8.71
7	12.70	69.9	1956.	0.0361	0.1485	-9430.	-5520.	9.04
8	12.50	67.0	960.	0.0361	0.1485	-9070.	-2640.	8.95
9	9.85	32.0	3780.	0.0360	0.1249	-3190.	-6620.	5.91
10	9.75	30.0	2886.	0.0360	0.1249	-3580.	-4420.	5.86
11	9.70	30.0	936.	0.0360	0.1249	-4030.	-1510.	5.80
12	4.81	13.0	3630.	0.0361	0.1485	-2760.	-3920.	3.44
13	5.45	14.0	3153.	0.0361	0.1485	-1860.	-3800.	3.90
14	5.35	13.0	2028.	0.0361	0.1485	-1470.	-2330.	3.84
15	5.10	11.0	1026.	0.0361	0.1485	-1540.	-1010.	3.64

Table 6. **Results from PSEAL 1.2 in USCS Units:** Analytical results for three smooth tapered seals. from taper 2 is compared to experimental results in Figures 13-15.

Run	$Re_z \cdot 10^{-3}$ $\rho V_z H/\mu$	ΔP lb / in^2	ω rpm	ρ lbm / in^3	$\mu \cdot 10^6$ lb • s / in^2	F_r/e lb / in	F_θ/e lb / in	$\dot{Q}$ lbm / s
Taper 1								
1	14.33	147.	3450.	0.0362	0.1806	-14270.	-12560.	12.7
2	14.42	147.	2442.	0.0362	0.1806	-14950.	-8878.	12.7
3	14.25	142.	1200.	0.0362	0.1806	-15000.	-4288.	12.6
4	14.39	80.9	3486.	0.0362	0.1806	-7236.	-9401.	9.18
5	10.71	84.0	2448.	0.0362	0.1806	-8216.	-6718.	9.47
6	10.38	83.0	1302.	0.0365	0.1868	-8596.	-3553.	9.49
7	7.97	50.0	3510.	0.0362	0.1806	-3986.	-7410.	7.04
8	9.10	61.9	2292.	0.0362	0.1806	-5942.	-5391.	8.04
9	8.55	54.0	1152.	0.0362	0.1806	-5537.	-2521.	7.55
10	4.78	22.0	3786.	0.0362	0.1868	-1042.	-5136.	4.37
11	4.86	21.0	3450.	0.0362	0.1806	-1127.	-4593.	4.29
12	4.87	20.0	2370.	0.0362	0.1806	-1517.	-3133.	4.31
13	4.73	18.0	1236.	0.0362	0.1806	-1694.	-1552.	4.18
Taper 2								
1	15.28	104.	3750.	0.0361	0.1485	-9914.	-10400.	11.1
2	15.42	104.	2479.	0.0361	0.1485	-10780.	-6821.	11.2
3	15.63	106.	1681.	0.0361	0.1485	-11380.	-4647.	11.4
4	15.75	107.	943.	0.0361	0.1485	-11740.	-2611.	11.5
5	10.11	49.0	4152.	0.0361	0.1485	-3684.	-7948.	7.36
6	10.33	50.0	3390.	0.0361	0.1485	-4282.	-6535.	7.52
7	10.21	48.0	2449.	0.0361	0.1485	-4591.	-4593.	7.44
8	10.45	49.0	1255.	0.0361	0.1485	-5193.	-2353.	7.61
9	4.81	13.0	3371.	0.0361	0.1485	-506.	-3193.	3.50
10	4.74	12.0	2479.	0.0361	0.1485	-755.	-2307.	3.45
11	5.23	14.0	1818.	0.0361	0.1485	-1175.	-1838.	3.84
12	4.97	12.0	925.	0.0361	0.1485	-1196.	-856.	3.62
Taper 3								
1	15.14	71.9	3792.	0.0360	0.1249	-6412.	-8590.	9.28
2	14.70	67.0	2844.	0.0360	0.1249	-6495.	-6172.	9.01
3	15.16	70.0	1932.	0.0360	0.1249	-7312.	-4252.	9.29
4	15.24	70.0	984.	0.0360	0.1249	-7646.	-2151.	9.34
5	12.89	74.0	3366.	0.0361	0.1485	-6907.	-7698.	9.39
6	12.72	71.5	2832.	0.0361	0.1485	-6974.	-6341.	9.26
7	12.65	69.9	1956.	0.0361	0.1485	-7258.	-4298.	9.22
8	12.45	67.0	960.	0.0361	0.1485	-7285.	-2050.	9.07
9	9.72	32.0	3780.	0.0360	0.1249	-2189.	-5734.	5.96
10	9.52	30.0	2886.	0.0360	0.1249	-2450.	-4222.	5.83
11	9.78	30.0	936.	0.0360	0.1249	-3191.	-1338.	5.99
12	4.83	13.0	3630.	0.0361	0.1485	-403.	-3348.	3.52
13	5.13	14.0	3153.	0.0361	0.1485	-704.	-3089.	3.74
14	5.09	13.0	2028.	0.0361	0.1485	-1010.	-1938.	3.71
15	4.78	11.0	1026.	0.0361	0.1485	-1069.	-890.	3.48

Table 7. Seal Geometry from Iwatsubo et al. (46) in SI Units: Seal geometry for smooth and grooved seals with constant radial clearance. Seal 1 data is plotted in Figures 16-18. Seal 2 data is plotted in Figures 19-24.

Seal	L cm	D cm	H inlet cm	H exit cm	NG	Lg cm	Dg cm
Seal 1	3.50	7.00	.0175	.0175	0	0.00	0.00
Seal 2	3.36	7.00	.0175	.0175	10	0.16	0.12
Seal 3	6.56	7.00	.0175	.0175	20	0.16	0.12

Table 8. Seal Geometry from Iwatsubo et al. (46) in USCS Units: Seal geometry for smooth and grooved seals with constant radial clearance. Seal 1 data is plotted in Figures 16-18. Seal 2 data is plotted in Figures 19-24.

Seal	L in	D in	H inlet in	H exit in	NG	Lg in	Dg in
Seal 1	1.38	2.76	.00689	.00689	0	0.00	0.00
Seal 2	1.32	2.76	.00689	.00689	10	0.063	0.047
Seal 3	2.58	2.76	.00689	.00689	20	0.063	0.047

Table 9. **Test Data vs. PSEAL 1.2 Predictions for Seal 1 (SI):** Seal 1 data for Figures 16-18. The seal was tested with water at a pressure drop of 882 kPa (128 psi).

Shaft rpm	F_r kN / m	F_θ kN / m	K kN / m	k kN / m	C kN s/ m	c kN s /m	M kg	$\dot{Q}$ kg / s
Seal 1 data								
500.	-1170.	-116.	1180.	10.0	2.40	0.0	4.90	0.8
1000.	-1110.	-266.	1270.	10.0	2.64	-0.8	6.86	0.8
1500.	-948.	-279.	1180.	98.0	2.40	-0.4	6.86	0.8
2000.	-994.	-370.	1080.	49.0	2.00	0.0	1.96	0.8
2500.	-103.	-569.	1470.	59.0	2.40	0.0	6.37	0.8
3000.	-503.	-656.	1470.	98.0	2.40	0.0	9.80	0.8
3500.	-414.	-821.	1270.	0.0	2.24	0.0	6.37	0.8
Seal 1 Predictions (PSEAL 1.2)								
500.	-1630.	-328.	1631.	15.1	6.56	0.101	2.71	0.73
1000.	-1624.	-656.	1628.	30.0	6.55	0.201	2.27	0.73
1500.	-1614.	-982.	1623.	45.1	6.55	0.300	2.26	0.73
2000.	-1600.	-1307.	1616.	60.5	6.54	0.397	2.26	0.73
2500.	-1583.	-1630.	1608.	76.7	6.54	0.494	2.25	0.72
3000.	-1561.	-1948.	1598.	94.5	6.53	0.588	2.24	0.72
3500.	-1536.	-2263.	1586.	115.	6.53	0.681	2.23	0.72

Table 10. **Test Data vs. PSEAL 1.2 Predictions for Seal 1 (USCS):** Seal 1 data for Figures 16-18. The seal was tested with water at a pressure drop of 882 kPa (128 psi).

Shaft rpm	F_r lb / in	F_θ lb / in	K lb / in	k lb / in	C lb • s / in	c lb • s / in	M lbm	$\dot{Q}$ lbm / s
Seal 1 data								
500.	-6680.	-662.	6740.	57.1	13.7	0.0	10.8	1.8
1000.	-6340.	-1520.	7250.	57.1	15.1	-4.6	15.1	1.8
1500.	-5410.	-1590.	6740.	56.0	13.7	-2.3	15.1	1.8
2000.	-5680.	-2110.	6170.	28.0	11.4	0.0	4.32	1.8
2500.	-588.	-3250.	8390.	33.7	13.7	0.0	14.0	1.8
3000.	-2870.	-3750.	8390.	56.0	13.7	0.0	21.6	1.8
3500.	-2360.	-4690.	7250.	0.0	12.8	0.0	14.0	1.8
Seal 1 Predictions (PSEAL 1.2)								
500.	-9310.	-1874.	9315.	85.8	37.4	0.574	5.01	1.62
1000.	-9275.	-3745.	9297.	172.	37.4	1.15	5.00	1.61
1500.	-9218.	-5610.	9268.	258.	37.4	1.71	4.99	1.61
2000.	-9139.	-7465.	9229.	345.	37.4	2.27	4.98	1.60
2500.	-9038.	-9305.	9181.	438.	37.3	2.82	4.96	1.60
3000.	-8915.	-11130.	9123.	540.	37.3	3.36	4.94	1.59
3500.	-8770.	-12920.	9058.	655.	37.3	3.89	4.93	1.58

Table 11. Test Data vs. PSEAL 1.2 Predictions for Seal 2 (SI): Seal 2 data for Figures 19-24. Seal 2 was tested at a constant running speed of 500 rpm while varying the whirl velocity and inlet preswirl. The test fluid was water at a pressure drop of 882 kPa (128 psi). The radial and tangential forces in this table are for synchronous rotor whirl ($\Omega/\omega = 1$).

Preswirl V_θ / $R\omega$	F_r kN / m	F_θ kN / m	K kN / m	k kN / m	C kN s/ m	c kN s /m	M kg	$\dot{Q}$ kg / s
Seal 2 data								
2.75	-575.	230.	576.	463.	4.42	0.318	6.51	0.63
0.08	-517.	-373.	559.	-137.	4.59	-0.467	6.30	0.63
-2.59	-730.	-680.	736.	-453.	4.38	0.296	7.91	0.63
Seal 2 Predictions (PSEAL 1.2)								
2.75	-1066.	320.6	1064.	679.	6.84	0.128	1.85	0.64
0.08	-1079.	-305.5	1080.	53.4	6.85	0.0675	1.85	0.64
-2.59	-1053.	-927.1	1057.	-569.	6.84	0.00528	1.85	0.63

Table 12. Test Data vs. PSEAL 1.2 Predictions for Seal 2 (USCS): Seal 2 data for Figures 19-24. Seal 2 was tested at a constant running speed of 500 rpm while varying the whirl velocity and inlet preswirl. The test fluid was water at a pressure drop of 882 kPa (128 psi). The radial and tangential forces in this table are for synchronous rotor whirl ($\Omega/\omega = 1$).

Preswirl V_θ / $R\omega$	F_r lb / in	F_θ lb / in	K lb / in	k lb / in	C lb • s / in	c lb • s / in	M lbm	$\dot{Q}$ lbm / s
Seal 2 data								
2.75	-3280.	1310.	3290.	2640.	25.2	1.82	14.4	1.4
0.08	-2950.	-2130.	3190.	-782.	26.2	-2.67	13.9	1.4
-2.59	-4170.	-3880.	4200.	-2590.	25.0	1.69	17.4	1.4
Seal 2 Predictions (PSEAL 1.2)								
2.75	-6087.	1831.	6077.	3880.	39.1	0.733	4.08	1.40
0.08	-6159.	-1745.	6168.	305.0	39.1	0.386	4.08	1.40
-2.59	-6011.	-5294.	6038.	-3250.	39.1	0.0301	4.07	1.40

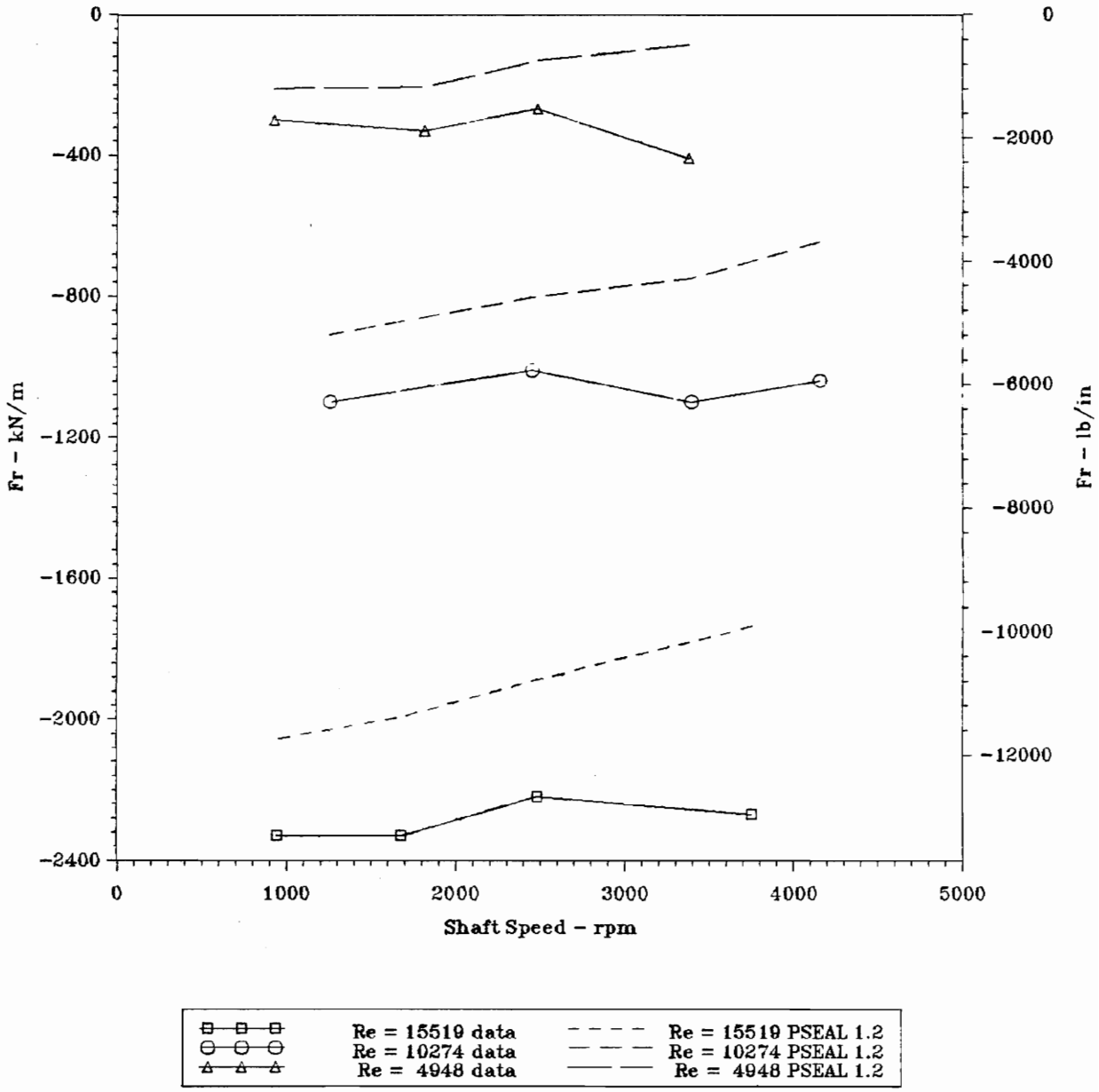

Figure 13. Radial Forces for Taper 2: Test data vs. PSEAL 1.2. Data is from Childs and Dressman, "Convergent-Tapered Annular Seals: Analysis and Testing for Rotordynamic Coefficients", *ASME Journal of Tribology*, Vol. 107, No. 3, July 1985, pp. 307-317.

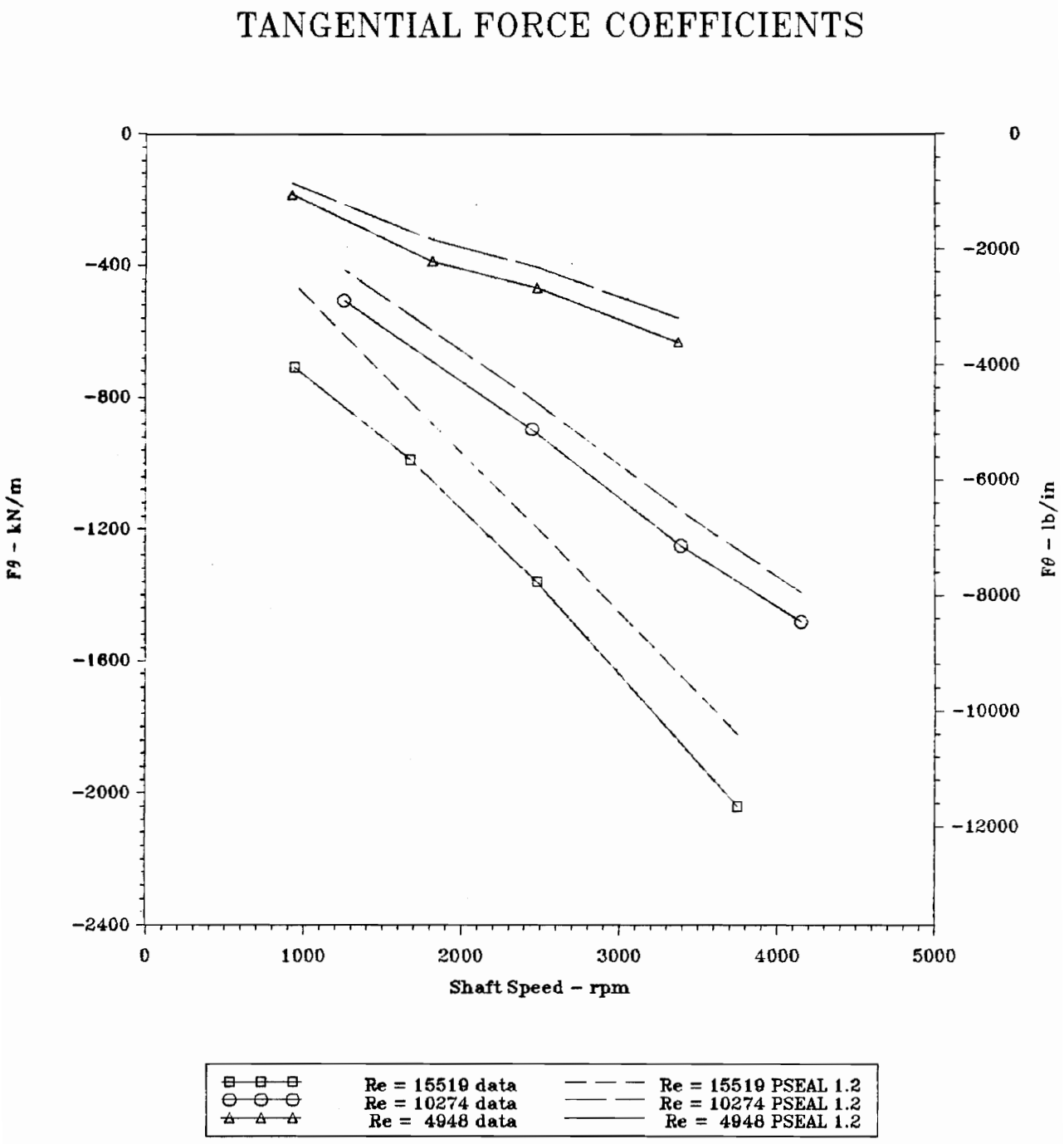

Figure 14. Tangential Forces for Taper 2: Test data vs. PSEAL 1.2. Data is from Childs and Dressman, "Convergent-Tapered Annular Seals: Analysis and Testing for Rotordynamic Coefficients", *ASME Journal of Tribology*, Vol. 107, No. 3, July 1985, pp. 307-317.

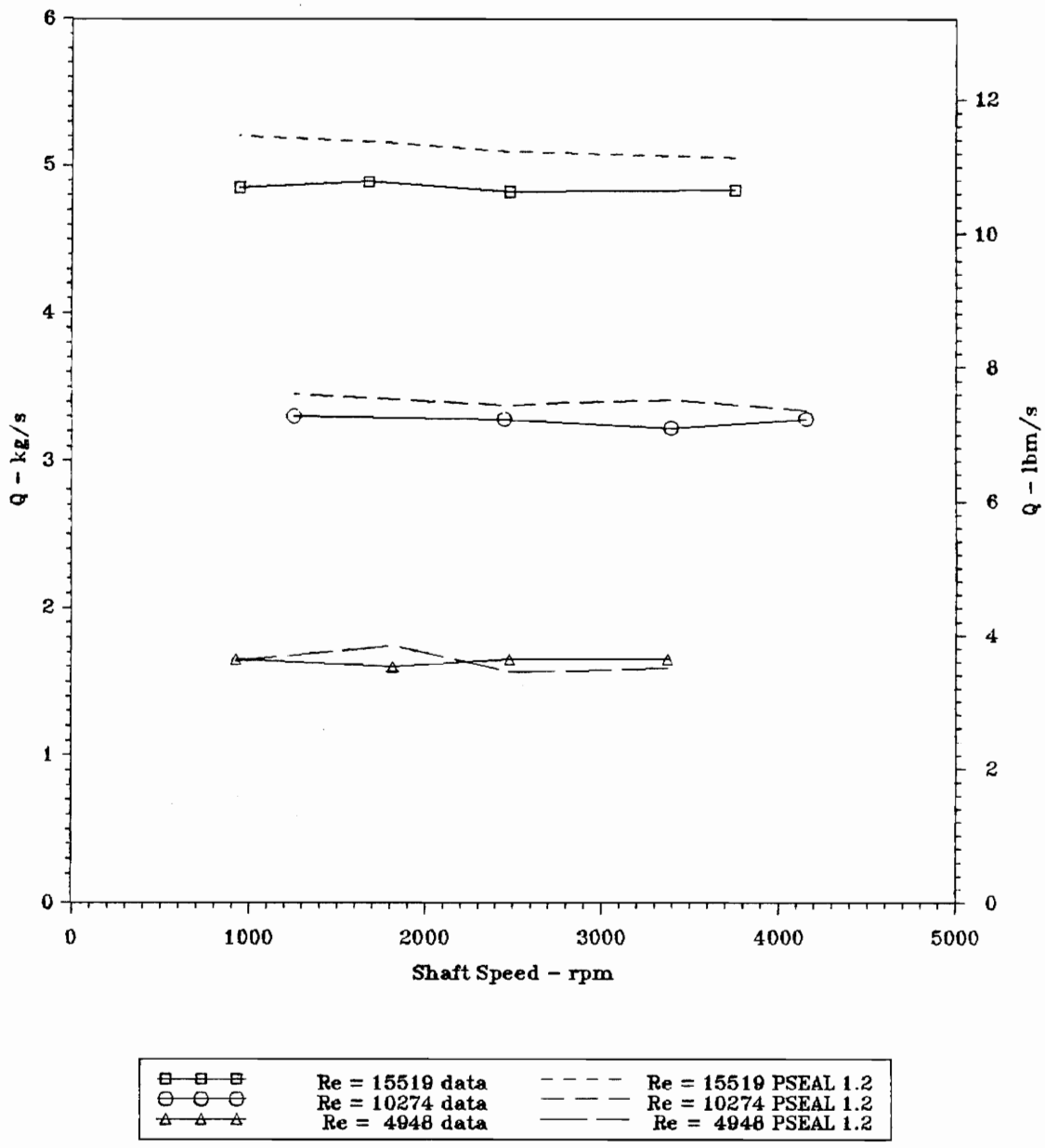

Figure 15. **Seal Leakage for Taper 2:** Test data vs. PSEAL 1.2. Data is from Childs and Dressman, "Convergent-Tapered Annular Seals: Analysis and Testing for Rotordynamic Coefficients", *ASME Journal of Tribology*, Vol. 107, No. 3, July 1985, pp. 307-317.

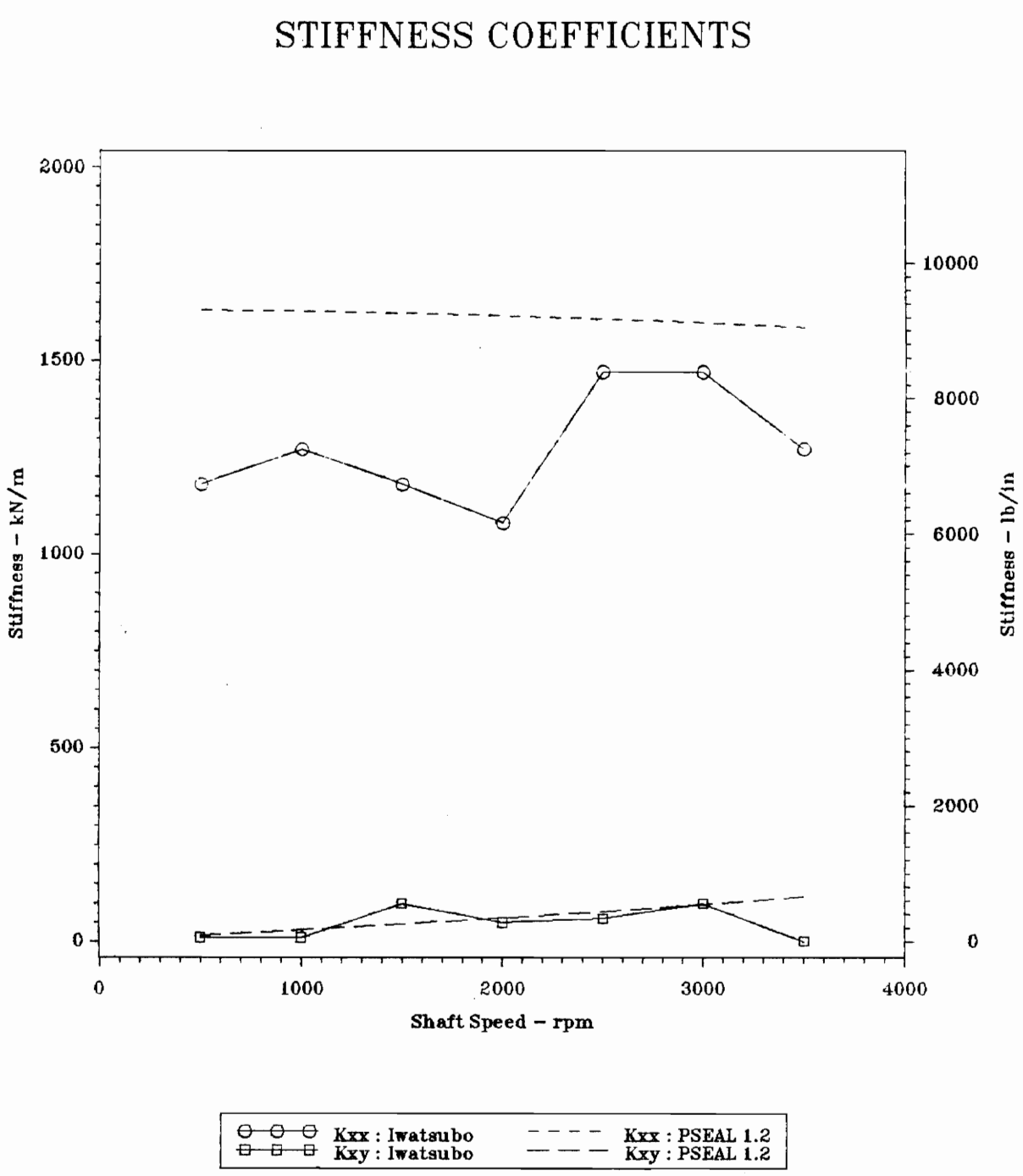

Figure 16. Stiffness Coefficients for Seal 1: Test data vs. PSEAL 1.2. Data is from Iwatsubo et al. (45).

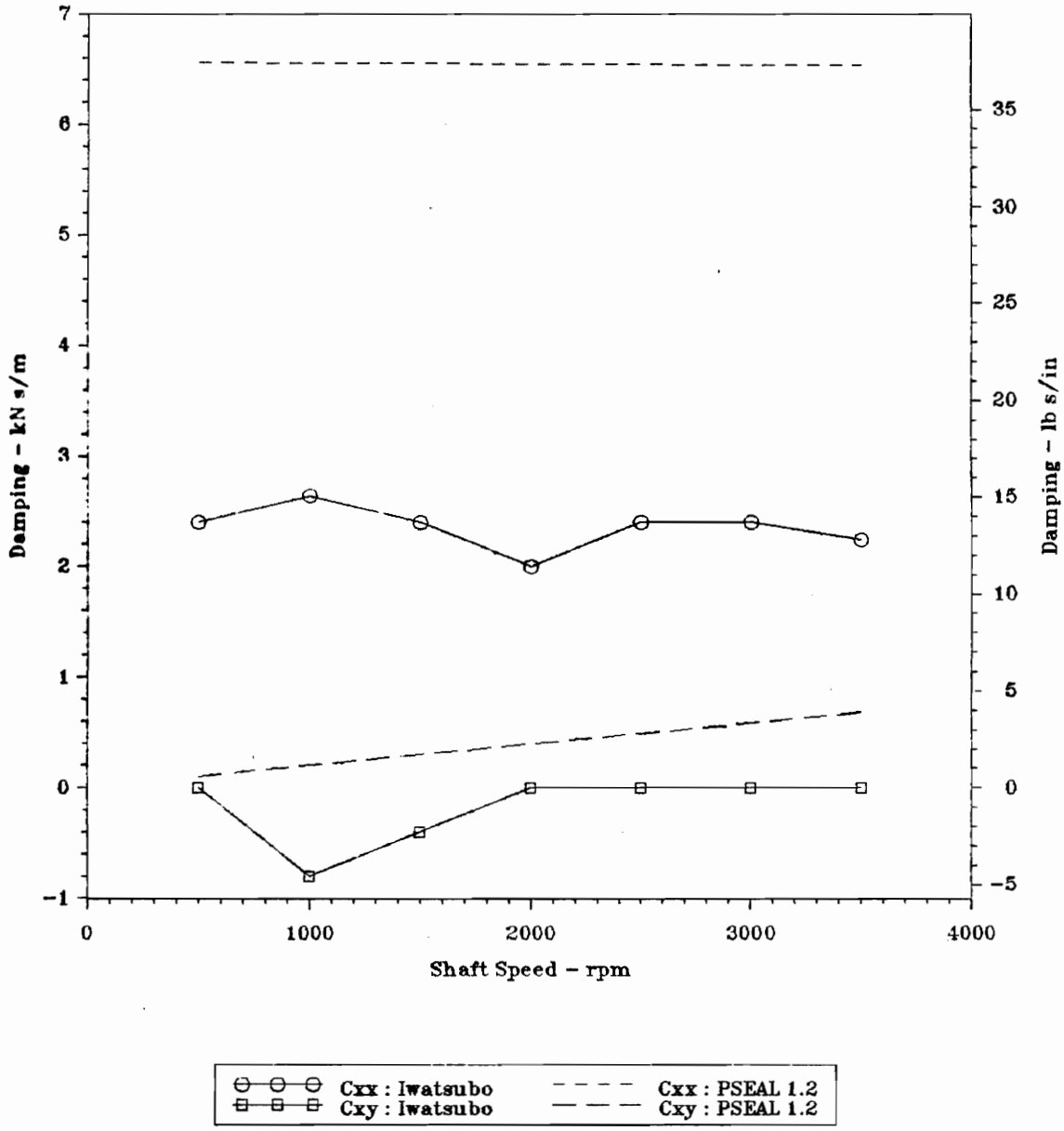

Figure 17. Damping Coefficients for Seal 1: Test data vs. PSEAL 1.2. Data is from Iwatsubo et al. (45).

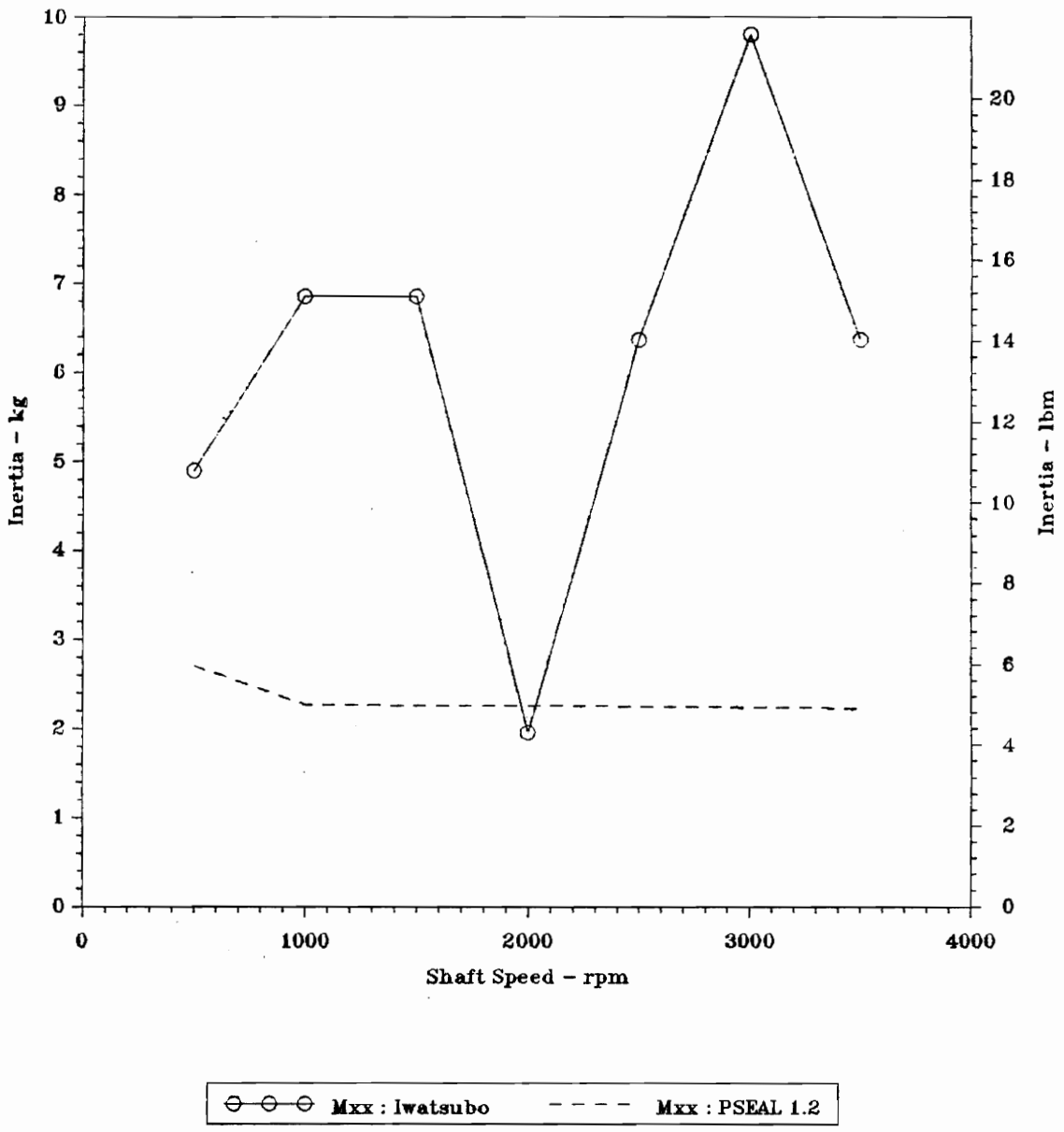

Figure 18. Inertial Coefficients for Seal 1: Test data vs. PSEAL 1.2. Data is from Iwatsubo et al. (45).

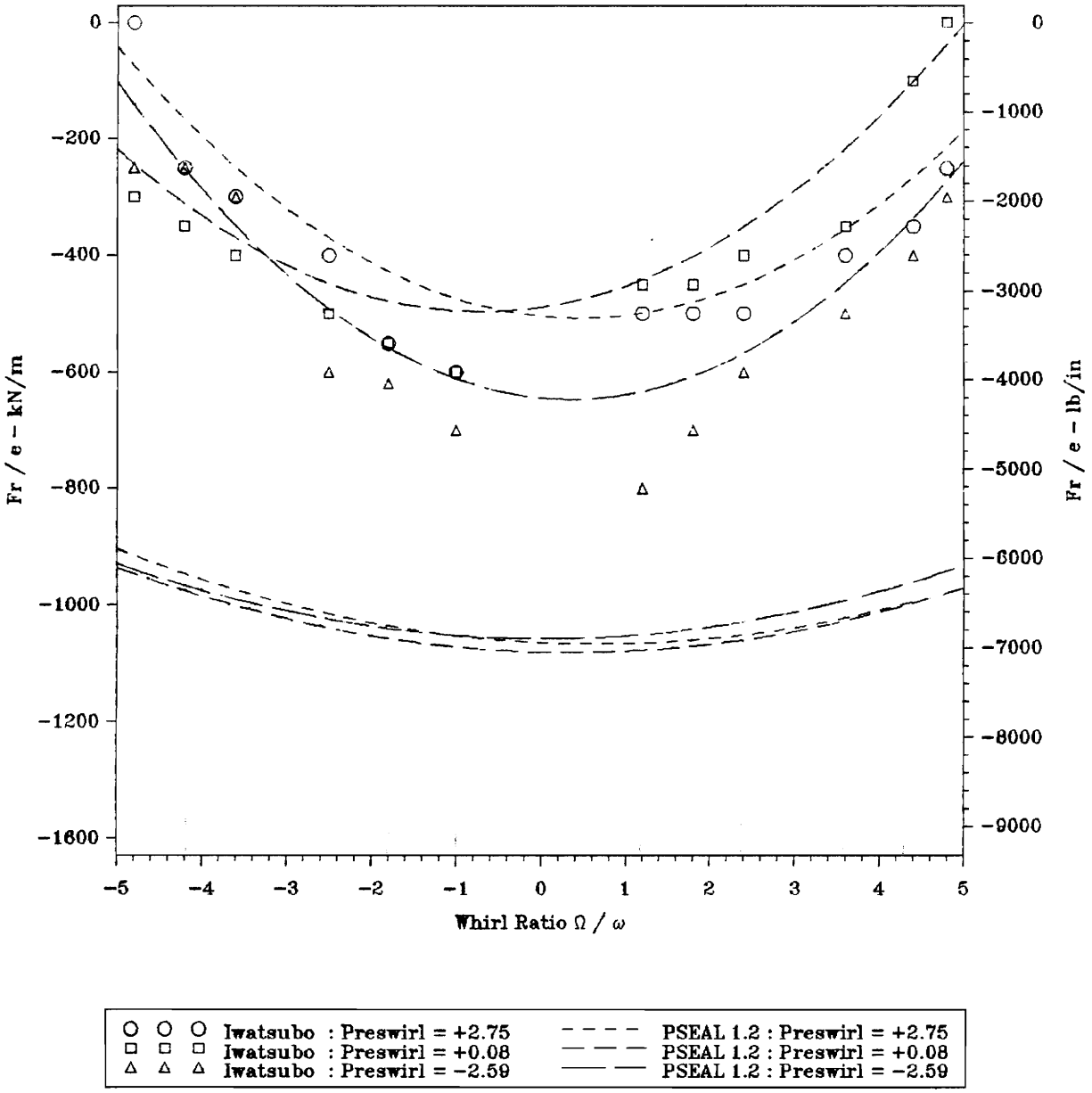

Figure 19. Radial Force vs. Whirl Ratio for Seal 2: Test data vs. PSEAL 1.2. Data is from Iwatsubo and Sheng, "Evaluation of Dynamic Characteristics of Parallel Grooved Seals by Theory and Experiment", *Proceedings of the 3rd International Conference on Rotordynamics - Lyon, France*, Sept. 10-12, 1990, pp. 313-318.

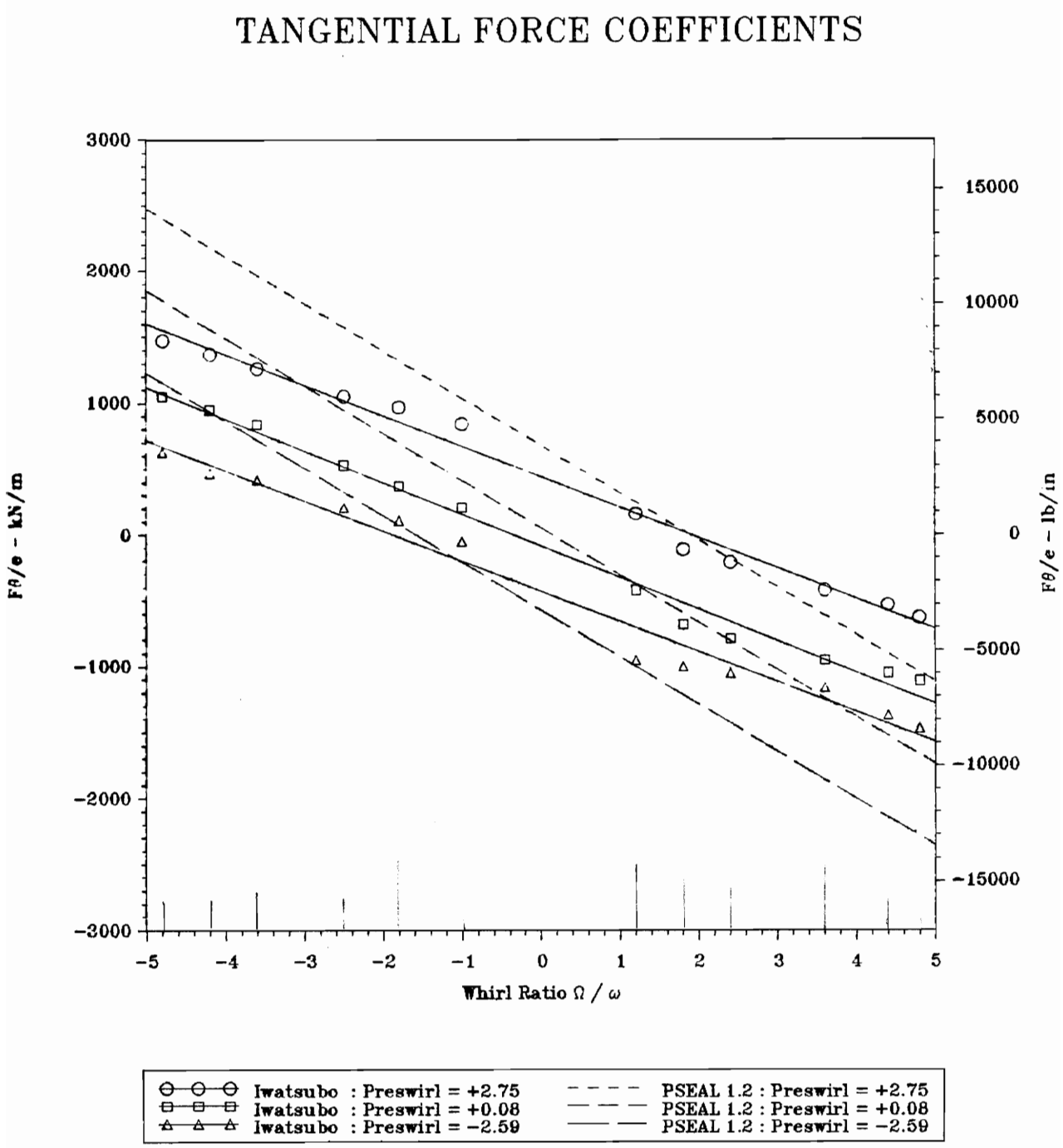

Figure 20. Tangential Force vs. Whirl Ratio for Seal 2: Test data vs. PSEAL 1.2. Data is from Iwatsubo and Sheng, "Evaluation of Dynamic Characteristics of Parallel Grooved Seals by Theory and Experiment", *Proceedings of the 3rd International Conference on Rotordynamics - Lyon, France*, Sept. 10-12, 1990, pp. 313-318.

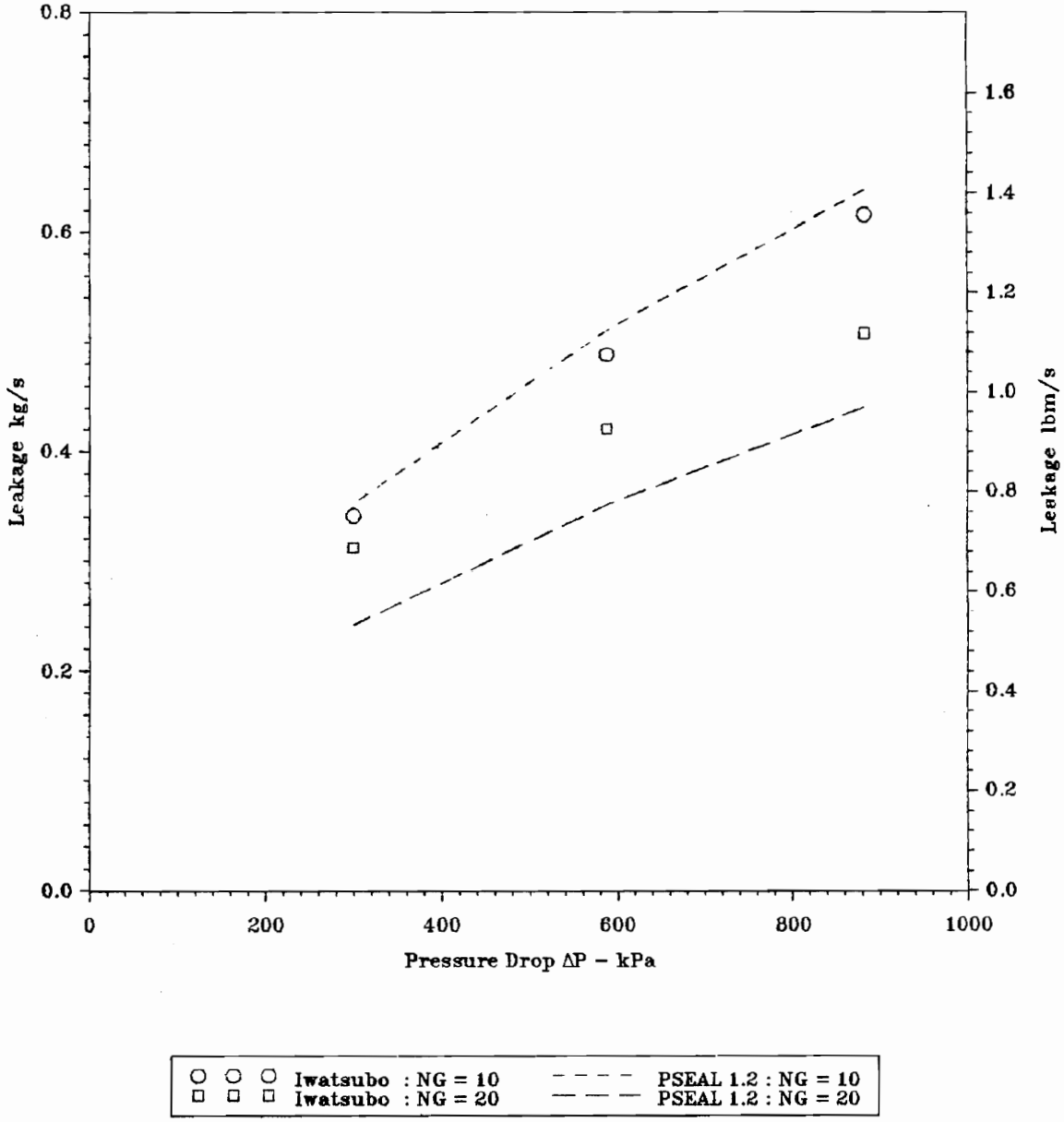

Figure 21. Seal Leakage vs. Pressure Drop for Seals 2 and 3: Test data vs. PSEAL 1.2. Data is from Iwatsubo and Sheng, "Evaluation of Dynamic Characteristics of Parallel Grooved Seals by Theory and Experiment", *Proceedings of the 3rd International Conference on Rotordynamics - Lyon, France*, Sept. 10-12, 1990, pp. 313-318.

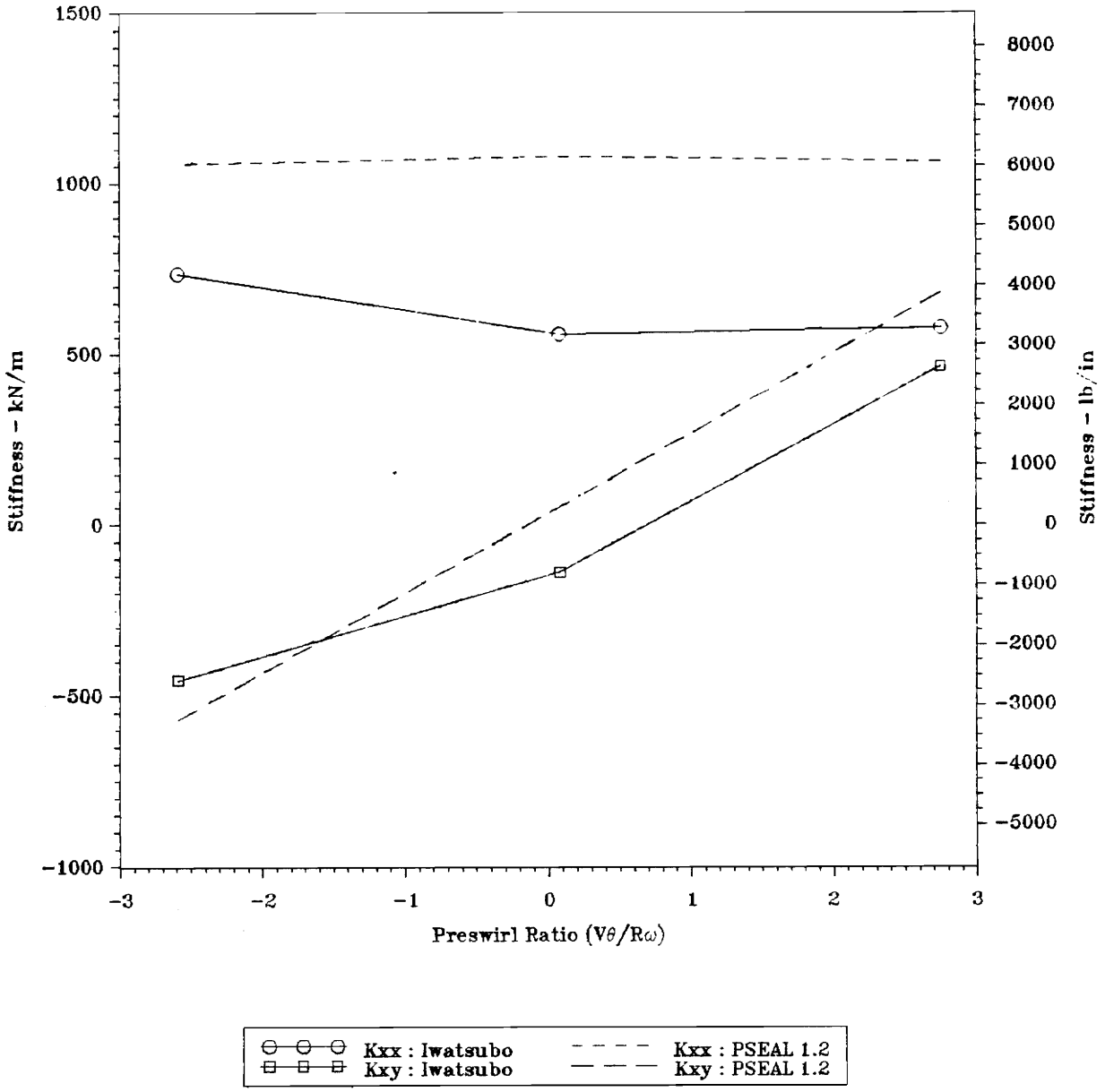

Figure 22. Stiffness Coefficients for Seal 2: Test data vs. PSEAL 1.2. Data is from Iwatsubo and Sheng, "Evaluation of Dynamic Characteristics of Parallel Grooved Seals by Theory and Experiment", *Proceedings of the 3rd International Conference on Rotordynamics - Lyon, France*, Sept. 10-12, 1990, pp. 313-318.

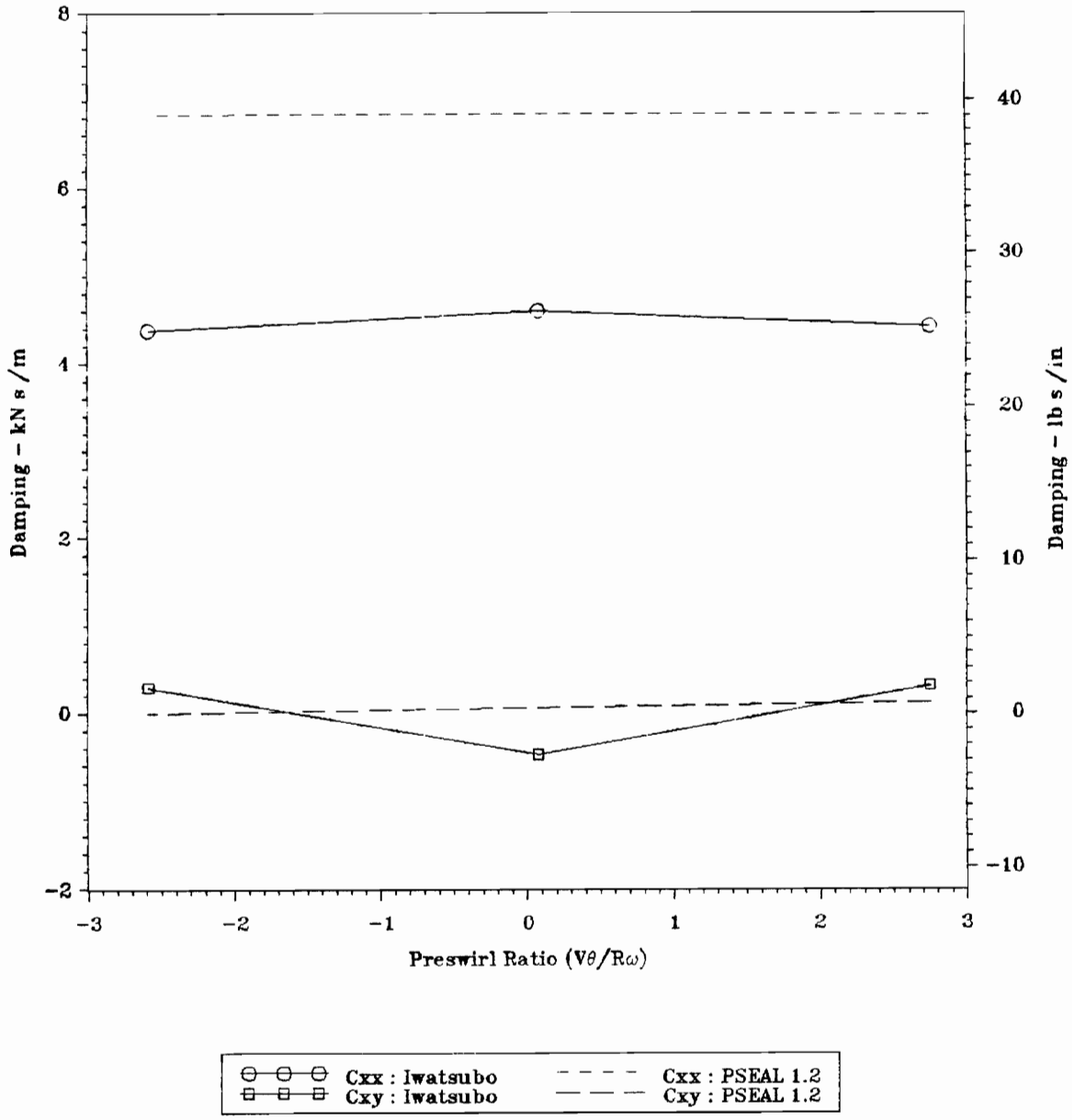

Figure 23. Damping Coefficients for Seal 2: Test data vs. PSEAL 1.2. Data is from Iwatsubo and Sheng, "Evaluation of Dynamic Characteristics of Parallel Grooved Seals by Theory and Experiment", *Proceedings of the 3rd International Conference on Rotordynamics - Lyon, France*, Sept. 10-12, 1990, pp. 313-318.

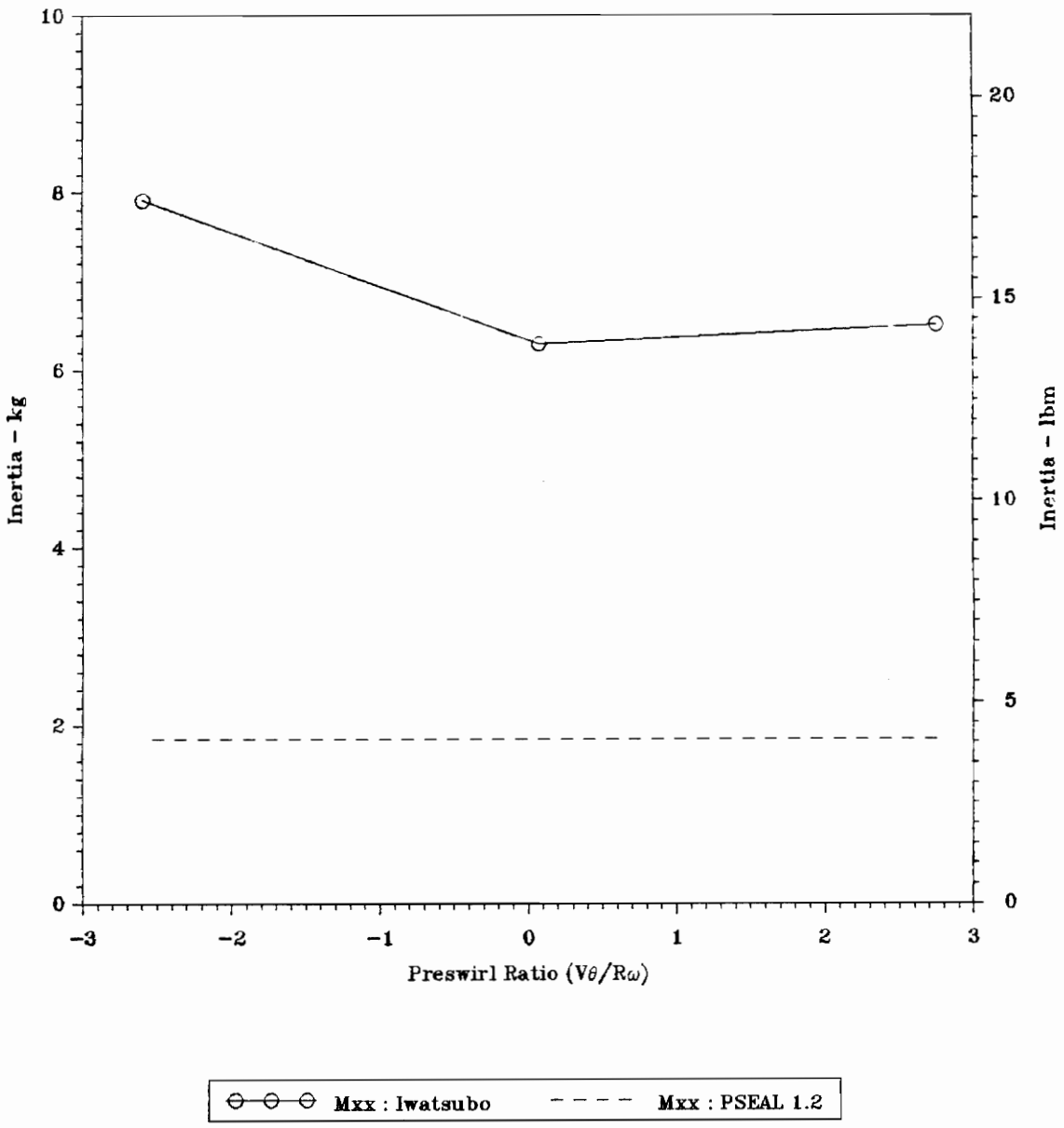

Figure 24. **Inertia Coefficients for Seal 2:** Test data vs. PSEAL 1.2. Data is from Iwatsubo and Sheng, "Evaluation of Dynamic Characteristics of Parallel Grooved Seals by Theory and Experiment", *Proceedings of the 3rd International Conference on Rotordynamics - Lyon, France*, Sept. 10-12, 1990, pp. 313-318.

6. Conclusions and Recommendations

SUMMARY

A PC-based computer program has been developed which will analytically predict the leakage and rotordynamic coefficients for smooth walled or circumferentially grooved annular pressure seals. The analytical model represents an original compilation of information obtained through a search of current technical literature. The governing equations are based on Hirs' bulk-flow theory for turbulent lubrication flims (14). An entrance loss model is developed based on that of Elrod et al. (40). Friction factors in the grooved seal analysis are based on turbulent shear layer theory after Iwatsubo et al. (46). Empirical results from Yamada (12) were used to modify Iwatsubo's method for scaling the pressure losses in the groove. The analytical seal model shows good qualitative agreement when compared to experimental test results. Actual quantitative agreement is unresolved due to a limited data base with high experimental uncertainty. The conclusions and recommendations from this work have been based on on the analytical development as compared to published literature and test results.

CONCLUSIONS

1. The small perturbation assumptions in conjunction with Hirs' friction factor equation provide a sound physical model which predicts physical rotordynamic behavior in seals. The simplifications of the small perturbation technique allow computational efficiency needed for many PC-based applications without significantly compromising the accuracy of the physical model.

2. The analytical model predicts the effect of preswirl on the cross-coupled terms. Increasing preswirl increases cross-coupled stiffness, a destabilizing effect. Negative preswirl is shown to drive the cross-coupled stiffness to negative values which is a stabilizing influence in seals.

3. The analytical model predicts the effect of adding circumferential grooves to the seal. Adding grooves increases the effective friction factor which decreases leakage and enhances stability.

4. The analytical model shows moderately good agreement with published test results. There is a tendency to overpredict direct stiffness and underpredict direct inertia, however, the uncertainty in experimental results makes it difficult to reach a firm conclusion on the quantitative accuracy of the current analytical model.

RECOMMENDATIONS

1. A broader base of test data is needed to help quantify the model. Development of a seal test facility at Virginia Tech would significantly enhance future research efforts in this field.

2. The recent development of high speed personal computers and workstations has made possible the development of a 3-D finite element code specifically tailored to model seal dynamics. Such a code could model virtually any seal geometry including eccentric seals with non-circular orbits. This is recommended for future analytical research.

References

1. Vance, John M., Rotordynamics of Turbomachinery , John Wiley & Sons, 1988, pp. 202-260.

2. Adams, M. L., and Padovan, J., "Insights Into Linearized Rotor Dynamics", *Journal of Sound and Vibration*, Vol. 76, No. 1, 1981, pp. 129-142.

3. Adams, M. L., "A Note On Rotor-Bearing Stability", *Journal of Sound and Vibration*, Vol. 86, No. 3, 1983, pp. 435-438.

4. Adams, M. L., "Insights Into Linearized Rotor Dynamics, Part 2", *Journal of Sound and Vibration*, Vol. 112, No. 1, 1987, pp. 97-110.

5. Allaire, P. E., Gunter, E. J., Lee, C. P., and Barrett, L. E., "The Dynamic Analysis of the Space Shuttle Main Engine High Pressure Fuel Turbopump Final Report, Part II, Load Capacity and Hybrid Coefficients for Turbulent Interstage Seals", University of Virginia Report UVA/528140/ME76/103, Sept. 1976.

6. Childs, D. W., "The Space Shuttle Main Engine High-Pressure Fuel Turbopump Rotordynamic Instability Problem", *ASME Journal of Engineering for Power*, Vol. 100, No. 1, Jan. 1978, pp. 48-57.

7. Barrett, L. E., "Turbulent Flow Annular Pump Seals: A Literature Review", *Shock and Vibration Digest*, Vol. 16, No. 2, Feb. 1984, pp. 3-13.

8. Flack, R. D., and Allaire, P. E., "Lateral Forces on Pump Impellers: A Literature Review", *Shock And Vibration Digest*, Vol. 16, No. 1, Jan. 1984, pp. 5-14.

9. Ehric, F., and Childs, D., "Self-Excited Vibration in High-Performance Turbomachinery", *Mechanical Engineering*, Vol. 106, No. 5, May 1984, pp. 66-79.

10. Lomakin, A. A., "Calculation of Critical Speed and Securing of Dynamic Stability of Hydraulic High-Pressure Pumps With Reference to the Forces Arising in the Gap Seals", *Energomashinostroenie*, Vol. 4, No. 1, 1958, p. 1158.

11. Yamada, Y., "Resistance of a Flow Through an Annulus with an Inner Rotating Cylinder", *Bulletin of Japan Society of Mechanical Engineers*, Vol. 5, No. 18, May 1962, pp. 302-310.

12. Yamada, Y., "On the Pressure Loss of Flow Between Rotating Co-Axial Cylinders with Rectangular Grooves", *Bulletin of Japan Society of Mechanical Engineers*, Vol. 5, No. 20, 1962, pp. 642-651.

13. Yamada, Y., Nakabayashi, K., and Maeda, K., "Pressure Drop Measurements of the Flow through Eccentric Cylinders with Rotating Inner Cylinders", *Bulletin of Japan Society of Mechanical Engineers*, Vol. 12, No. 53, Dec. 1969, pp. 1032-1040.

14. Hirs, G. G., "A Bulk-Flow Theory for Turbulence in Lubricant Films", *ASME Journal of Lubrication Technology*, Vol. 95, No. 2, April 1973, pp. 137-146.

15. Black, H. F., "Effects of Hydraulic Forces in Annular Pressure Seals on the Vibrations of Centrifugal Pump Rotors", *Journal of Mechanical Engineering Science*, Vol. 11, No. 2, 1969, pp. 206-213.

16. Black, H. F., and Jenssen, D. N., "Dynamic Hybrid Bearing Characteristics of Annular Controlled Leakage Seals", *Proceedings of the Institution of Mechanical Engineers*, Vol. 184, Pt. 3N, 1969-70, pp. 92-100.

17. Black, H. F., Allaire, P. E., and Barrett, L. E., "Inlet Flow Swirl in Short Turbulent Annular Seal Dynamics", *9th International Conference on Fluid Sealing*, Paper D4, April 1-3, 1981, pp. 141-152.

18. Black, H. F., "Empirical Treatment of Hydrodynamic Journal Bearing Performance in the Superlaminar Regime", *Journal of Mechanical Engineering Science*, Vol. 12, No. 2, 1970, pp. 116-122.

19. Black, H. F., "On Journal Bearings With High Axial Flows In The Turbulent Regime", *Journal of Mechanical Engineering Science*, Vol. 12, No. 4, 1970, pp. 301-303.

20. Black, H. F., and Cochrane, E. A., "Leakage and Hybrid Bearing Properties of Serrated Seals in Centrifugal Pumps", *6th International Conference on Fluid Sealing*, Paper G5, Feb 1973, pp. G5-61-70.

21. Allaire, P. E., Lee, C. C., and Gunter, E. J., "Dynamics of Short Eccentric Plain Seals with High Axial Reynolds Number", *Journal of Spacecraft and Rockets*, Vol. 15, No. 6, 1978, pp. 341-347.

22. Allaire, P. E., Lee, C. P., and Farris, R. C., "Turbulent Flow in Seals: Load Capacity and Dynamic Coefficients - A Manual for Computer Program SEAL1", University of Virginia Report UVA/464761/ME76/139, Dec. 1976.

23. Childs, D. W., Nelson, C., Noyes, T., and Dressman, J. B., "A High Reynolds Number Seal Test Facility: Facility Description and Preliminary Test Data", NASA Conference Publication 2250, *Proceedings from a Workshop on Rotordynamic Instability Problems in High Performance Turbomachinery*, held at Texas A & M University, May 10-12, 1982, pp. 172-186.

24. Childs, D. W., and Dressman, J. B., "Testing of Turbulent Seals for Rotordynamic Coefficients", NASA Conference Publication 2250, *Proceedings from a Workshop on Rotordynamic Instability Problems in High Performance Turbomachinery*, held at Texas A & M University, May 10-12, 1982, pp. 157-171.

25. Childs, D. W., "Dynamic Analysis of Turbulent Annular Seals Based on Hirs' Lubrication Equation", *ASME Journal of Lubrication Technology*, Vol. 105, No. 3, July 1983, pp. 429-436.

26. Childs. D. W., "Finite-Length Solutions for Rotordynamic Coefficients of Turbulent Annular Seals", *ASME Journal of Lubrication Technology* , Vol. 105, No. 3, July 1983, pp. 437-444.

27. Childs, D. W., and Dressman, J. B., "Convergent-Tapered Annular Seals: Analysis and Testing for Rotordynamic Coefficients", *ASME Journal of Tribology*, Vol. 107, No. 3, July 1985, pp. 307-317.

28. Kilgore, J. J., and Childs, D. W., "Rotordynamic Characteristics and Leakage Flow of Circumferentially Grooved Liquid Seals", *ASME Journal of Fluids Engineering*, Vol. 112, No. 3, Sep. 1990, pp. 250-256.

29. Nordmann, R., Dietzen, F. J., Janson, W., Frei, A., and Florjancic, S., "Rotordynamic Coefficients and Leakage Flow of Parallel Grooved Seals and Smooth Seals", NASA Conference Publication 2443, *Proceedings from a Workshop on Rotordynamic Instability Problems in High Performance Turbomachinery*, held at Texas A & M University, 1986, pp. 129-154.

30. Childs, D. W., and Kim, Chang-Ho, "Analysis and Testing for Rotordynamic Coefficients of Turbulent Annular Seals With Different, Directionally Homogeneous Surface Roughness Treatment for Rotor and Stator Elements", *ASME Journal of Tribology*, Vol. 107, No. 3, July 1985, pp. 296-306.

31. Childs, D. W., and Kim, Chang-Ho, "Test Results for Round-Hole-Pattern Damper Seals: Optimum Configurations and Dimensions for Maximum Net Damping", *ASME Journal of Tribology*, Vol. 108, No. 4, Oct. 1986, pp. 605-611.

32. Childs, D. W., Nolan, S. A., and Kilgore, J. J., "Additional Test Results For Round-Hole-Pattern Damper Seals: Leakage, Friction Factors, and Rotordynamic Force Coefficients", *ASME Journal of Tribology*, Vol. 112, No. 2, April 1990, pp. 365-371.

33. Childs, D. W., Nolan, S. A., and Kilgore, J. J., "Test Results for Turbulent Annular Seals, Using Smooth Rotors and Helically Grooved Stators", *ASME Journal of Tribology*, Vol. 112, No. 2, April 1990, pp. 254-258.

34. Kim, Chang-Ho, and Childs, D. W., "Analysis for Rotordynamic Coefficients of Helically-Grooved Turbulent Annular Seals", *ASME Journal of Tribology*, Vol. 109, No. 1, Jan. 1987, pp. 136-143.

35. Nelson, C. C., and Nguyen, D. T., 1987, "Comparison of Hirs' Equation With Moody's Equation for Determining Rotordynamic Coefficients of Annular Pressure Seals", *ASME Journal of Tribology*, Vol. 109, No. 1, Jan. 1987, pp. 144-148.

36. Nelson, C. C., and Nguyen, D. T., "Analysis of Eccentric Annular Incompressible Seals: Part 1 - A New Solution Using Fast Fourier Transforms for Determining Hydrodynamic Force", *ASME Journal of Tribology*, Vol. 110, No. 2, April 1988, pp. 354-360.

37. Nelson, C. C., and Nguyen, D. T., "Analysis of Eccentric Annular Incompressible Seals: Part 2 - Effects of Eccentricity on Rotordynamic Coefficients", *ASME Journal of Tribology*, Vol. 110, No. 2, April 1988, pp. 361-366.

38. Scharrer, J. K., and Nelson, C. C., "Rotordynamic Coefficients for Partially Tapered Annular Seals: Part 1 - Incompressible Flow", *ASME Journal of Tribology*, Vol. 113, No. 1, Jan. 1991, pp. 48-52.

39. Nelson, C. C., "Rotordynamic Coefficients for Compressible Flow in Tapered Annular Seals", *ASME Journal of Tribology*, Vol. 107, No. 3, July 1985, pp. 318-325.

40. Elrod, D., Nelson, C., and Childs, D., "An Entrance Region Friction Factor Model Applied to Annular Seal Analysis: Theory Versus Experiment for Smooth and Honeycomb Seals", *ASME Journal of Tribology*, Vol. 111, No. 2, April 1989, pp. 337-343.

41. Elrod, D. A., Childs, D. W., and Nelson, C. C., "An Annular Gas Seal Analysis Using Empirical Entrance and Exit Region Friction Factors", *ASME Journal of Tribology*, Vol. 112, No. 2, April 1990, pp. 196-204.

42. Dietzen, F. J., and Nordmann, R., "Calculation of Rotordynamic Coefficients of Seals by Finite Difference Techniques", *ASME Journal of Tribology*, Vol. 109, No. 3, July 1987, pp. 388-394.

43. Nordmann, R., Dietzen, F. J., and Weiser, H. P., "Calculation of Rotordynamic Coefficients and Leakage for Annular Gas Seals by Means of Finite Difference Techniques", *ASME Journal of Tribology*, Vol. 111, No. 3, July 1989, pp. 545-552.

44. Iwatsubo, T., Yang, B., and Ibaraki, R., "Static and Dynamic Characteristics of Parallel-Grooved Seals", NASA Conference Publication 2443, *Proceedings from a Workshop on Rotordynamic Instability Problems in High-Performance Turbomachinery*, held at Texas A & M University, 1986, pp. 99-128.

45. Iwatsubo, T., Sheng, B. C., and Matsumoto, T., "An Experimental Study on the Static and Dynamic Characteristics of Pump Annular Seals", NASA Conference Publication 3026, *Proceedings from a Workshop on Rotordynamic Instability Problems in High-Performance Turbomachinery*, held at Texas A & M University, 1988, pp. 229-252.

46. Iwatsubo, T., and Sheng, B. C., "Evaluation of Dynamic Characteristics of Parallel Grooved Seals by Theory and Experiment", *Proceedings of the 3rd International Conference on Rotordynamics - Lyon, France*, Sept. 10-12, 1990, pp. 313-318.

47. Barbin, A. R., and Jones, J. B., "Turbulent Flow in the Inlet Region of a Smooth Pipe", *ASME Journal of Basic Engineering*, Vol. 85, No. 1, March 1963, pp. 29-34.

48. Klein, A., "Review: Turbulent Developing Pipe Flow", *ASME Journal of Fluids Engineering*, Vol. 103, No. 2, June 1981, pp. 243-249.

49. Shapiro, A. H., and Smith, R. D., "Friction Coefficients in the Inlet Length of Smooth, Round Tubes", NACA Technical Note No. 1785.

50. Wang, J. S., and Tullis, J. P., "Turbulent Flow in the Entry Region of a Rough Pipe", *ASME Journal of Fluids Engineering*, Vol. 96, No. 1, March 1974, pp. 62-68.

51. Deissler, R. G., "Analysis of Turbulent Heat Transfer and Flow in the Entrance Regions of Smooth Passages", NACA Technical Note No. 3016.

52. Bejan, Adrian, Convection Heat Transfer , John Wiley & Sons, 1984, pp. 282-295.

Appendix A. Derivation of the Dynamic Force Equations for a Circular Orbit

With reference to Figure 2 on page 5, the equations of motion for a nominally centered seal with a circular whirl orbit are given by:

$$-\begin{Bmatrix} F_x \\ F_y \end{Bmatrix} = \begin{bmatrix} K & k \\ -k & K \end{bmatrix} \begin{Bmatrix} x \\ y \end{Bmatrix} + \begin{bmatrix} C & c \\ -c & C \end{bmatrix} \begin{Bmatrix} \dot{x} \\ \dot{y} \end{Bmatrix} + \begin{bmatrix} M & m \\ -m & M \end{bmatrix} \begin{Bmatrix} \ddot{x} \\ \ddot{y} \end{Bmatrix}$$

This matrix equation is expanded to yield the x- and y- components:

$$-F_x = Kx + ky + C\dot{x} + c\dot{y} + M\ddot{x} + m\ddot{y}$$
$$-F_y = -kx + Ky - c\dot{x} + C\dot{y} - m\ddot{x} + M\ddot{y}$$

The x- and y- coordinates for a circular rotor orbit of whirl velocity Ω and amplitude e are given by:

$$x = e\ \cos \Omega t \qquad y = e\ \sin \Omega t$$
$$\dot{x} = -\,e\,\Omega \sin \Omega t \qquad \dot{y} = e\,\Omega \cos \Omega t$$
$$\ddot{x} = -e\,\Omega^2 \cos \Omega t \qquad \ddot{y} = -e\,\Omega^2 \sin \Omega t$$

Making these substitutions into the rotordynamic equation above we have:

$$\frac{-F_x}{e} = K\cos\Omega t + k\sin\Omega t - C\Omega\sin\Omega t + c\Omega\cos\Omega t - M\Omega^2\cos\Omega t - m\Omega^2\sin\Omega t$$
$$\frac{-F_y}{e} = -k\cos\Omega t + K\sin\Omega t + c\Omega\sin\Omega t + C\Omega\cos\Omega t + m\Omega^2\cos\Omega t - M\Omega^2\sin\Omega t$$

Collecting sine and cosine terms we have:

$$\frac{-F_x}{e} = (K + c\Omega - M\Omega^2)\cos\Omega + (k - C\Omega - m\Omega^2)\sin\Omega t$$
$$\frac{-F_y}{e} = (-k + C\Omega + m\Omega^2)\cos\Omega + (K + c\Omega - M\Omega^2)\sin\Omega t$$

The x- and y- components can be translated into radial and tangential force components where the radial direction coincides with the whirl angle, Ωt, by the following equations:

$$F_x = F_r\cos\Omega t - F_\theta\sin\Omega t$$
$$F_y = F_\theta\cos\Omega t + F_r\sin\Omega t$$

By comparing these equations to the rotordynamic equations above, the following relationships can be easily deduced:

$$\frac{F_r}{e} = -K - c\Omega + M\Omega^2$$
$$\frac{F_\theta}{e} = k - C\Omega - m\Omega^2$$

These equations show that the forces developed on the rotor are proportional to the square of the whirl frequency. Thus by analyzing different whirl frequencies and fitting a parabola through the plot of force vs. Ω, the rotordynamic coefficients can be determined.

Appendix B. Governing Equations

Continuity Equation

$$\frac{\partial H}{\partial t} + \frac{\partial}{\partial z}(V_z H) + \frac{1}{R}\frac{\partial}{\partial \theta}(V_\theta H) = 0$$

Axial Momentum Equation

$$H\left(\frac{\partial V_z}{\partial t} + \frac{V_\theta}{R}\frac{\partial V_z}{\partial \theta} + V_z\frac{\partial V_z}{\partial z}\right) = -\frac{1}{\rho}\left(H\frac{\partial P}{\partial z} + \tau_{sz} + \tau_{rz}\right)$$

Circumferential Momentum Equation

$$H\left(\frac{\partial V_\theta}{\partial t} + \frac{V_\theta}{R}\frac{\partial V_\theta}{\partial \theta} + V_z\frac{\partial V_\theta}{\partial z}\right) = -\frac{1}{\rho}\left(\frac{H}{R}\frac{\partial P}{\partial \theta} + \tau_{s\theta} + \tau_{r\theta}\right)$$

Zeroth Order Continuity Equation

$$\frac{\partial}{\partial z}(V_{z0}H_0) = 0$$

Zeroth Order Axial Momentum Equation

$$H_0\left(V_{z0}\frac{\partial V_{z0}}{\partial z}\right) = -\frac{1}{\rho}\left(H_0\frac{\partial P_0}{\partial z} + \tau_{sz0} + \tau_{rz0}\right)$$

Zeroth Order Circumferential Momentum Equation

$$H_0 V_{z0}\frac{\partial V_{\theta 0}}{\partial z} = -\frac{1}{\rho}(\tau_{s\theta 0} + \tau_{r\theta 0})$$

First Order Continuity Equation

$$\frac{\partial H_1}{\partial t} + \frac{\partial}{\partial z}(V_{z1}H_0 + V_{z0}H_1) + \frac{1}{R}\frac{\partial}{\partial \theta}(V_{\theta 1}H_0 + V_{\theta 0}H_1) = 0$$

First Order Axial Momentum Equation

$$H_0\left(\frac{\partial V_{z1}}{\partial t} + \frac{V_{\theta 0}}{R}\frac{\partial V_{z1}}{\partial \theta} + V_{z0}\frac{\partial V_{z1}}{\partial z} + V_{z1}\frac{\partial V_{z0}}{\partial z}\right) + H_1 V_{z0}\frac{\partial V_{z0}}{\partial z} = \frac{-1}{\rho}\left(H_0\frac{\partial P_1}{\partial z} + H_1\frac{\partial P_0}{\partial z} + \tau_{sz1} + \tau_{rz1}\right)$$

First Order Circumferential Momentum Equation

$$H_0\left(\frac{\partial V_{\theta 1}}{\partial t} + \frac{V_{\theta 0}}{R}\frac{\partial V_{\theta 1}}{\partial \theta} + V_{z0}\frac{\partial V_{\theta 1}}{\partial z} + V_{z1}\frac{\partial V_{\theta 0}}{\partial z}\right) + H_1 V_{z0}\frac{\partial V_{\theta 0}}{\partial z} = -\frac{1}{\rho}\left(\frac{H_0}{R}\frac{\partial P_1}{\partial \theta} + \tau_{s\theta 1} + \tau_{r\theta 1}\right)$$

Appendix C. First Order Variables

Derivation of the Clearance Equation for a Circular Whirl Orbit

With reference to Figure 6 on page 21, we seek to derive an expression for the clearance, H, as a function of the angular coordinate, ϕ, where ϕ is measured relative to the line of centers. From an inertial frame of reference, θ, we have the relationship that $\phi = \theta - \Omega t$ where Ω is the whirl angular velocity in rad/s. Note that the nominal (zeroth order) clearance, H_0, is related to the stator radius, R_s, and the rotor radius, R_r, by the following equation.

$$H_0 = R_s - R_r$$

From the law of cosines, we can then deduce the following relationship.

$$R_r^2 = (R_s - H)^2 + e^2 - 2(R_s - H)e\cos\phi$$

Introducing the nominal clearance on the left hand side we have:

$$(R_s - H_0)^2 = (R_s - H)^2 + e^2 - 2(R_s - H)e\cos\phi$$
$$R_s^2 - 2R_sH_0 + H_0^2 = R_s^2 - 2R_sH + H^2 + e^2 - 2(R_se - He)\cos\phi$$

Note that $e,H \ll R_s,R_r$, therefore products of the orbit radius, e, and the clearances, H_0, H, can be neglected without introducing appreciable errors. This reduces the clearance equation to the following relationship.

$$H = H_0 - e\cos\phi$$

The first order solution assumes that for small perturbations about the centered position, the velocity and pressure variables will experience small perturbations from the zeroth order solution. Hence the primitive variables in the governing equations are replaced by the following zeroth and first order variables.

$$\begin{aligned} H &= H_0 + H_1 \\ P &= P_0 + P_1 \\ V_z &= V_{z0} + V_{z1} \\ V_\theta &= V_{\theta 0} + V_{\theta 1} \end{aligned}$$

From the clearance equation derived above we see that $H_1 = -e\cos\phi$. Assuming that the clearance perturbations drive the first order solution, i.e., the pressure and velocity changes are caused by changes in clearance, it is reasonable to assume that the first order perturbation variables will have the same form as the first order clearance. In general this means the first order variables will be composed of sine and cosine functions of the following form.

$$\begin{aligned} P_1 &= P_{1c}\cos\phi + P_{1s}\sin\phi \\ V_{z1} &= V_{z1c}\cos\phi + V_{z1s}\sin\phi \\ V_{\theta 1} &= V_{\theta 1c}\cos\phi + V_{\theta 1s}\sin\phi \end{aligned}$$

Thus, we have assumed a functional relationship for the first order variables in t and θ based on the first order clearance. The unknown coefficients will be constant for a given axial position but will in general vary along the length of the seal. It is the axial variation that remains to be determined. Based on the assumed form of the first order variables. we can now derive expressions for the derivatives in the governing equations as follows.

First Order Clearance and Derivatives

$$H_1 = -e\cos(\theta - \Omega t)$$
$$\frac{\partial H_1}{\partial z} = 0$$
$$\frac{\partial H_1}{\partial \theta} = e\sin(\theta - \Omega t)$$
$$\frac{\partial H_1}{\partial t} = -\Omega e\sin(\theta - \Omega t)$$

First Order Pressure and Derivatives

$$P_1 = P_{1c}\cos(\theta - \Omega t) + P_{1s}\sin(\theta - \Omega t)$$
$$\frac{\partial P_1}{\partial z} = \frac{dP_{1c}}{dz}\cos(\theta - \Omega t) + \frac{dP_{1s}}{dz}\sin(\theta - \Omega t)$$
$$\frac{\partial P_1}{\partial \theta} = -P_{1c}\sin(\theta - \Omega t) + P_{1s}\cos(\theta - \Omega t)$$
$$\frac{\partial P_1}{\partial t} = \Omega P_{1c}\sin(\theta - \Omega t) - \Omega P_{1s}\cos(\theta - \Omega t)$$

First Order Axial Velocity and Derivatives

$$V_{z1} = V_{z1c}\cos(\theta - \Omega t) + V_{z1s}\sin(\theta - \Omega t)$$
$$\frac{\partial V_{z1}}{\partial z} = \frac{dV_{z1c}}{dz}\cos(\theta - \Omega t) + \frac{dV_{z1s}}{dz}\sin(\theta - \Omega t)$$
$$\frac{\partial V_{z1}}{\partial \theta} = -V_{z1c}\sin(\theta - \Omega t) + V_{z1s}\cos(\theta - \Omega t)$$
$$\frac{\partial V_{z1}}{\partial t} = \Omega V_{z1c}\sin(\theta - \Omega t) - \Omega V_{z1s}\cos(\theta - \Omega t)$$

First Order Circumferential Velocity and Derivatives

$$V_{\theta 1} = V_{\theta 1c}\cos(\theta - \Omega t) + V_{\theta 1s}\sin(\theta - \Omega t)$$
$$\frac{\partial V_{\theta 1}}{\partial z} = \frac{dV_{\theta 1c}}{dz}\cos(\theta - \Omega t) + \frac{dV_{\theta 1s}}{dz}\sin(\theta - \Omega t)$$
$$\frac{\partial V_{\theta 1}}{\partial \theta} = -V_{\theta 1c}\sin(\theta - \Omega t) + V_{\theta 1s}\cos(\theta - \Omega t)$$
$$\frac{\partial V_{\theta 1}}{\partial t} = \Omega V_{\theta 1c}\sin(\theta - \Omega t) - \Omega V_{\theta 1s}\cos(\theta - \Omega t)$$

Appendix D. Expansion of First Order Equations

First Order Continuity Equation

Beginning with the first order continuity equation from Appendix B:

$$\frac{\partial H_1}{\partial t} + \frac{\partial}{\partial z}(V_{z1}H_0 + V_{z0}H_1) + \frac{1}{R}\frac{\partial}{\partial \theta}(V_{\theta 1}H_0 + V_{\theta 0}H_1) = 0$$

The following assumptions are used in the small perturbation analysis:

$$\frac{\partial H_1}{\partial z} = 0 \qquad \frac{\partial H_0}{\partial \theta} = 0 \qquad \frac{\partial V_{z0}}{\partial \theta} = 0$$

Expanding the first order equation with these assumptions we have:

$$\frac{\partial H_1}{\partial t} + V_{z1}\frac{\partial H_0}{\partial z} + H_0\frac{\partial V_{z1}}{\partial z} + H_1\frac{\partial V_{z0}}{\partial z} + \frac{1}{R}\left(H_0\frac{\partial V_{\theta 1}}{\partial \theta} + V_{\theta 0}\frac{\partial H_1}{\partial \theta}\right) = 0$$

Now substitute the perturbation variables from Appendix C:

$$-\Omega e \sin\phi + (V_{z1c}\cos\phi + V_{z1s}\sin\phi)\frac{dH_0}{dz} + H_0\left(\frac{dV_{z1c}}{dz}\cos\phi + \frac{dV_{z1s}}{dz}\sin\phi\right)$$

$$-e\cos\phi\frac{dV_{z0}}{dz} + \frac{H_0}{R}(-V_{\theta 1c}\sin\phi + V_{\theta 1s}\cos\phi) + \frac{V_{\theta 0}}{R}e\sin\phi = 0$$

To satisfy this equation, the coefficients multiplying both the sine and cosine terms must be equal. This gives us two equations. Equating the cosine coefficients we have:

$$\frac{dH_0}{dz}V_{z1c} + H_0\frac{dV_{z1c}}{dz} - e\frac{dV_{z0}}{dz} + \frac{H_0}{R}V_{\theta 1s} = 0$$

Equating the sine coefficients we have:

$$-\Omega e + \frac{dH_0}{dz}V_{z1s} + H_0\frac{dV_{z1s}}{dz} - \frac{H_0}{R}V_{\theta 1c} + \frac{V_{\theta 0}}{R}e = 0$$

Rearranging the cosine terms:

$$H_0\frac{dV_{z1c}}{dz} + \frac{dH_0}{dz}V_{z1c} + \frac{H_0}{R}V_{\theta 1s} = e\frac{dV_{z0}}{dz} \qquad (D.1)$$

Rearranging the sine terms:

$$H_0\frac{dV_{z1s}}{dz} + \frac{dH_0}{dz}V_{z1s} - \frac{H_0}{R}V_{\theta 1c} = e\left(\Omega - \frac{V_{\theta 0}}{R}\right) \qquad (D.2)$$

These are the two equations used in the continuity portion of the first order solution.

First Order Axial Momentum Equation

Beginning with the first order axial momentum equation from Appendix B:

$$H_0\left(\frac{\partial V_{z1}}{\partial t}+\frac{V_{\theta 0}}{R}\frac{\partial V_{z1}}{\partial \theta}+V_{z0}\frac{\partial V_{z1}}{\partial z}+V_{z1}\frac{\partial V_{z0}}{\partial z}\right)+H_1V_{z0}\frac{\partial V_{z0}}{\partial z}=\frac{-1}{\rho}\left(H_0\frac{\partial P_1}{\partial z}+H_1\frac{\partial P_0}{\partial z}+\tau_{sz1}+\tau_{rz1}\right)$$

The first order shear stress is found by a Taylor Series expansion in the perturbation variables:

$$\tau_{sz}=\tau_{sz0}+\frac{\partial \tau_{sz}}{\partial V_z}V_{z1}+\frac{\partial \tau_{sz}}{\partial V_\theta}V_{\theta 1}+\frac{\partial \tau_{sz}}{\partial H}H_1+\cdots$$

$$\tau_{sz}=\tau_{sz0}+\tau_{sz1}$$

Considering only first order terms we have:

$$\tau_{sz1}=\frac{\partial \tau_{sz}}{\partial V_z}V_{z1}+\frac{\partial \tau_{sz}}{\partial V_\theta}V_{\theta 1}+\frac{\partial \tau_{sz}}{\partial H}H_1$$

And similarly for the rotor shear stress:

$$\tau_{rz1}=\frac{\partial \tau_{rz}}{\partial V_z}V_{z1}+\frac{\partial \tau_{rz}}{\partial V_\theta}V_{\theta 1}+\frac{\partial \tau_{rz}}{\partial H}H_1$$

The derivatives are evaluated from the zeroth order solution. Substituting these expressions along with the pertubation variables from Appendix C we have:

$$H_0(\Omega V_{z1c}\sin\phi - \Omega V_{z1s}\cos\phi) + H_0\frac{V_{\theta 0}}{R}(-V_{z1c}\sin\phi + V_{z1s}\cos\phi)$$
$$+ H_0 V_{z0}\left(\frac{dV_{z1c}}{dz}\cos\phi + \frac{dV_{z1s}}{dz}\sin\phi\right) + H_0(V_{z1c}\cos\phi + V_{z1s}\sin\phi)\frac{dV_{z0}}{dz}$$
$$-(e\cos\phi)\left(V_{z0}\frac{dV_{z0}}{dz}\right) = -\frac{H_0}{\rho}\left(\frac{dP_{1c}}{dz}\cos\phi + \frac{dP_{1s}}{dz}\sin\phi\right)$$
$$-\frac{1}{\rho}(-e\cos\phi)\frac{dP_0}{dz} - \frac{1}{\rho}\left(\frac{\partial\tau_{sz}}{\partial V_z} + \frac{\partial\tau_{rz}}{\partial V_z}\right)(V_{z1c}\cos\phi + V_{z1s}\sin\phi)$$
$$-\frac{1}{\rho}\left(\frac{\partial\tau_{sz}}{\partial V_\theta} + \frac{\partial\tau_{rz}}{\partial V_\theta}\right)(V_{\theta 1c}\cos\phi + V_{\theta 1s}\sin\phi) - \frac{1}{\rho}\left(\frac{\partial\tau_{sz}}{\partial H} + \frac{\partial\tau_{rz}}{\partial H}\right)(-e\cos\phi)$$

Equating all the cosine coefficients we have:

$$-H_0\Omega V_{z1s} + H_0\frac{V_{\theta 0}}{R}V_{z1s} + H_0 V_{z0}\frac{dV_{z1c}}{dz} + H_0\frac{dV_{z0}}{dz}V_{z1c} - eV_{z0}\frac{dV_{z0}}{dz}$$
$$= -\frac{H_0}{\rho}\frac{dP_{1c}}{dz} + \frac{1}{\rho}e\frac{dP_0}{dz} - \frac{1}{\rho}\left(\frac{\partial\tau_{sz}}{\partial V_z} + \frac{\partial\tau_{rz}}{\partial V_z}\right)V_{z1c} - \frac{1}{\rho}\left(\frac{\partial\tau_{sz}}{\partial V_\theta} + \frac{\partial\tau_{rz}}{\partial V_\theta}\right)V_{\theta 1c} + \frac{1}{\rho}e\left(\frac{\partial\tau_{sz}}{\partial H} + \frac{\partial\tau_{rz}}{\partial H}\right)$$

Equating all the sine coefficients we have:

$$H_0\Omega V_{z1c} - H_0\frac{V_{\theta 0}}{R}V_{z1c} + H_0 V_{z0}\frac{dV_{z1s}}{dz} + H_0\frac{dV_{z0}}{dz}V_{z1s}$$
$$= -\frac{H_0}{\rho}\frac{dP_{1s}}{dz} - \frac{1}{\rho}\left(\frac{\partial\tau_{sz}}{\partial V_z} + \frac{\partial\tau_{rz}}{\partial V_z}\right)V_{z1s} - \frac{1}{\rho}\left(\frac{\partial\tau_{sz}}{\partial V_\theta} + \frac{\partial\tau_{rz}}{\partial V_\theta}\right)V_{\theta 1s}$$

Rearranging the cosine terms:

$$\frac{H_0}{\rho}\frac{dP_{1c}}{dz} + H_0 V_{z0}\frac{dV_{z1c}}{dz} + \left[H_0\frac{dV_{z0}}{dz} + \frac{1}{\rho}\left(\frac{\partial\tau_{sz}}{\partial V_z} + \frac{\partial\tau_{rz}}{\partial V_z}\right)\right]V_{z1c} + H_0\left(\frac{V_{\theta 0}}{R} - \Omega\right)V_{z1s}$$

$$+\frac{1}{\rho}\left(\frac{\partial\tau_{sz}}{\partial V_\theta} + \frac{\partial\tau_{rz}}{\partial V_\theta}\right)V_{\theta 1c} = e\left[V_{z0}\frac{dV_{z0}}{dz} + \frac{1}{\rho}\left(\frac{dP_0}{dz} + \frac{\partial\tau_{sz}}{\partial H} + \frac{\partial\tau_{rz}}{\partial H}\right)\right]$$

Rearranging the sine terms:

$$\frac{H_0}{\rho}\frac{dP_{1s}}{dz} + H_0 V_{z0}\frac{dV_{z1s}}{dz} + H_0\left(\Omega - \frac{V_{\theta 0}}{R}\right)V_{z1c} + \left[H_0\frac{dV_{z0}}{dz} + \frac{1}{\rho}\left(\frac{\partial\tau_{sz}}{\partial V_z} + \frac{\partial\tau_{rz}}{\partial V_z}\right)\right]V_{z1s}$$

$$+\frac{1}{\rho}\left(\frac{\partial\tau_{sz}}{\partial V_\theta} + \frac{\partial\tau_{rz}}{\partial V_\theta}\right)V_{\theta 1s} = 0$$

These are the first order axial momentum equations used in the first order solution.

The shear stress terms present the greatest challenge in this analysis. These are modelled as follows. Starting with the shear stress on the stator, we use the Blasius shear stress model where

$$\tau_s = \frac{1}{2}\rho(V_\theta^2 + V_z^2)\, f_s$$

where the friction factor comes from Hir's turbulent bulk-flow theory:

$$f_s = ns(Re)^{ms}$$

the Reynolds number based on the radial clearance of the seal is:

$$Re = \frac{H\sqrt{V_\theta^2 + V_z^2}}{\nu}$$

For fully developed turbulent flow the friction factor is:

$$f_s = ns\left(\frac{H\sqrt{V_\theta^2 + V_z^2}}{\nu}\right)^{ms}$$

The axial component of the shear stress is determined from the velocity triangle:

$$\tau_{sz} = \tau_s\left(\frac{V_z}{\sqrt{V_\theta^2 + V_z^2}}\right)$$

The expanded form of the axial shear stress in primitive variables is then:

$$\tau_{sz} = \frac{1}{2}\rho(V_\theta^2 + V_z^2)ns\left(\frac{H\sqrt{V_\theta^2 + V_z^2}}{\nu}\right)^{ms}\left(\frac{V_z}{\sqrt{V_\theta^2 + V_z^2}}\right)$$

Simplifying this expression somewhat we have:

$$\tau_{sz} = \frac{1}{2}\rho V_z[V_\theta^2 + V_z^2]^{\left(\frac{ms+1}{2}\right)} ns\left(\frac{H}{\nu}\right)^{ms}$$

The axial shear stress on the rotor follows a similar derivation:

$$\tau_{rz} = \frac{1}{2}\rho V_z[(V_\theta - R\omega)^2 + V_z^2]^{\left(\frac{mr+1}{2}\right)} nr\left(\frac{H}{\nu}\right)^{mr}$$

The partial derivatives are evaluated as follows:

$$\frac{\partial \tau_{sz}}{\partial V_z} = \frac{\rho}{2}\left\{[V_\theta^2 + V_z^2]^{\left(\frac{ms+1}{2}\right)} ns\left(\frac{H}{\nu}\right)^{ms}\right\}\frac{dV_z}{dV_z} + \frac{\rho}{2}\left\{V_z ns\left(\frac{H}{\nu}\right)^{ms}\right\}\frac{d}{dV_z}[V_\theta^2 + V_z^2]^{\left(\frac{ms+1}{2}\right)}$$

$$\frac{\partial \tau_{sz}}{\partial V_\theta} = \frac{\rho}{2}\left\{V_z ns\left(\frac{H}{\nu}\right)^{ms}\right\}\frac{d}{dV_\theta}[V_\theta^2 + V_z^2]^{\left(\frac{ms+1}{2}\right)}$$

$$\frac{\partial \tau_{sz}}{\partial H} = \frac{\rho}{2}\left\{V_z[V_\theta^2 + V_z^2]^{\left(\frac{ms+1}{2}\right)}\right\}\frac{d}{dH}\left[ns\left(\frac{H}{\nu}\right)^{ms}\right]$$

$$\frac{\partial \tau_{rz}}{\partial V_z} = \frac{\rho}{2}\left\{[(V_\theta - R\omega)^2 + V_z^2]^{\left(\frac{mr+1}{2}\right)} nr\left(\frac{H}{\nu}\right)^{mr}\right\}\frac{dV_z}{dV_z} + \frac{\rho}{2}\left\{V_z nr\left(\frac{H}{\nu}\right)^{mr}\right\}\frac{d}{dV_z}[(V_\theta - R\omega)^2 + V_z^2]^{\left(\frac{mr+1}{2}\right)}$$

$$\frac{\partial \tau_{rz}}{\partial V_\theta} = \frac{\rho}{2}\left\{V_z nr\left(\frac{H}{\nu}\right)^{mr}\right\}\frac{d}{dV_\theta}[(V_\theta - R\omega)^2 + V_z^2]^{\left(\frac{mr+1}{2}\right)}$$

$$\frac{\partial \tau_{rz}}{\partial H} = \frac{\rho}{2}\left\{V_z[(V_\theta - R\omega)^2 + V_z^2]^{\left(\frac{mr+1}{2}\right)}\right\}\frac{d}{dH}\left[nr\left(\frac{H}{\nu}\right)^{mr}\right]$$

It is enlightening to write the shear stress in terms of the axial Reynolds number where the contribution of swirling flow can be more readily seen. The following equations show the shear stress and derivatives in this form.

$$\tau_{sz} = \frac{1}{2}\rho V_z^2 ns\left(\frac{V_z H}{\nu}\right)^{ms}\left[1+\frac{V_\theta^2}{V_z^2}\right]^{\left(\frac{ms+1}{2}\right)}$$

$$\tau_{rz} = \frac{1}{2}\rho V_z^2 nr\left(\frac{V_z H}{\nu}\right)^{mr}\left[1+\frac{(V_\theta - R\omega)^2}{V_z^2}\right]^{\left(\frac{mr+1}{2}\right)}$$

$$\frac{\partial \tau_{sz}}{\partial V_z} = \frac{\tau_{sz}}{V_z}\left\{1+(ms+1)\left[1+\frac{V_\theta^2}{V_z^2}\right]^{-1}\right\}$$

$$\frac{\partial \tau_{sz}}{\partial V_\theta} = \frac{\tau_{sz}}{V_\theta}(ms+1)\left[1+\frac{V_z^2}{V_\theta^2}\right]^{-1}$$

$$\frac{\partial \tau_{sz}}{\partial H} = \frac{\tau_{sz}}{H}(ms)$$

$$\frac{\partial \tau_{rz}}{\partial V_z} = \frac{\tau_{rz}}{V_z}\left\{1+(mr+1)\left[1+\frac{(V_\theta - R\omega)^2}{V_z^2}\right]^{-1}\right\}$$

$$\frac{\partial \tau_{rz}}{\partial V_\theta} = \frac{\tau_{rz}}{(V_\theta - R\omega)}(mr+1)\left[1+\frac{V_z^2}{(V_\theta - R\omega)^2}\right]^{-1}$$

$$\frac{\partial \tau_{rz}}{\partial H} = \frac{\tau_{rz}}{H}(mr)$$

First Order Circumferential Momentum Equation

Beginning with the first order equation from Appendix B:

$$H_0\left(\frac{\partial V_{\theta 1}}{\partial t}+\frac{V_{\theta 0}}{R}\frac{\partial V_{\theta 1}}{\partial \theta}+V_{z0}\frac{\partial V_{\theta 1}}{\partial z}+V_{z1}\frac{\partial V_{\theta 0}}{\partial z}\right)+H_1 V_{z0}\frac{\partial V_{\theta 0}}{\partial z}=-\frac{1}{\rho}\left(\frac{H_0}{R}\frac{\partial P_1}{\partial \theta}+\tau_{s\theta 1}+\tau_{r\theta 1}\right)$$

Following the same procedure as with the axial momentum equation, the first order shear stress terms are given by:

$$\tau_{s\theta 1}=\frac{\partial \tau_{s\theta}}{\partial V_z}V_{z1}+\frac{\partial \tau_{s\theta}}{\partial V_\theta}V_{\theta 1}+\frac{\partial \tau_{s\theta}}{\partial H}H_1$$

$$\tau_{r\theta 1}=\frac{\partial \tau_{r\theta}}{\partial V_z}V_{z1}+\frac{\partial \tau_{r\theta}}{\partial V_\theta}V_{\theta 1}+\frac{\partial \tau_{r\theta}}{\partial H}H_1$$

Substituting the perturbation variables from Appendix C:

$$H_0(\Omega V_{\theta 1c}\sin\phi-\Omega V_{\theta 1s}\cos\phi)+H_0\frac{V_{\theta 0}}{R}(-V_{\theta 1c}\sin\phi+V_{\theta 1s}\cos\phi)$$
$$+H_0V_{z0}\left(\frac{dV_{\theta 1c}}{dz}\cos\phi+\frac{dV_{\theta 1s}}{dz}\sin\phi\right)+H_0(V_{z1c}\cos\phi+V_{z1s}\sin\phi)\frac{dV_{\theta 0}}{dz}$$
$$-(e\cos\phi)\left(V_{z0}\frac{dV_{\theta 0}}{dz}\right)=-\frac{H_0}{R\rho}(-P_{1c}\sin\phi+P_{1s}\cos\phi)$$
$$-\frac{1}{\rho}\left(\frac{\partial \tau_{s\theta}}{\partial V_z}+\frac{\partial \tau_{r\theta}}{\partial V_z}\right)(V_{z1c}\cos\phi+V_{z1s}\sin\phi)-\frac{1}{\rho}\left(\frac{\partial \tau_{s\theta}}{\partial V_\theta}+\frac{\partial \tau_{r\theta}}{\partial V_\theta}\right)(V_{\theta 1c}\cos\phi+V_{\theta 1s}\sin\phi)$$
$$-\frac{1}{\rho}\left(\frac{\partial \tau_{s\theta}}{\partial H}+\frac{\partial \tau_{r\theta}}{\partial H}\right)(-e\cos\phi)$$

Equating all the cosine coefficients we have:

$$-H_0\Omega V_{\theta 1s} + H_0 \frac{V_{\theta 0}}{R} V_{\theta 1s} + H_0 V_{z0} \frac{dV_{\theta 1c}}{dz} + H_0 \frac{dV_{\theta 0}}{dz} V_{z1c} - eV_{z0} \frac{dV_{\theta 0}}{dz}$$
$$= -\frac{H_0}{R\rho} P_{1s} - \frac{1}{\rho}\left(\frac{\partial \tau_{s\theta}}{\partial V_z} + \frac{\partial \tau_{r\theta}}{\partial V_z}\right) V_{z1c} - \frac{1}{\rho}\left(\frac{\partial \tau_{s\theta}}{\partial V_\theta} + \frac{\partial \tau_{r\theta}}{\partial V_\theta}\right) V_{\theta 1c} + \frac{1}{\rho} e\left(\frac{\partial \tau_{s\theta}}{\partial H} + \frac{\partial \tau_{r\theta}}{\partial H}\right)$$

Equating all the sine coefficients we have:

$$H_0\Omega V_{\theta 1c} - H_0 \frac{V_{\theta 0}}{R} V_{\theta 1c} + H_0 V_{z0} \frac{dV_{\theta 1s}}{dz} + H_0 \frac{dV_{\theta 0}}{dz} V_{z1s}$$
$$= \frac{H_0}{R\rho} P_{1c} - \frac{1}{\rho}\left(\frac{\partial \tau_{s\theta}}{\partial V_z} + \frac{\partial \tau_{r\theta}}{\partial V_z}\right) V_{z1s} - \frac{1}{\rho}\left(\frac{\partial \tau_{s\theta}}{\partial V_\theta} + \frac{\partial \tau_{r\theta}}{\partial V_\theta}\right) V_{\theta 1s}$$

Rearranging the cosine terms:

$$H_0 V_{z0} \frac{dV_{\theta 1c}}{dz} + \frac{H_0}{R\rho} P_{1s} + \left[H_0 \frac{dV_{\theta 0}}{dz} + \frac{1}{\rho}\left(\frac{\partial \tau_{s\theta}}{\partial V_z} + \frac{\partial \tau_{r\theta}}{\partial V_z}\right)\right] V_{z1c}$$
$$+ \frac{1}{\rho}\left(\frac{\partial \tau_{s\theta}}{\partial V_\theta} + \frac{\partial \tau_{r\theta}}{\partial V_\theta}\right) V_{\theta 1c} + H_0\left(\frac{V_{\theta 0}}{R} - \Omega\right) V_{\theta 1s} = e\left[V_{z0} \frac{dV_{\theta 0}}{dz} + \frac{1}{\rho}\left(\frac{\partial \tau_{s\theta}}{\partial H} + \frac{\partial \tau_{r\theta}}{\partial H}\right)\right]$$

Rearranging the sine terms:

$$H_0 V_{z0} \frac{dV_{\theta 1s}}{dz} - \frac{H_0}{R\rho} P_{1c} + \left[H_0 \frac{dV_{\theta 0}}{dz} + \frac{1}{\rho}\left(\frac{\partial \tau_{s\theta}}{\partial V_z} + \frac{\partial \tau_{r\theta}}{\partial V_z}\right)\right] V_{z1s}$$
$$+ H_0\left(\Omega - \frac{V_{\theta 0}}{R}\right) V_{\theta 1c} + \frac{1}{\rho}\left(\frac{\partial \tau_{s\theta}}{\partial V_\theta} + \frac{\partial \tau_{r\theta}}{\partial V_\theta}\right) V_{\theta 1s} = 0$$

These are the circumferential momentum equations used in the first order solution.

The circumferential shear stress on the stator is:

$$\tau_{s\theta} = \frac{1}{2}\rho V_\theta [V_\theta^2 + V_z^2]^{\left(\frac{ms+1}{2}\right)} ns \left(\frac{H}{v}\right)^{ms}$$

The circumferential shear stress on the rotor is:

$$\tau_{r\theta} = \frac{1}{2}\rho (V_\theta - R\omega)[(V_\theta - R\omega)^2 + V_z^2]^{\left(\frac{mr+1}{2}\right)} nr \left(\frac{H}{v}\right)^{mr}$$

The derivatives are evaluated as follows:

$$\frac{\partial \tau_{s\theta}}{\partial V_z} = \frac{\rho}{2}\left\{V_\theta ns \left(\frac{H}{v}\right)^{ms}\right\} \frac{d}{dV_z}[V_\theta^2 + V_z^2]^{\left(\frac{ms+1}{2}\right)}$$

$$\frac{\partial \tau_{s\theta}}{\partial V_\theta} = \frac{\rho}{2}\left\{[V_\theta^2 + V_z^2]^{\left(\frac{ms+1}{2}\right)} ns \left(\frac{H}{v}\right)^{ms}\right\} \frac{dV_\theta}{dV_\theta}$$
$$+ \frac{\rho}{2}\left\{V_\theta\, ns \left(\frac{H}{v}\right)^{ms}\right\} \frac{d}{dV_\theta}[V_\theta^2 + V_z^2]^{\left(\frac{ms+1}{2}\right)}$$

$$\frac{\partial \tau_{s\theta}}{\partial H} = \frac{\rho}{2}\left\{V_\theta [V_\theta^2 + V_z^2]^{\left(\frac{ms+1}{2}\right)}\right] \frac{d}{dH}\left[ns \left(\frac{H}{v}\right)^{ms}\right]$$

$$\frac{\partial \tau_{r\theta}}{\partial V_z} = \frac{\rho}{2}\left\{(V_\theta - R\omega) nr \left(\frac{H}{v}\right)^{mr}\right\} \frac{d}{dV_z}[(V_\theta - R\omega)^2 + V_z^2]^{\left(\frac{mr+1}{2}\right)}$$

$$\frac{\partial \tau_{r\theta}}{\partial V_\theta} = \frac{\rho}{2}\left\{[(V_\theta - R\omega)^2 + V_z^2]^{\left(\frac{mr+1}{2}\right)} nr \left(\frac{H}{v}\right)^{mr}\right\} \frac{d}{dV_\theta}(V_\theta - R\omega)$$
$$+ \frac{\rho}{2}\left\{(V_\theta - R\omega)\, nr \left(\frac{H}{v}\right)^{mr}\right\} \frac{d}{dV_\theta}[(V_\theta - R\omega)^2 + V_z^2]^{\left(\frac{mr+1}{2}\right)}$$

$$\frac{\partial \tau_{r\theta}}{\partial H} = \frac{\rho}{2}\left\{(V_\theta - R\omega)[(V_\theta - R\omega)^2 + V_z^2]^{\left(\frac{mr+1}{2}\right)}\right] \frac{d}{dH}\left[nr \left(\frac{H}{v}\right)^{mr}\right]$$

Again these expressions may be simplified when expressed in terms of the axial Reynolds number as follows:

$$\tau_{s\theta} = \frac{1}{2}\rho V_z V_\theta ns\left(\frac{V_z H}{\nu}\right)^{ms}\left[1+\frac{V_\theta^2}{V_z^2}\right]^{\left(\frac{ms+1}{2}\right)}$$

$$\tau_{r\theta} = \frac{1}{2}\rho V_z (V_\theta - R\omega) nr\left(\frac{V_z H}{\nu}\right)^{mr}\left[1+\frac{(V_\theta - R\omega)^2}{V_z^2}\right]^{\left(\frac{mr+1}{2}\right)}$$

$$\frac{\partial \tau_{s\theta}}{\partial V_z} = \frac{\tau_{s\theta}}{V_z}(ms+1)\left[1+\frac{V_\theta^2}{V_z^2}\right]^{-1}$$

$$\frac{\partial \tau_{s\theta}}{\partial V_\theta} = \frac{\tau_{s\theta}}{V_\theta}\left\{1+(ms+1)\left[1+\frac{V_z^2}{V_\theta^2}\right]^{-1}\right\}$$

$$\frac{\partial \tau_{s\theta}}{\partial H} = \frac{\tau_{s\theta}}{H}(ms)$$

$$\frac{\partial \tau_{r\theta}}{\partial V_z} = \frac{\tau_{r\theta}}{V_z}(mr+1)\left[1+\frac{(V_\theta - R\omega)^2}{V_z^2}\right]^{-1}$$

$$\frac{\partial \tau_{r\theta}}{\partial V_\theta} = \frac{\tau_{r\theta}}{(V_\theta - R\omega)}\left\{1+(mr+1)\left[1+\frac{V_z^2}{(V_\theta - R\omega)^2}\right]^{-1}\right\}$$

$$\frac{\partial \tau_{r\theta}}{\partial H} = \frac{\tau_{r\theta}}{H}(mr)$$

Appendix E. Matrices for First Order Solution

The first order equations can be summarized by the following matrix equation:

$$[A]\frac{d[X]}{dz} + [B][X] = [C]\ e$$

where the matrices are defined as follows:

$$[A] = \begin{bmatrix} A_{11} & A_{12} & A_{13} & A_{14} & A_{15} & A_{16} \\ A_{21} & A_{22} & A_{23} & A_{24} & A_{25} & A_{26} \\ A_{31} & A_{32} & A_{33} & A_{34} & A_{35} & A_{36} \\ A_{41} & A_{42} & A_{43} & A_{44} & A_{45} & A_{46} \\ A_{51} & A_{52} & A_{53} & A_{54} & A_{55} & A_{56} \\ A_{61} & A_{62} & A_{63} & A_{64} & A_{65} & A_{66} \end{bmatrix} \begin{matrix} \text{cosine terms} \\ \text{sine terms} \\ \text{cosine terms} \\ \text{sine terms} \\ \text{cosine terms} \\ \text{sine terms} \end{matrix} \begin{matrix} \} \text{Continuity} \\ \\ \} z\text{ - Momentum} \\ \\ \} \theta\text{ - Momentum} \\ \end{matrix}$$

$$[B] = \begin{bmatrix} B_{11} & B_{12} & B_{13} & B_{14} & B_{15} & B_{16} \\ B_{21} & B_{22} & B_{23} & B_{24} & B_{25} & B_{26} \\ B_{31} & B_{32} & B_{33} & B_{34} & B_{35} & B_{36} \\ B_{41} & B_{42} & B_{43} & B_{44} & B_{45} & B_{46} \\ B_{51} & B_{52} & B_{53} & B_{54} & B_{55} & B_{56} \\ B_{61} & B_{62} & B_{63} & B_{64} & B_{65} & B_{66} \end{bmatrix} \begin{matrix} \text{cosine terms} \\ \text{sine terms} \end{matrix} \} \text{Continuity}$$

$$\begin{matrix} \text{cosine terms} \\ \text{sine terms} \end{matrix} \} z \text{ - Momentum}$$

$$\begin{matrix} \text{cosine terms} \\ \text{sine terms} \end{matrix} \} \theta \text{ - Momentum}$$

$$[C] = \begin{bmatrix} C_1 \\ C_2 \\ C_3 \\ C_4 \\ C_5 \\ C_6 \end{bmatrix} \begin{matrix} \text{cosine terms} \\ \text{sine terms} \end{matrix} \} \text{Continuity}$$

$$\begin{matrix} \text{cosine terms} \\ \text{sine terms} \end{matrix} \} z \text{ - Momentum}$$

$$\begin{matrix} \text{cosine terms} \\ \text{sine terms} \end{matrix} \} \theta \text{ - Momentum}$$

$$[X] = \begin{bmatrix} X_1 \\ X_2 \\ X_3 \\ X_4 \\ X_5 \\ X_6 \end{bmatrix} = \begin{bmatrix} P_{1c} \\ P_{1s} \\ V_{z1c} \\ V_{z1s} \\ V_{\theta 1c} \\ V_{\theta 1s} \end{bmatrix} = f(z)$$

The coefficient matrices are filled according to the first order equations in Appendix D. For example, the coefficient multiplying $V_{\theta 1s}$ in the cosine equation for first order continuity (equation D.1) is $\frac{H_0}{R}$. $V_{\theta 1s} = X_6$, hence $B_{16} = \frac{H_0}{R}$. Following this procedure, all of the non-zero coefficients are defined as follows:

$$A_{13} = H_0$$

$$A_{24} = H_0$$

$$A_{31} = \frac{H_0}{\rho}$$

$$A_{33} = H_0 V_{z0}$$

$$A_{42} = \frac{H_0}{\rho}$$

$$A_{44} = H_0 V_{z0}$$

$$A_{55} = H_0 V_{z0}$$

$$A_{66} = H_0 V_{z0}$$

$$C_1 = \frac{dV_{z0}}{dz}$$

$$C_2 = \left(\Omega - \frac{V_{\theta 0}}{R} \right)$$

$$C_3 = V_{z0} \frac{dV_{z0}}{dz} + \frac{1}{\rho} \left(\frac{dP_0}{dz} + \frac{\partial \tau_{sz}}{\partial H} + \frac{\partial \tau_{rz}}{\partial H} \right)$$

$$C_4 = 0$$

$$C_5 = V_{z0} \frac{dV_{\theta 0}}{dz} + \frac{1}{\rho} \left(\frac{\partial \tau_{s\theta}}{\partial H} + \frac{\partial \tau_{r\theta}}{\partial H} \right)$$

$$C_6 = 0$$

$$B_{13} = \frac{dH_0}{dz}$$

$$B_{16} = \frac{H_0}{R}$$

$$B_{24} = \frac{dH_0}{dz}$$

$$B_{25} = -\frac{H_0}{R}$$

$$B_{33} = H_0 \frac{dV_{z0}}{dz} + \frac{1}{\rho}\left(\frac{\partial \tau_{sz}}{\partial V_z} + \frac{\partial \tau_{rz}}{\partial V_z}\right)$$

$$B_{34} = H_0\left(\frac{V_{\theta 0}}{R} - \Omega\right)$$

$$B_{35} = \frac{1}{\rho}\left(\frac{\partial \tau_{sz}}{\partial V_\theta} + \frac{\partial \tau_{rz}}{\partial V_\theta}\right)$$

$$B_{43} = H_0\left(\Omega - \frac{V_{\theta 0}}{R}\right)$$

$$B_{44} = H_0 \frac{dV_{z0}}{dz} + \frac{1}{\rho}\left(\frac{\partial \tau_{sz}}{\partial V_z} + \frac{\partial \tau_{rz}}{\partial V_z}\right)$$

$$B_{46} = \frac{1}{\rho}\left(\frac{\partial \tau_{sz}}{\partial V_\theta} + \frac{\partial \tau_{rz}}{\partial V_\theta}\right)$$

$$B_{52} = \frac{H_0}{R\rho}$$

$$B_{53} = H_0 \frac{dV_{\theta 0}}{dz} + \frac{1}{\rho}\left(\frac{\partial \tau_{s\theta}}{\partial V_z} + \frac{\partial \tau_{r\theta}}{\partial V_z}\right)$$

$$B_{55} = \frac{1}{\rho}\left(\frac{\partial \tau_{s\theta}}{\partial V_\theta} + \frac{\partial \tau_{r\theta}}{\partial V_\theta}\right)$$

$$B_{56} = H_0\left(\frac{V_{\theta 0}}{R} - \Omega\right)$$

$$B_{61} = -\frac{H_0}{R\rho}$$

$$B_{64} = H_0 \frac{dV_{\theta 0}}{dz} + \frac{1}{\rho}\left(\frac{\partial \tau_{s\theta}}{\partial V_z} + \frac{\partial \tau_{r\theta}}{\partial V_z}\right)$$

$$B_{65} = H_0\left(\Omega - \frac{V_{\theta 0}}{R}\right)$$

$$B_{66} = \frac{1}{\rho}\left(\frac{\partial \tau_{s\theta}}{\partial V_\theta} + \frac{\partial \tau_{r\theta}}{\partial V_\theta}\right)$$

Vita

Kevin Wilkes received his Bachelor's Degree with Honors in Mechanical Engineering from the University of Florida in 1986. He began his career as an analytical engineer in the compressor design group at Pratt & Whitney's Government Engine Business in West Palm Beach. Kevin worked extensively on the F100-PW-229 developmental engine from the first full scale engine test in December 1986 through the first production engine buy. In 1989 he was granted a two year academic leave of absence to pursue a Master's degree at Virginia Polytechnic Institute & State University. Kevin has since been awarded the Charles E. Minor Fellowship and has elected to remain at Virginia Tech for his Ph.D.

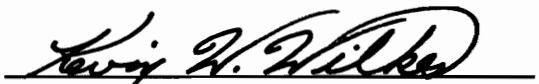

Kevin W. Wilkes